Marco Antonio Gómez-Guzmán

Global dynamics evaluation in brain cancer model using deep learning techniques and iterative locali

Universidad Autónoma del Estado de Baja California

Detalles del documento

Identificador de la entrega
trn:oid:::3117:474051380

Fecha de entrega
15 jul 2025, 1:34 p.m. GMT-7

Fecha de descarga
15 jul 2025, 1:44 p.m. GMT-7

Nombre de archivo
Tesis_R2_FINAL-15julio2025.pdf

Tamaño de archivo
10.0 MB

84 Páginas

26.923 Palabras

150.777 Caracteres

Visto Bueno Director de tesis y Co-directora de tesis

Dr. Everardo Inzunza Gonzalez
Director de tesis

Dra. Laura Jiménez Beristain
Co-directora de tesis

31% Similitud general

El total combinado de todas las coincidencias, incluidas las fuentes superpuestas, para ca...

Grupos de coincidencias

- **500** Sin cita o referencia 26%
  Coincidencias sin una citación ni comillas en el texto
- **62** Faltan citas 2%
  Coincidencias que siguen siendo muy similar al material fuente
- **13** Falta referencia 2%
  Las coincidencias tienen comillas, pero no una citación correcta en el texto
- **0** Con comillas y referencia 0%
  Coincidencias de citación en el texto, pero sin comillas

Fuentes principales

- 23% Fuentes de Internet
- 28% Publicaciones
- 0% Trabajos entregados (trabajos del estudiante)

Marcas de integridad

N.º de alerta de integridad para revisión

- **Caracteres reemplazados**
  149 caracteres sospechosos en N.º de páginas
  Las letras son intercambiadas por caracteres similares de otro alfabeto.

Los algoritmos de nuestro sistema analizan un documento en profundidad para buscar inconsistencias que permitirían distinguirlo de una entrega normal. Si advertimos algo extraño, lo marcamos como una alerta para que pueda revisarlo.

Una marca de alerta no es necesariamente un indicador de problemas. Sin embargo, recomendamos que preste atención y la revise.

Visto Bueno Director de tesis y Co-directora de tesis

Dr. Everardo Inzunza Gonzalez
Director de tesis

Dra. Laura Jiménez Beristain
Co-directora de tesis

Universidad Autónoma de Baja California
Facultad de Ingeniería, Arquitectura y Diseño
Programa de Maestría y Doctorado en Ciencias e Ingeniería

Global dynamics evaluation in brain cancer model using deep learning techniques and iterative localization method

THESIS

that to partially meet the requirements to obtain the degree of
Doctor of Science

Presents:
Marco Antonio Gómez Guzmán
Thesis Advisor:
Dr. Everardo Inzunza González
Thesis Co-advisor:
Dra. Laura Jiménez Beristáin

Ensenada, Baja California, México, August 2025.

UNIVERSIDAD AUTÓNOMA DE BAJA CALIFORNIA

FACULTAD DE INGENIERÍA, ARQUITECTURA Y DISEÑO

MAESTRÍA Y DOCTORADO EN CIENCIAS E INGENIERÍA

Global dynamics evaluation in brain cancer model using deep learning techniques and iterative localization method

TESIS

Que para obtener el grado de Doctorado en Ciencias presenta:

Marco Antonio Gómez Guzmán

Aprobada por:

Dr. Everardo Inzunza-Gonzalez
Director de tesis

Dra. Laura Jiménez Beristáin
Co-directora de tesis

Dr. José Jaime Esqueda Elizondo
Miembro del comité

Dr. Enrique Efrén García Guerrero
Miembro del comité

Dr. Oscar Roberto Lopez Bonilla
Miembro del comité

Ensenada Baja California, 7 de Agosto de 2025.

Universidad Autónoma de Baja California
Facultad de Ingeniería, Arquitectura y Diseño
Maestría y Doctorado en Ciencias e Ingeniería

Global dynamics evaluation in brain cancer model using deep learning techniques and iterative localization method

TESIS

Que como parte de los requisitos para obtener el grado de
Doctor en Ciencias

Presenta:

Marco Antonio Gómez Guzmán

Dirigido por:

Dr. Everardo Inzunza González

Co-dirigido por:

Dra. Laura Jiménez Beristáin

Aprobada por:

Dr. Everardo Inzunza González
Director de tesis

Dra. Laura Jiménez Beristáin
Co-directora de tesis

Dr. José Jaime Esqueda Elizondo
Miembro del comité

Dr. Enrique Efren García Guerrero
Miembro del comité

Dr. Oscar Roberto Lopez Bonilla
Miembro del comité

Ensenada, Baja California, México
Fecha de aprobación de la Tesis
Agosto 2025

This thesis is dedicated to my parents, Mrs. Rosa Elia Guzmán and Mr. Antonio Gómez Pérez, who have given me their support throughout my academic route, which has now reached its culmination, and who, with all their effort, dedication and love, knew how to educate me when I was a child. I love them very much.

Esta tesis está dedicada a mis padres, la Sra. Rosa Elia Guzmán y el Sr. Antonio Gómez Pérez, quienes me han brindado su apoyo a lo largo de mi camino académico que hoy ha llegado a su fin, y quienes, con todo su esfuerzo, dedicación y amor, supieron educarme desde que era niño. Los quiero mucho.

Acknowledgments

- First, I want to thank God for placing me here. Many thanks to my parents for their unwavering support while I followed my goals. For inspiring my brother Angel to follow my career. My son Jesus Benito inspires me to be a better professional and person. All my family members who have supported me remotely deserve my sincerest gratitude.

- To the Consejo Nacional de Humanidades, Ciencias y Tecnologías (CONAHCYT) for having granted me a scholarship during my doctoral studies. In the same way Universidad Autónoma de Baja California (UABC) for all the support provided to carry out this research.

- Thank you, Dr. Everardo Inzunza González, the advisor of my thesis, for your hospitality, advice, and constant support throughout my stay in Ensenada, Baja California. Additionally, I appreciate your friendship and all the teachings you have shared with me. Thank you for your patience in sharing your knowledge and for always encouraging me to complete my doctoral studies.

- Dra. Laura Jiménez Beristáin, my thesis co-advisor, thank you so much for all of her instruction, her consistent patience throughout the classes, and her dedication to impart her expertise. For always welcoming me into your home when I needed it, I appreciate your friendship. I greatly appreciated your insightful feedback and corrections, which significantly contributed to my improvement.

- Thank you to Dr. Oscar Roberto López Bonilla, Dr. Ulises Jesús Tamayo Pérez, and Dr. Enrique Efrén García Guerrero for their invaluable assistance with academic inquiries, including subject-specific concerns, thesis inquiries, article observations, and lecture sharing. Dr. José Jaime Esqueda Elizondo deserves a special mention for his instruction and enthusiastic answers to my queries. Thank you for helping me choose UABC for my doctoral studies.

- I would like to dedicate a special mention to the first person who encouraged me to study for a postgraduate degree and for whom I decided to follow the path of research. Without his motivation and drive, I would not be where I am right now. M.E. Juan Carlos Ramírez Vazquez, research professor at the TECNM campus Pánuco, thank you very much.

- I wish to extend sincere gratitude to Alejandro Duran, Fernando Ayala, David Arroyos, Ilse Ortega, Edgar Ramos, Nestor Mendoza, and Carolina Medina, who are all master's and doctoral students with whom I have had the privilege of working. For their friendship, unwavering support, and for contributing to the overall comfort of this study stay.

Resumen

RESUMEN de la tesis de Marco Antonio Gómez Guzmán, presentada como requisito para obtener el grado de DOCTOR en CIENCIAS, del programa de Maestría y Doctorado en Ciencias e ingeniería de la Universidad Autónoma de Baja California, Ensenada, Baja California México, Agosto 2025.

Global dynamics evaluation in brain cancer model using deep learning techniques and iterative localization method

Resumen aprobado por:

Dr. Everardo Inzunza González
Director de tesis

Dra. Laura Jiménez Beristáin
Co-directora de tesis

Las imágenes por resonancia magnética (IRM) desempeñan un papel fundamental en el diagnóstico de cánceres del sistema nervioso central. En este trabajo de tesis doctoral se integran técnicas de aprendizaje profundo y modelado matemático con el propósito de analizar tumores cerebrales, diferenciar entre gliomas de alto grado (HGG) y bajo grado (LGG), y simular el tratamiento de HGG mediante células T citotóxicas. Se entrenaron, evaluaron y validaron seis modelos de redes neuronales convolucionales (CNN, por sus siglas en inglés) utilizando un total de 7,023 imágenes del conjunto de datos Msoud, el cual incluye imágenes de tumores de tipo glioma, meningioma, pituitario y cerebro sano. El modelo *InceptionV3* obtuvo el mejor desempeño, alcanzando una exactitud del 97.12%. Asimismo, se exploraron seis arquitecturas de aprendizaje profundo para la clasificación de gliomas empleando el conjunto de datos BRATS 2019: *deiT3_base_patch16_224*, *Inception_v4*, *Xception41*, *swin_tiny_patch4_window7_224*, *convNextV2_tiny* y *EfficientNetB0*. El modelo *deiT3_base_patch16_224* demostró el mejor rendimiento utilizando solo el 50% de los datos de entrenamiento, alcanzando una exactitud del 99.08%, una precisión del 99.37%, una recuperación del 98.72% y una puntuación F1 del 99.04%.

Finalmente, se desarrolló y simuló un modelo matemático compuesto por seis ecuaciones diferenciales ordinarias que describen la dinámica del glioma durante la inmunoterapia con células T citotóxicas (CTL), considerando la interacción entre células T, CTL y receptores inmunomediados. Las simulaciones permitieron validar el modelo, establecer hipótesis terapéuticas y evaluar distintos esquemas de tratamiento. Los resultados sugieren que nuevas terapias con dosis intensivas podrían ser efectivas para erradicar los HGG. Este estudio exhaustivo contribuye a la medicina de precisión en el ámbito de la neurooncología al caracterizar tumores cerebrales, clasificar gliomas con alta precisión y modelar el comportamiento terapéutico ante inmunoterapias específicas.

Palabras claves: Tumores cerebrales, Glioma de alto grado, Resonancia magnética, Aprendizaje profundo, Clasificación automática, Redes neuronales convolucionales, Inmunoterapia con células T, Modelado matemático.

Abstract

ABSTRACT of the thesis of Marco Antonio Gómez Guzmán, presented as a requirement to obtain the degree of DOCTOR in SCIENCE, from the Master's and Doctorate program in Science and Engineering of the Universidad Autónoma de Baja California, Ensenada, Baja California Mexico, August 2025.

Global dynamics evaluation in brain cancer model using deep learning techniques and iterative localization method

Abstract approved by:

Dr. Everardo Inzunza González
Thesis Advisor

Dra. Laura Jiménez Beristáin
Thesis Co-advisor

Magnetic resonance imaging (MRI) plays a fundamental role in the diagnosis of cancers of the central nervous system. This doctoral dissertation integrates deep learning (DL) techniques and mathematical modeling to analyze brain tumors, differentiate between high-grade gliomas (HGG) and low-grade gliomas (LGG), and simulate the treatment of HGG using cytotoxic T lymphocytes (CTLs). Six convolutional neural network (CNN) models were trained, evaluated, and tested using a total of 7,023 images from the Msoud dataset, which includes images of glioma, meningioma, pituitary tumors, and healthy brains. The *InceptionV3* model achieved the highest performance, with an accuracy of 97.12%. Additionally, six deep learning architectures were explored for glioma classification using the BRATS 2019 dataset: *deiT3_base_patch16_224*, *Inception_v4*, *Xception41*, *swin_tiny_patch4_window7_224*, *convNextV2_tiny*, and *EfficientNetB0*. The *deiT3_base_patch16_224* model exhibited the best performance using only 50% of the training data, achieving a test accuracy of 99.08%, precision of 99.37%, recall of 98.72%, and an F1-score of 99.04%.

Finally, a mathematical model was developed and simulated to analyze the dynamics of glioma during immunotherapy with CTLs. The model comprises six ordinary differential equations describing T cells, CTLs, and immune-mediated receptors. The simulations validated the model, established treatment hypotheses, and assessed therapeutic strategies. The results suggest that novel high-dose therapy protocols may be effective in eradicating HGG. This comprehensive study contributes to precision neuro-oncology by accurately characterizing brain tumors, classifying gliomas, and modeling therapeutic responses to targeted immunotherapies.

Keywords: Brain tumors, High-grade glioma, Magnetic resonance imaging, Deep learning, Automatic classification, Convolutional neural networks, T-cell immunotherapy, Mathematical modeling.

Contents

List of Figures

List of Tables

CHAPTER 1

Introduction

The brain, a crucial component of the central nervous system, governs all aspects of life via a vast network of neurons. Disease or dysfunction in brain cells may hinder the functioning of any organ related to the brain [1–3].

The World Health Organization (WHO) identifies brain cancer as the most prevalent brain illness [4,5]. Brain tumors, caused by uncontrolled brain cell multiplication, may be fatal [6,7].

A brain tumor's impact on nervous system function relies on its location and growth rate [8]. There are several tumor kinds, including gliomas, meningiomas, and pituitary [9,10]. Additionally, tumors have three main types: 1) Benign; 2) Pre-Malignant; 3) Malignant (only cancer is malignant) [4,11].

The global mortality rate from brain tumors is increasing annually. Brain tumors may affect individuals of all genders, including males, females, and infants [7].

Although new forms of brain cancer have been identified in the last few decades, glioma continues to be the most crucial kind of brain tumor on a worldwide scale due to its severity. It is estimated that around 33% of all brain cancers are gliomas [4]. The WHO-approved grading system categorizes glioma tumor grades. The features of brain tumor cells and the extent of tumor progression establish the classifications of gliomas as Grade I, II, III, or IV. Grade I and Grade II are categorized as Low Grade Gliomas (LGG), whereas Grade III and Grade IV are classed as High Grade Gliomas (HGG). LGG and HGG are alternatively referred to be benign and malignant, respectively [7]. Glioblastoma multiforme, often known as GBM, is a kind of grade IV glioblastoma that is essentially defined by increased heterogeneity, mortality, recurrence, and a lower likelihood of survival [12]. Tumor types are frequently identified by magnetic resonance imaging (MRI), yet MRI interpretation is subjective and data analysis of large volumes can be difficult [10].

Medical imaging encompasses a range of non-invasive techniques that allow for visualizing the inside of the body. Medical imaging is primarily used for diagnostic and therapeutic purposes related to human anatomy. Consequently, it is crucial for enhancing human health and therapeutic interventions [11]. Radiologists have identified Medical Resonance Image (MRI) as the predominant imaging modality for the identification of brain tumors. In comparison to other imaging modalities such as CT and X-ray, it provides enhanced resolution of soft brain tissues [13,14]. The four MRI modalities, namely T1, Contrast-Enhanced T1 (T1-CE), T2-weighted, and Fluid Attenuation Inversion Recovery (FLAIR), each provides specific phenotypes and features of the tumor, which aid in estimating survival times for patients with GBM [12].

Based on the type of tumor and the number of images, MRI can be segmented into multiple

datasets. The training of neural network models may then be accomplished with the help of this.

Currently, Artificial Intelligence (AI) offers sophisticated learning methodologies for developing Computer-Aided Diagnosis (CAD) systems that aid clinicians in diagnosing cancer or tumors using imaging data. AI technology enables robots to make judgments more efficiently than humans and autonomously complete complicated tasks with little to no human intervention. Artificial Intelligence encompasses several Machine Learning (ML) approaches, such as decision trees, support vector machines, Bayesian algorithms, artificial neural networks, regression models, and K-Nearest Neighbors. Deep neural networks, in contrast to artificial neural networks (ANNs), consist of several hidden layers organized in a hierarchical structure. These networks possess complex computations and activation functions that enable automated hierarchical feature learning. They are utilized in various domains, including voice recognition, surveillance, virtual assistance, anomaly detection, and healthcare, due to their ability to learn complex patterns from high-dimensional data. Deep learning (DL) denotes the class of methods and methodologies based on deep neural networks [15,16].

A vast number of images included in the datasets constitutes the greatest challenge when it comes to classifying MRI scans using specific neural networks. There is a possibility that the database may be expanded if every plane was used for MRI collection. To obtain the classification result, it is necessary to perform preprocessing on the MRI images before feeding them into the various networks. Convolutional Neural Networks (CNNs), which were developed to address this issue, offer several benefits, including the ability to bypass preprocessing and facilitate feature engineering. When a simpler network is used, there is a reduction in the amount of resources required for deployment and training. Due to the limited availability of resources, using the system for mobile platforms or medical diagnostics is an incredibly challenging endeavor. If the method is required for standard clinical diagnostic procedures performed daily, then it must be beneficial to everyone [10,17].

On the other hand, mathematical modeling is a valuable tool that can be used to consider the evolution of brain cancer and select the most effective course of treatment. Once the kind and severity of brain cancer have been identified, the selection of an appropriate therapy is among the most essential factors in determining whether or not the patient will survive. To describe, understand, and predict the short-term and long-term behavior of complex biological phenomena, such as the evolution of tumors and immune responses, mathematical modeling has proven to be a valuable tool. This has been demonstrated via the utilization of numerical simulations [18,19].

Chemotherapy, radiation therapy, and surgical procedures are the most common treatments applied to treat this condition. Several medications are used in the process of chemotherapy to eradicate cancerous cells that rapidly replicate. In order for therapy to be successful, it is vital to deliver an adequate quantity of medicine to tumor cells while simultaneously minimizing the amount of damage that is caused to healthy cells to an acceptable level [20]. Chemotherapy has long been the primary cancer treatment, particularly while the tumor is still in its early stages [18].

New therapies, particularly immunotherapy, are expected to enhance survival rates. The immune system is essential for protecting the body from damage. In addition to safeguarding against dangerous germs, it is a crucial element in detecting and eradicating altered cells, hence contributing to the prevention and retardation of malignant proliferation. Our immune system can eliminate gliomas while they are tiny; however, it becomes ineffective in preventing their proliferation as they increase in size [21,22].

Immunotherapy has recently emerged as a potentially viable treatment for cancer in many contexts [23]. This rapidly advancing cancer treatment strategy was established on the premise that enhancing the immune system may combat cancer. Employing biological components, it either

enhances the immune system or rectifies the damage inflicted by the disease. The basis of GB immunotherapy is the use of several immune cells, including natural killer (NK) cells, cytotoxic T lymphocytes, and dendritic cells. The latter are less hazardous than radiation and chemotherapy and have shown the highest cytotoxic efficacy against malignant tumor cells [22].

Mathematical models may also integrate the immune system's response, the evolving survival tactics of cancer cells, and the use of cancer therapies such as chemotherapy, immunotherapy, and cancer vaccines, among others. Cell-cell interaction models suggest that intermittent treatment is more successful than typical continuous therapy in postponing cancer recurrence [19]. Despite the challenging nature of the latter endeavor, intricate biological mechanisms associated with cancer proliferation and treatment have been thoroughly examined by mathematical modeling over the last three decades. As a result, enhanced supportive and chemotherapeutic treatment strategies have been proposed [24].

Since mathematical cancer models are multidimensional and nonlinear, iterative techniques are employed to evaluate their global dynamics, such as the Localization method of invariant compact sets (LMCIS) [25–28]. A few models from the present literature that meet the criteria mentioned above, and the LMCIS, will be discussed in the sections that follow.

1.1 Problem statement

The manual identification of brain tumors may be difficult, time-consuming, and imprecise because brain tumors come in a variety of sizes and forms. For identification that is both accurate and precise, expertise is essential, and the presence of complicated situations makes this process far more challenging [6, 14].

It is a significant challenge for diagnostic imaging to handle the increasing number of patients with enormous image volumes, which requires medical professionals to examine data in a timely and efficient manner [29].

Any tumor in the human body poses a serious risk to life; hence, the best course of therapy requires an early identification [15]. The precise classification of brain cancers has grown challenging owing to the existence of several types, such as glioma, meningioma, and pituitary tumors, each necessitating a specific treatment regimen [13].

1.2 Research Questions

The research questions that serve as the motivation for this thesis are:

1. How is the grade of a brain tumor determined?
2. What artificial intelligence methods are available for the classification of brain tumors?
3. How are the dynamics of brain cancer evaluated?
4. What treatments are applied to a high-grade brain tumor?

1.3 Hypothesis

Tumor cell reduction conditions can be effectively predicted using DL algorithms combined with mathematical modeling.

1.4 Objectives

This section outlines the general objective and the corresponding specific objectives of the current research.

1.4.1 General Objective

The objective is to evaluate the global dynamics of cell populations by using pre-trained DL algorithms and the compact invariant set localization approach. This will enable the determination of the tumor grade, which will ultimately aid in identifying appropriate therapies to reduce tumor cell proliferation.

1.4.2 Specific Objectives

Table 1.1: Specific Objectives and procedures to achieve them.

Research Question	Specific Objective
1	Search for public domain MRI image datasets.
2	Search for public domain DL Models.
1 , 2	Training Deep Learning Models.
3	Select a Brain cancer Mathematical Model.
3	Find the supremum and infimum limits for all the populations of cells involved in the model using the Localization Method, whose domain intersection contains all the compact sets.
3	Analyze the existence of the attraction set; as a function of the treatment parameter.
3	Analyze the properties of tumor cell elimination and tumor persistence using Lyapunov stability theory.
3 , 4	Determine the biological implications of the results obtained.
1 , 4	Test and validate the performance of Mathematical and DL models.

1.5 Justification

Accelerating the therapeutic process by timely and accurate identification might significantly enhance survival rates [6,10]. Thus, an automated technique for brain lesion diagnosis and categorization must be combined with human evaluation [6].

CNN and DL may significantly expedite the diagnostic procedure by automating and precisely executing the classification task [6,30]. Specialists in that field have suggested machine learning and DL methodologies for tumor diagnosis, grounded in known paradigms within the literature [15]. Particularly, CNN has been recommended in digital pathology [31].

Machine learning and DL have boosted various application sectors. Many research are improving medical image processing, which has developed tremendously. IT and its interaction with other industries are interested in AI and DL-based image processing. This is because image processing is versatile [32]. An important area of study that applies the above techniques is the automation of the segmentation and classification procedures for brain tumors [6].

Previous issues included a lack of MRI pictures and labels. This slowed training convergence and generalization. Several academic institutions and research centers addressed the public dataset problem. These universities offer comprehensive, regularly updated annotation databases. The BraTS database, from 2012 to the present, is an example [32,33].

DL technology has lately garnered significant interest as a way for identifying brain cancers using MRI images [6]. MRI is a medical imaging modality highly recommended for obtaining high-resolution images of brain tissue to categorize brain tumors [15,29]. Consequently, research into the creation of CAD systems for automatic and prompt illness detection has continued to be ongoing and has garnered significant interest in recent years. The CAD system can help medical professionals identify diseases quickly and accurately [5]. DL is one such method that allows for automatic picture classification with a high degree of accuracy [34]. If data availability and collection continue to improve, DL could ultimately become a valuable predictive tool for glioma patients [35].

Furthermore, the ability to describe, comprehend, and predict the short- and long-term behavior of complex biological processes has been significantly enhanced by mathematical modeling [18,19]. Finding the correct dosage, selecting the most effective therapeutic medicine or vaccine infusion method, and establishing treatment parameters are the primary challenges. It would be too expensive to address these difficulties empirically; hence, mathematical modeling is necessary [36]. Comprehending the complex nature of the cancer process can aid in pinpointing targets for molecular treatment, which has the potential to halt or even reverse the progression and spread of the illness [28].

This thesis is organized into five main chapters. Chapter 2 delineates the current state of the art, categorized into two primary methodologies: literature about deep learning techniques and that rooted in mathematical modeling, providing a comparative and contextual analysis of the issue at hand. Chapter 3 delineates the materials and methodologies utilized. This encompasses two suggested methodologies utilizing Convolutional Neural Networks (CNNs) for brain tumor classification: one for multiclass classification employing the Kaggle dataset, and another for binary classification using the BRATS 2019 dataset. An iterative approach for localizing compact invariant sets is presented, grounded on a mathematical model. Chapter 4 outlines the outcomes achieved for each methodology, encompassing performance measurements, computational complexity, Grad-CAM visualizations, and mathematical simulations across various therapeutic scenarios. Chapter 5 discusses the main contributions of the work, the study's limitations, and suggests possible future research directions.

CHAPTER 2

State of the art

2.1 Related work with Deep Learning approach

Deep learning (DL) has become an effective method to detect brain tumors using brain MRI data. Consequently, considerable research has been conducted on the topic, where authors have proposed new models or added characteristics to existing models to improve classification accuracy. For instance, in [31], a novel architecture for glioma classification was developed. A CNN with transformation stages, efficient smart junctions and feature combination modules was employed. Histopathological images were used to classify four glioma subtypes with 96.75% accuracy. Similarly, research [34] suggested using a CNN to extract information from MRI images and pass it to an SVM classifier. The proposed method achieved 96.19% accuracy for HGG glioma using the FLAIR modality and 95.46% for LGG using the T2 modality for the four glioma classes. The recommended solution outperformed similar strategies in the literature on BraTS 2018 dataset. In the same way, in [7] a dual CNN was suggested. The first module retrieved brain imaging characteristics, while the second categorized them. The training case used BraTS-IXI. To segment tumor sites in classified Gliomas, the Histogram-Density Segmentation Algorithm (HDSA) was created. They achieved 98.85% accuracy in identifying LGG and HGG. Likewise, in [4], the authors introduced a U-network segmentation model and a deep CNN architecture for automatic brain image categorization into four classes, utilizing six datasets. Testing and training the segmentation model allowed them to determine how segmentation affected brain MRI tumor categorization. The highest accuracy was 98.8%.

In another case, as reported in [13], an ARM-Net CNN was proposed for multiclass classification of brain tumors. They implemented an LGAM to RM-Net to capture widely distributed feature dependencies. In experiments, the ARM-Net achieved 96.64% accuracy on the MBTD dataset and 97.11% accuracy on BraTS 2020. The authors of [29] created a hybrid model using AlexNet and GRU neural networks to categorize cancers into four classes. The model accurately classified and diagnosed brain tumors with 97% accuracy. The authors utilized Msoud dataset from Kaggle.

In [15], a CNN model was developed and used with residual connections and starting modules. Experiments using two publicly available datasets of 4,600 and 253 brain images demonstrated a classification accuracy of 99% for the proposed architecture.

Reference [14] proposed a parallel deep convolutional neural network (PDCNN) architecture to mitigate overfitting by extracting global and local features from concurrent stages utilizing a dropout regularizer and batch normalization. Three kinds of MRI datasets were used to evaluate

the technique. The binary I-tumor identification dataset, Figshare-II, and Multiclass Kaggle-III have accuracies of 97.33%, 97.60%, and 98.12%, respectively. Another example is research [37], which presented an innovative customised CNN model, Glioma-CNN. It stands out as a lightweight CNN model compared to its predecessors. The research utilized the BraTS 2020 dataset, which consists of two classes, for its experiments. Integrated with the gradient boosting algorithm, GliomaCNN achieved an accuracy of 99.1569%.

Several articles also suggest transfer learning (TL). In particular, authors proposed using pre-trained models for the categorization task of brain tumors. In [16], the authors presented several advanced pre-trained TL models for the detection and diagnosis of brain tumors, including pituitary, meningioma, and glioma. TL approaches were evaluated using the publicly available SARTAJ MRI dataset from Kaggle. InceptionResNetv2 achieves an optimal accuracy of 98.91%. The research [38] introduced VGGNet, a pre-trained DCNN architecture. The proposed approach is compared to deep learning-based brain tumor classification algorithms. The training dataset was Figshare. The suggested method achieves 98.93% test accuracy.

The other case is Reference [9], where the authors evaluated the effectiveness of deep TL topologies in identifying brain cancers. This study uses InceptionV3, VGG19, DenseNet121, and MobileNet TL designs. They used data from figshare, SARTAJ, and Br35H to test the models. These databases classify glioma, meningioma, pituitary tumors, and no tumors. Experimental findings show that MobileNet achieves 99.60% accuracy, surpassing rival approaches.

Also, in [39], TL methods and deep learning architectures were compared for classifying adult-type diffuse gliomas. The authors achieved a balanced accuracy of 96.91%. Finally, they provided pathologists with a visualization tool that creates heat maps of tumor locations, helping them identify the most relevant sections. In [40], researchers found the optimum CNN architecture for brain tumor identification and classification by comparing DenseNet-201, Inception-V1, AlexNet, and MobileNetV2. This solved the issue of inaccurate or delayed diagnosis. The article's database includes over 3,000 Kaggle MRI images. MobileNetV2's 96.5% accuracy made it the best model throughout development.

Additionally, studies in the current literature suggest their model and subsequently evaluate its results against pre-trained models. In this case, a study [10] introduced a CNN model for categorizing different forms of pituitary, meningioma, and glioma. The model was evaluated against pre-trained methods that used a public Kaggle dataset. The experiment's outcomes demonstrated a high categorization accuracy of 98.04%. In the same year, [17] demonstrated the usage of pretrained CNNs and the training of a proposed CNN model. This study considered the classifications of glioma, meningioma, pituitary tumor, and non-tumors. The Msoud dataset, available on Kaggle, was used to test the CNN models. The experimental results of the proposed method demonstrated a remarkable classification accuracy of 97.84

The research [41] proposed a two-way parallel hierarchical diagnostic model based on pathomorphological features to achieve automatic clinical classification of gliomas. The model was verified on the clinical data samples provided by Liaoning Cancer Hospital and its accuracy reached 98.6%.

Study [42] introduced an EBT Deep Net DL model for the categorization of three distinct types of brain tumors. Pre-trained deep convolutional neural network models, including ResNet50V2, ResNet152, DenseNet201, MobileNetV3, and VGG19, were used. The suggested approach achieved an accuracy of 98.8%.

In [43], authors evaluated the precision of many pre-trained models. The majority of models attained optimal accuracy via TL, followed by a fine-tuning phase. The most effective model in this

investigation was EfficientNetB3, with an accuracy of 97.5%. The researchers determined that data augmentation did not enhance the overall accuracy of the models.

Research [44] introduces a lightweight, fine-tuned EfficientNetV2S convolutional neural network for the detection of brain tumors. The suggested pre-trained and fine-tuned model, based on EfficientNetV2S, attained exceptional training outcomes across three distinct datasets. An accuracy of 98.48% was attained.

The paper [45] suggested CNN Multi-Branch Networks with Inception Block. The use of the Br35H dataset, meticulously calibrated and tested, validated this complete technique. In classifying the four tumor types, the proposed model achieves an accuracy rate of 99.30% and a variance of 0.0005, demonstrating its superiority over current methods. In [46] a hybrid DL model using Graph Neural Networks (GNN) was presented to enhance brain cancer identification. A total of 10,847 public MRI images were used to test the model. Results revealed that the proposed model outperforms pre-trained models and CNN architectures, achieving an accuracy of 93.68%. As another classification approach, [47] proposed the Dual Attention method based on the Resnet-50 model with bidirectional gated recurrent unit (DA-ResBiGRU). Brain tumor MRI and Figshare datasets were utilized for experiments. The suggested model achieves 98.53% accuracy on the Brain Tumor MRI dataset and 99.3% accuracy on Figshare.

Other studies using pre-trained models include [48], [49], [50], and [51]. They utilized numerous approaches from the literature and suggested modifications or combinations of them to increase classification accuracy.

The following Table presents a comparison between state-of-the-art works, considering studies of pre-trained models and the datasets used, the number of classes, the best architecture, and the best accuracy obtained.

Table 2.1: Comparison of the state-of-the-art of work related to training DL models.

Reference	Dataset	Classes	Best architecture	Accuracy
Ref. [10]	Nangfang and General Hospital Tianjin, China	3	Proposed Model	98.04%
Ref. [16]	SARTAJ	3	InceptionResNetv2	98.91%
Ref. [38]	Figshare	3	VGGNet, a pre-trained DCNN	98.93%
Ref. [9]	Figshare, SARTAJ and Br35H	4	MobileNet	99.60%
Ref. [17]	Msoud dataset	4	Proposed Model	97.84%
Ref. [39]	Luxembourg National Health Laboratory	5	BYOL (ResNet50+ViT)	96.91%
Ref. [41]	Liaoning Cancer Hospital	3	MF-DPNet	98.60%
Ref. [42]	Figshare	3	EBT Deep Net	98.80%
Ref. [43]	Figshare, SARTAJ	3 , 4	EfficientNetB3	97.5%
Ref. [44]	Figshare, ERDOS,Fernando2rad	3, 12, 44	Fine-tuned EfficientNet-V2S	98.48%
Ref. [45]	Br35H dataset	4	Multi Branch Network	99.30%
Ref. [46]	SARTAJ, Msoud dataset	4	Brain-GCN-Net	93.68%
Ref. [47]	Brain MRI, Figshare	3 , 3	DA-ResBiGRU	99.30%
Ref. [48]	Kaggle Dataset	4	ResNet-18	99.90%
Ref. [49]	Msoud dataset	4	AlexNet-GRU	97%
Ref. [50]	Figshare, Br35H and SARTAJ combination	4	CNN-KNN	97.15%
Ref. [51]	Figshare, Br35H and SARTAJ combination	4	EfficientNet	98%

2.2 Related work with Mathematical Model approach

Recent research on cancer models has been used to determine the conditions required for the total eradication of cancer cells. Studies such as [3], have suggested models of cancer immunology and immunotherapy that describe an inherent CTL response to the formation of an immunogenic tumor and assess the efficacy of adoptive immunotherapy. Likewise, [21] analyzed a five-dimensional mathematical model to simulate glioma cell reactions to T11 target structure. The model predicted the recommended treatment duration to obtain glioma cell approval. A system analysis was conducted. In immunotherapy, macrophage and CD8+T cell counts increase while glioma cell proliferation decreases, according to numerical models.

According to [52], a three-dimensional mathematical model integrates oncolytic virotherapy with chemotherapy. Using a cancer-specific virus for virotherapy after the first or second chemotherapy session was the aim. The authors presented several simulations to illustrate their findings. With this combined therapy, gliomas may need fewer chemotherapy sessions. Another study that employed virotherapy is [53]. A three-dimensional model of oncolytic virotherapy for melanoma was created and evaluated. They began by analyzing the dynamics of tumor cells at the primary tumor site using an oncolytic virus. This was a local example of the model. The analytic findings were substantiated by numerical simulations, which also examined the impact of various factors on treatment outcomes.

To anticipate tumor growth, [20] combined the drug transport equation with tumor development and magnetism equations, using partial derivative equations. They evaluated three simulations: chemotherapy using magnetic drug targeting (MDT), chemotherapy without treatment, and tumor progression without treatment. Considering therapeutic duration. Their findings demonstrated that the dispersion of medication in tumor tissue significantly affected the efficacy of therapy.

In another study, [54] modeled tumor radius development before and after radiation therapy, utilizing a biologically inspired mathematical model to bridge gaps in previous models. They generated good fits using stochastic optimization on the tumor radius time series of 43 patient records. The model demonstrates how glioma cells become tumors, estimating the tumor's age. Similarly, Bekker et al. [55] analyze the biological response and immunomodulatory effects of radiation treatment before reviewing preclinical and clinical research to address these issues. Published mathematical models of radiation-tumor immunological interactions were examined. All these strategies emphasize personalized treatment. In [56] developed a mathematical model employing four ordinary differential equations (ODE) to predict LGG response to various radiation and therapy combinations, including temozolomide. From longitudinal imaging data on genuine LGG patients' response, patient-specific features were obtained. Simulations indicated that concurrent radiation and temozolomide were best for research subjects. In other treatment case, [57] proposed a simple four-dimensional ODE model. It was used to examine tumor development under ionising irradiation (IR) and anti-programmed death ligand 1 (anti-PD-L1) therapies. In cases of tumor persistence, anti-PD-L1 and IR may inhibit tumor growth over time. In [58] a mathematical model of triple negative breast cancer (TNBC) with checkpoint inhibitor treatment was presented. The model included two stable equilibria, reflecting cancer-free and big tumour states. The cancer-free equilibrium is locally unstable, but mathematical analysis and numerical simulation have shown that the model's immune system can eliminate a small tumor, providing immune monitoring.

In the case of immunotherapy, as presented in [59], an ODE-based model was proposed to account for the dynamics of multicellular conjugates and the binding of multiple Chimeric Antigen Receptor (CAR)-T cells to a single glioma cell during cancer treatment. The model more accurately represents empirical CAR-T cell lethal test results than models that ignore multicellular conjugates.

They also measured CAR-T cell proliferation, a key parameter of therapeutic effectiveness. Finally, the model demonstrated the distinct lethal behaviors of CAR-T cells in patient-derived brain tumor cells, varying from low to high antigen receptor levels. Another similar study is [60], where the authors used partial-integral differential equations to create a mathematical model. The model accurately predicted tumor and CAR-T cell dynamics for many haematological malignancies using clinical data. These pathways are also examined in conjunction with biological events, such as pre-existing or intended mutations, to gain a deeper understanding of resistance to CAR-T cell immunotherapy.

In [61], regulatory T cells were explored with an ODE model of chemo-immunotherapy with seven equations. Regulatory T cells are one way tumor cells fool the immune system. The incorporation of regulatory T-cell status into cancer mathematical modeling for chemo-immunotherapy cell simulation has improved the identification of important cases, which a simpler model cannot achieve.

Similarly, in [62], a mathematically based treatment program was presented. The mathematical model focuses on brain cancer chemo-immunotherapy using Interleukin-2 (IL-2). The interplay between chemotherapy and immunotherapy is also considered in this model to improve chemotherapy treatment. It achieves this by utilizing an analytical function to specify the therapy and tailor its application to each patient. The timing and dose of drug delivery affect its function. They employed the singular perturbed vector field (SPVF) approach to uncover the hierarchy of the system of equations and determine the equilibrium points and stability of the mathematical model. In [63] A mathematical model was devised to examine cancer cell dynamics after different treatments. The authors found equilibrium points and explored local stability to characterize the model's dynamic behavior. The simulations indicate that immunotherapy combined with chemotherapy controls tumor development more effectively than monotherapy. In other case [64] presented and analyzed a four-dimensional mathematical model for IL-2-based cancer immunotherapy. Researchers observed that treating IL-2 for a brief duration over several days lowers the tumor population for an extended period before reaching steady-state values. This suggests that periodic treatment of IL-2 may be an effective technique for tumor size management. In [65], the authors proposed a mathematical model to explore tumor-immune dynamics with three discrete time delays. A model with nine ODEs was suggested. To better understand tumor-immune dynamics, they added three discrete temporal delays to our deterministic system. The retarded and non-retarded systems, along with the Hopf bifurcation direction, were identified through stability analysis. Numerical simulations and parameter estimation methods supported the theoretical approach. In [66] researchers investigated the saturated M2 macrophage response using a tumor-macrophage interaction model with three differential equations. The authors determined the model's equilibrium point and examined local stability. They demonstrated that a stronger immune response may stabilize that system. Numerical simulations confirm the analysis.

The following works provided mathematical models of cancer and utilized LMCIS to evaluate its global dynamics. Firstly, this method was implemented in studies like [67] in where the authors proposed the localization of compact invariant sets in nonlinear systems. They developed a novel technique using first-order extremum conditions and symmetric prolongations. Their method developed the symmetric extension of the Rayleigh-Bénard convection system model, known as the Lorenz system.

After that, [68] applied the LMCIS to a five-dimensional melanoma model. In cellular immunotherapy, tumor cells interact with cytotoxic T lymphocytes and cytokines. Global stability

analysis yields global asymptotic criteria for melanoma eradication from these findings.

Additionally, study [26] employs LMCIS in conjunction with a cancer model approach. This study examines the ultimate dynamics of angiogenesis in the five-dimensional tumor growth model. One was chemotherapy alone, while the other had antiangiogenic medication. Global asymptotic tumor clearance was obtained for both.

In subsequent years, [27] developed a mathematical model for cancer. Using the LMCIS, the authors analyzed the global dynamics of the five structural equations that characterize the produced pancreatic cancer model without immunotherapy. It was essential to examine the ultimate dynamics of these equations to predict patient health.

In [19] explain chronic myelogenous leukemia using a dynamical system of three first-order ODEs and explore cellular immunotherapy as a therapeutic control strategy. The latter was achieved using Lyapunov stability theory and localization of compact invariant sets. Combining these two methods might generate immunotherapeutic treatment parameters that eliminate leukemia cancer cells.

Recently, in [28] examined the ultimate dynamics of a six-dimensional metastatic cancer model resistant to therapy. This model illustrates how chemotherapeutic medications affect both malignant and non-malignant cells in two primary and secondary tumors. Global asymptotic tumor eradication criteria were calculated using LMCIS.

The following Table presents a comparison between the state-of-the-art works realted with mathematical models.

Table 2.2: Comparison of the state-of-the-art studies that suggested and analyzed mathematical models of cancer.

Reference	Cancer Model	Number of Eq.	Treatment	Method
Ref. [3]	Glioblastoma model	6	Cytotoxic T lymphocytes CTLs	Stability analysis
Ref. [21]	Glioma model	5	Immunotherapeutic drug T11	Numerical simulations
Ref. [53]	Melanoma model	3	Virotherapy	Stability analysis
Ref. [57]	Tumor growth	4	IR and anti-PD-L1	Stability analysis
Ref. [58]	Breast cancer	8	Immunotherapy	Stability analysis
Ref. [59]	Glioma model	5	CAR T-Cells	Stability analysis
Ref. [60]	Haematological malignancies	4	CAR T-Cells	Numerical simulations
Ref. [61]	Tumor growth	7	T-Cells	Newton Method
Ref. [62]	Brain cancer	11	IL-2 in chemo-immunotherapy	SPVF
Ref. [54]	Glioma model	1	Radiotherapy	Stochastic optimization
Ref. [63]	Tumor growth	4	Immunotherapy with chemotherapy	Stability analysis
Ref. [64]	Tumor growth	4	IL-2 in Immunotherapy	Stability analysis
Ref. [65]	Tumor growth	9	Immunotherapy with IL-12	Stability analysis
Ref. [66]	Tumor growth	3	Immunotherapy	Stability analysis
Ref. [68]	Melanoma cancer model	5	Immunotherapy	LMCIS
Ref. [26]	Tumor growth	5	Chemotherapy	LMCIS
Ref. [27]	Pancreatic cancer	5	No treatment	LMCIS
Ref. [19]	Chronic myelogenous leukemia	3	Immunotherapy	LMCIS
Ref. [28]	Metastatic cancer model	6	Chemotherapeutic medicines	LMCIS

CHAPTER 3

Materials and Methods

3.1 Proposed Deep Learning technique for multiclass classification

The Google Colab platform and Python programming language version 3.8.10 are used for developing preprocessing procedures. TensorFlow version 2.9.2 is used. The Google Colab platform utilizes the NVIDIA A100-SXM4-40 GB, a professional-grade graphics card.

In contrast, classification is crucial since it categorizes images into distinct categories. This is the preliminary phase in forecasting a locale with anomalies in illness diagnosis [69]. The suggested methodology comprises four main steps. The study dataset is obtained from the Kaggle database [70]. This dataset comprises three distinct datasets, which will be described in the following sections. The dataset undergoes preprocessing using many methods, including resizing, labeling, and data augmentation techniques such as rotation, scaling, and brightness adjustment. Subsequently, the training and validation methodologies are executed using the Generic CNN model alongside pre-trained CNN models. Figure 3.1 illustrates the models used in this work to assess their performance using the same dataset for the suggested CNN models. Similarly, the assessment is undertaken to confirm that the training was executed accurately. The test is conducted by creating a test dataset including distinct images from the dataset used for training and validation.

Accuracy, precision, recall, specificity, and area under the curve (AUC) are some of the major performance measures that are used in the last step of the evaluation process for the suggested models so that results may be evaluated. A comparison is made between the performance of the model and that of pre-trained models, and the percentage of losses incurred during training is also confirmed. To identify which model performed better with the dataset that was provided, all of those that were described above might be considered.

3.1.1 Preprocessing

This study suggests the following preprocessing techniques for the dataset: Resizing, Labeling, and Data Augmentation (including Rotation, Zoom, Brightness, and Random flips), as seen in Figure 3.1. The methods of Rotation, Zoom and Random flips were used as Position Augmentation techniques. Brightness was used as a Color Enhancement Technique.

The preprocessing approaches started with the declaration of a dictionary using the Python function *dict()*. This dictionary has been given a name and may be used to generate a new dataset containing its attributes. This aggregation of arguments should be conducted at the beginning of

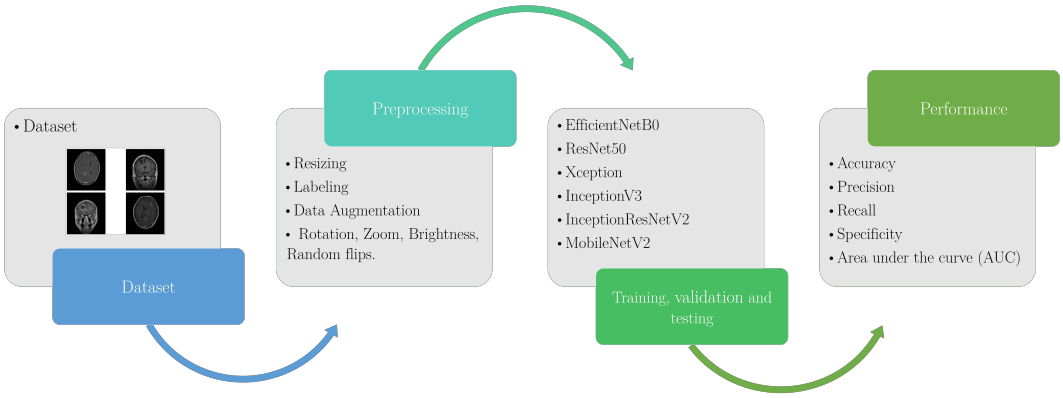

Figure 3.1: Flowchart illustrating the proposed methodology for brain tumor classification.

this phase to avert superfluous code in the instructions of this stage. Deep neural networks require inputs of a designated size; therefore, it is essential to resize all photos before inputting them into CNN classification models. Consequently, the first method used was Resizing, which utilizes the *rescale* parameter, a Python function parameter. Subsequently, the labeling step is executed. This technique involves assigning labels to each class. The number of created labels is contingent upon the number of classes addressed by each research study. For this study, the designations of the four classes (Glioma, Meningioma, No-tumor, and Pituitary) and their associated images were determined and assigned.

On the other hand, Data Augmentation is a crucial methodology for addressing the challenges of unbalanced distribution and data sparsity. Many research investigations on brain tumor classification have used this approach, which integrates geometric transformation operations such as rotation, scaling, and brightness adjustment. At this step, the Keras *ImageDataGenerator()* method was used to generate images. Three rotation parameter functions are suggested. One is *rotation_range*. Set the random picture rotation degree range using this parameter. *horizontal_flip* also rotates the picture. It randomly flips inputs horizontally. *shear_range* randomly alters the shear angle counterclockwise in degrees, hence it was employed. Zoom or Scale randomly zooms in or out on each dataset picture using the *zoom_range* parameter.

The *brightness_range* parameter was used to vary brightness levels, resulting in changes to random brightness intensity for each dataset picture. Table 3.1 presents the suggested parameters for preprocessing the CNN models. For comprehensive information on the preprocessing settings, please consult the references [9, 10, 69]. Utilizing more characteristics may elevate the difficulty of the training. Finally, Weights & Biases (wandb) was used to monitor the training in real time.

Table 3.1: Parameter values for the preprocessing stage for each CNN model.

Parameter	Value
Rescale	1.0/255
Rotation	10
Horizontal flip	True
Zoom	0.1
Shear range	0.1
Brightness range	0 to 0.7
Labeling	4 Labels

3.1.2 Pre-Trained CNN Models

The models in this research are simulated using the Python programming language inside Google Colaboratory. The parameter configurations are specified as follows: learning rate: 0.0001, dropout rates: 0.3 and 0.4, batch size: 16, epochs per K-fold: 10, optimizer: SGD, and activation functions: ReLU and Softmax. Table 3.2 presents details on the hyperparameters for this model. These hyperparameterswere chosen according to the state of the art [9, 10, 29, 41–43, 45–49, 69]

Table 3.2: Hyper-parameter values for training the Generic CNN model.

Hyper-Parameter	Value
Activation function	ReLU
Initial learning rate	0.0001
Optimizer	SGD
Batch size	16
Dropout rate	0.3-0.4
Epochs	10
Train-test split	70–30%
Output activation function	Softmax

This study examines several publicly available models in the pre-trained network technique, including ResNet50, Xception, InceptionV3, EfficientNetB0, InceptionResNetV2, and MobileNet v2.

ResNet50: The ResNet versions secured the top position in the ImageNet-based ILSVRC 2015 ranking competition. The architecture is detailed in [71]. They are now employed in various machine vision-related operations. The design employs an input dimension of 224×224 and may be adjusted to 256×256. ResNets utilize direct connections to bypass many network layers, thereby streamlining the network and enhancing the learning process. A correlation exists between the residual network and feature inference. ResNet also addresses the problem of diminishing Precision. This work employs ResNet50 as a model for transfer learning. TL is versatile; the pre-trained model is used immediately for picture identification. The model is trained using the dataset analyzed in this work, and a fourth layer of neurons is included due to the dataset's four classifications.

Xception: CNN Xception [72] employs point convolution and depth convolution. It is unnecessary to perform a convolution on all channels in this configuration. This reduces the number of connections and, consequently, the number of parameters. Similar to ResNet, it utilizes residual

connections to enhance accuracy. The process comprises input flow, middle flow, and exit flow. The input size of this architecture is 256×256. The Xception model's architecture is easily adaptable. The pre-trained version of the Xception approach, having been trained on the ImageNet dataset, is capable of classifying new tasks [73].

InceptionV3: InceptionV3 is a variant of the Inception family of deep neural networks. This is a consequence of the improvements made in the original Inception design. It is a more profound network due to its configuration of limited connections. It mostly consists of several Inception modules. Every module obtains input from the previous module. This design has 48 layers and has an input dimension of 299 x 299, which is subject to modification. The included pre-trained Inceptionv3 model is trained on the ImageNet dataset and can categorize photos of one thousand unique objects [74].

Efficientnet_b0: In [75] the EfficientNet network as a scaling solution was presented . This network achieves more precision by securing a balance between the network's height, depth, and input resolution. The network uses an input size of 224 × 224, while the modified network takes advantage of an input size that can be as large as 256 × 256.

InceptionResNetV2: Rather of utilizing the original Inception blocks, this network makes use of modified Inception blocks. Additionally, it adds a filter expansion layer after each Inception block that utilizes convolution without activation. Batch normalization is used on top of the representative layers in order to increase the total number of Inception blocks. The picture that is being processed by this network has a resolution of 299 × 299 pixels [16].

MobileNetv2: The input picture dimensions for MobileNetV2 are 224 × 224 pixels. This model's processing efficiency makes it more appropriate for real-time and mobile applications. The swift performance of the Mobilenetv2 model is partially attributable to the implementation of point-wise and depthwise convolution techniques. The network utilizes the residual connections among the bottlenecks. The Mobilenetv2 architecture has an initial layer with 32 convolutional filters, followed by bottleneck layers of 19 filters each [76].

3.1.3 Brain Tumor Kaggle Dataset

The publicly available MRI dataset from the Kaggle repository was leveraged for the training, validation, and testing of the various TL-based approaches applied in this study, along with the model. The Brain Tumor MRI dataset Msoud [70] comprises three publicly available datasets enumerated below:

1. Fighshare [77]
2. SARTAJ [78]
3. Br35H [79]

All prior datasets are publicly accessible in the Kaggle repository.

The dataset details are shown in Table 3.3. This collection comprises 7,023 grayscale and JPG format MRIs of the human brain, including various varieties. The dataset comprises four categories of brain tumors: Glioma (1321 training images, 300 testing images), Meningioma (1339 training images, 306 testing images), No-tumor (1595 training images, 405 testing images), and Pituitary (1457 training images, 300 testing images). For the training and validation tasks, 80% and 20% of the photos were used, respectively. During the preparation phase, Resizing and Data Augmentation

were implemented on the dataset to ensure an appropriate input size for each model and to enhance the picture quantity available for usage. A total of 9,139 images were generated, with 70% allocated for training and 30% for testing.

Table 3.3: Dataset details.

Classes	Images for Training	Images for Testing
Glioma	1321	300
Meningioma	1339	306
No-tumor	1595	405
Pituitary	1457	300
Total	5712	1311

Figure 3.2 illustrates many examples of the images included in the dataset:

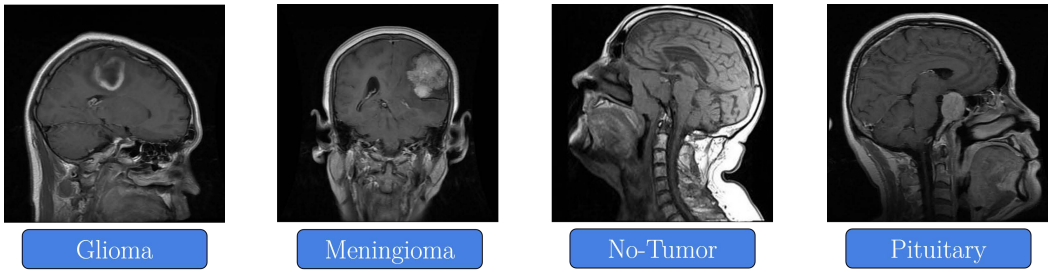

Figure 3.2: MRIs categorized in the Msoud dataset.

3.1.4 Performance Metrics

The performance metrics listed below are used in references such as [9,10,29,41–43,45–49,69,80].Additionally, they will be employed in the subsequent technique of this thesis work.

Equation (3.1) is used to determine the accuracy of classification, which is defined as the percentage of accurate predictions relative to the total number of data items:

$$Accuracy = \frac{TP + TN}{TP + FP + TN + FN} \tag{3.1}$$

Precision may be defined as the percentage of optimistic predictions that fall into the category of being always positive. The equation that represents the value of precision is equal to (3.2):

$$Precision = \frac{TP}{TP + FP} \tag{3.2}$$

Recall is determined by dividing the number of true positive (TP) outcomes by the total number of components in the positive class. The formula for *Recall* is given by (3.3):

$$Recall = \frac{TP}{TP + FN} \tag{3.3}$$

Likewise, the real negative rate is the likelihood of obtaining a negative test result, given that the subject is genuinely negative. The Specificity described by Equation (3.4):

$$Specificity = \frac{TN}{(FP + TN)} \tag{3.4}$$

Finally, we will display the proportion of losses as well as the AUC score, which reflects the model's capacity to differentiate between distinct classes, with a larger number indicating better performance.

For the equations above: True Positive (TP) is the number of anticipated positive cases that are, in fact, positive. True Negative (TN) is the number of anticipated negative cases that are in fact negative. False Negative (FN) is the number of expected negative situations that are in fact positive; it is also known as (type two) error. False Positive (FP) is the number of expected positive cases that are in fact negative; it is also known as (type one) error [69].

3.2 Proposed method for binary classification

In the preceding Section 3.1, a multi class classification approach for four distinct forms of brain tumors was developed. The aforementioned strategy aims to distinguish glioma tumors from other tumor types. This section aims to train and evaluate another six deep learning algorithms for the classification of brain tumors into two classes (LGG and HGG) across imaging settings, using deep artificial vision and TL methodologies. The metodology of this study is displayed in the Figure 3.3.

The proposed technique consists of four primary components. Initially, The dataset used was developed initially. The BRATS 2019 dataset will be delineated in the following parts. The dataset is preprocessed using several approaches, including labeling, resizing, color adjustment, rotation, and random flipping. Thereafter, the training and validation methods are implemented using the pre-trained CNN models. Figure 3.3 depicts the models used in this study to evaluate their efficacy. The validation was performed to verify that the training was done correctly. The test was conducted by generating a test dataset including unique images from the dataset used for training and validation. The effectiveness of the proposed models is assessed by important performance metrics, such as Accuracy, Precision, Recall, F1-Score, and Matthews correlation coefficient (MCC). The performance was assessed in comparison to pre-trained models. All previously stated models were assessed to determine which demonstrated higher performance with the designated dataset.

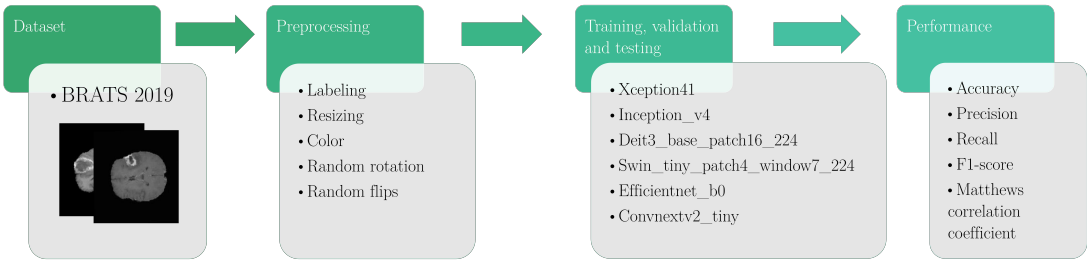

Figure 3.3: Flowchart depicting the methodology suggested in this section for the classification of high-grade gliomas (HGG) and low-grade gliomas (LGG).

3.2.1 Preprocessing

This preprocessing stage was developed in Google Colab, including GPU and TPU, enabling expedited model training compared to CPU. This section of thesis work use the NVIDIA A100 GPU. Programming language Python 3. The libriries used are PyTorch, scikit-learn, and Weights & Biases (wandb) for the purpose of tracking and monitoring the training process. Image data augmentation was performed to enhance the robustness of the dataset.Data Augmentation included Labeling, Resizing, Random Color, Random rotation and Random flips. The following Table 3.4 shows the values assigned in the data augmentation stage.

Table 3.4: Settings used for image data augmentation.

Augmentation	Setings
Resize	224 × 224 pixels.
Rotation	30%.
Brightness	Randomly adjusted within a range of 0 to 20%.
Contrast	Applied randomly from 0 to 20%.
Saturation	Randomly used, ranging from 0 to 20%.
Horizontal flip	The train subset folder is flipped horizontally.
Vertical flip	The train subset folder is flipped vertically.

3.2.2 Pre-Trained CNN Models

Table 3.5 establishes the hyperparameters that models in this section used. The epochs have been restricted to a maximum of 10. The batch size is restricted to 32 and 64. The authors choose to start with a modest dataset, with data size constrained between 10% and 25%; thereafter, they chose to proceed with 50% and 75%. The used optimizer is Adam (an abbreviation for Adaptive Moment Estimation), with an initial learning rate varying from 1×10^{-5} to 1×10^{-3}. The used learning rate scheduler is ReduceLROnPlateau, which modifies the starting learning rate at each epoch [80].

Table 3.5: Hyperparameters employed during the training.

Parameter	Value
Epochs	10
Batch size	32, 64
Data size	10%, 25%, 50%, 75%
Initial learning rate	1×10^{-5}, 1×10^{-3}
Optimizer	Adam
Learning rate scheduler	*ReduceLROnPlateau*

Following is a description of the pre-trained models that were used in this section:

Inception_v4: The inception_v4 architecture was developed by Google in 2014. The fundamental premise of Inception involves using many concurrent branches to implement diverse con-

volutional layers, therefore gathering input across numerous dimensions and levels of abstraction. Inception_v4 introduces improvements over its predecessors with the use of factorized convolutions, residual connections, and label smoothing [80, 81].

Xception41: The Xception41 architecture is derived from Inception. Xception41 employs depthwise separable convolutions. This technique approximates Inception modules using depthwise separable convolutions, consisting of a depthwise convolution applied to each channel independently, followed by a pointwise convolution that amalgamates channels via a 1×1 convolution operation. [73].

Data efficient image transformer: In 2017, Google introduced the deit3_base_patch16_224 architecture for Natural Language Processing (NLP). Transformers use self-attention to prioritize elements of the input sequence during prediction. Vision transformers (ViT) are well recognized. Transformer-based models may be enhanced by transferring knowledge from a larger, pre-trained teacher model to a smaller student model, therefore accelerating training while maintaining accuracy [82]

Swing transformer: The "swing attention" method is included during the sequence processing by the swing_tiny_patch4_window7_224 architecture. This method preferentially focuses on a selection of locations that shift within the sequence. This method facilitates the discovery of long-range linkages while concurrently reducing attention expenses [83].

Convnextv2_tiny: This architecture is a modification of the ResNet50 framework, integrating the benefits of convolutional networks with vision transformers to provide a more efficient structure. It incorporates self-supervision methods, masked autoencoders, and a Global Response Normalization (GRN) layer, leading to enhanced performance. ImageNet and the Large Scale Visual Recognition Challenge (ILSVRC) serve as public datasets used for the training and assessment of these models [84].

In this method is also used the Efficientnet_b0 architecture, as detailed in the preceding Section 3.1.

3.2.3 BRATS 2019 dataset

Images of the brain obtained from MRI are taken from the Brain Tumor Segmentation (BraTS) 2019 dataset [85]. T1, T1-Contrast Enhanced (T1ce), T2, and FLAIR are the four separate forms of contrast-enhanced brain imaging that are included in the BraTS 2019 dataset. Because of the improved contrast of the T1ce brain photos from this dataset, this research used them. This modality is the most often employed in cancer for the purpose of tumor identification [7]. There are 335 images of the brain that make up the T1ce type. These photos are divided into two categories: 259 high-grade glioma (HGG) images and 76 low-grade glioma (LGG) images. During the training phase, the T1ce approach was used, and 335 patient cases representative of both groups were investigated. Using a segmentation method, the slices of each photo in the dataset were viewed, and the ideal slices that portrayed the tumor lesion were chosen. As a result, 1074 axial slice images were obtained for the HGG class, and 1111 axial slice images were obtained for the LGG class.

for the testing dataset 10% of the photographs from each category were chosen, which resulted in a total of 108 images taken from the HGG category and 111 images taken from the LGG category. The following Figure shows some of the images that are included in the dataset.

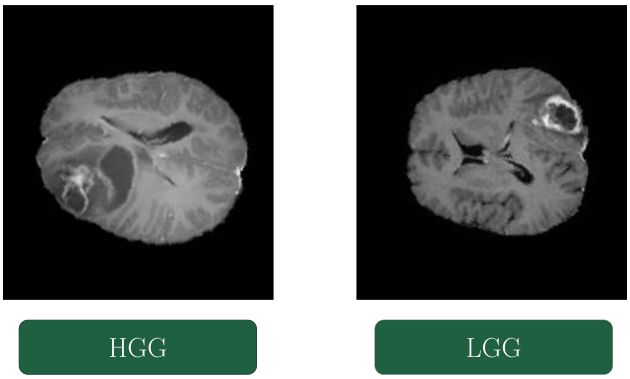

Figure 3.4: Sample of MRIs included in BRATS 2019 dataset.

3.2.4 Performance Metrics

The performance measures for the models used in this binary classification segment include accuracy (3.1), precision (3.2), and recall (3.3), which are derived from the preceding section 3.1. In addition, F1-score and Matthews correlation coefficient.

The F1 value measure combines Precision and Recall into a single comprehensive value. Neither Precision nor Recall can independently evaluate the whole matter. We may exhibit great precision with poor recall, or conversely, low precision with strong recall. The F1 Score amalgamates both issues into a one statistic. Upon computing Precision and Recall for a binary or multiclass classification task, the two metrics may be combined to get the F1-Score, as described in equation (3.5).

$$F1 - Score = \frac{2 \times Recall \times Precision}{(Recall + Precision)} \tag{3.5}$$

The Matthews Correlation Coefficient (MCC) measures the accuracy of binary classifications [86]. It is especially beneficial when the courses are imbalanced. The MCC is determined using the following equation (3.6):

$$MCC = \frac{TP \times TN - FP \times FN}{\sqrt{(TP + FP)(TP + FN)(TN + FP)(TN + FN)}} \tag{3.6}$$

3.3 Iterative Method of localization of Compact Invariant Sets

3.3.1 Model description

This section discusses the mathematical model of glioblastoma tumor and the immune system interactions delineated in [1], [2], and [3] clarifying the significance of each representation. Starting with the equation (3.7) that defines the dynamics of the tumor.

$$\frac{dT}{dt} = rT\left(1 - \frac{T}{K}\right) - a_T \frac{M_I}{M_I + e_T} \cdot \left(a_{T,\beta} + \frac{e_{T,\beta}(1 - a_{T,\beta})}{F_\beta + e_{T,\beta}}\right) \cdot \frac{C \cdot T}{h_T + T} \tag{3.7}$$

In the case of the following Equation (3.8), it describes the dynamics of CTL cells.

$$\frac{dC}{dt} = \left(\frac{a_{C,M_{II}} M_{II} \cdot T}{M_{II} \cdot T + a_{C,M_{II}}}\right) \cdot \left(a_{C,\beta} + \frac{e_{C,\beta}(1 - a_{C,\beta})}{F_\beta + e_{C,\beta}}\right) - \mu_c \cdot C + S \tag{3.8}$$

For the following case, cytokine dynamics are described by equations (3.9) and (3.10). Equation (3.9) describes the dynamics of TGF$-\beta$ in the brain. Equation (3.10) describes the dynamics of IFN$-\gamma$.

$$\frac{dF_\beta}{dt} = g_\beta + a_{\beta,T} \cdot T - \mu_\beta \cdot F_\beta \tag{3.9}$$

$$\frac{dF_\gamma}{dt} = a_{\gamma,C} \cdot C - \mu_\gamma \cdot F_\gamma \tag{3.10}$$

The dynamics of class I MHC cells is represented by the equation (3.11). Finally the equation (3.12) is used to represent the dynamics of class II MHC cells.

$$\frac{dM_I}{dt} = g_{M_I} + \frac{a_{M_{I,\gamma}} \cdot F_\gamma}{F_\gamma + e_{M_{I,\gamma}}} - \mu_{M_I} \cdot M_I \tag{3.11}$$

$$\frac{dM_{II}}{dt} = \frac{a_{M_{II,\gamma}} \cdot F_\gamma}{F_\gamma + e_{M_{II,\gamma}}} \cdot \left(\frac{e_{M_{II,\beta}} \cdot (1 - a_{M_{II,\beta}})}{F_\beta + e_{M_{II,\beta}}} + a_{M_{II,\beta}}\right) - \mu_{M_{II}} \cdot M_{II} \tag{3.12}$$

3.3.2 Detailed explanation of the variables, parameters, and initial conditions that have been suggested

The data shown in Table 3.6 summarizes the variables and parameters of the model defined in [2], along with their explanations.

Table 3.6: Summary of variables and parameters with their descriptions.

Variable	Description
T	Tumor cell numbers at any moment.
C	CTL recruitment from the peripheral blood system.
F_β	Dynamics of TGF-β (F_β) in the brain compartment.
F_γ	Dynamics of IFN-γ.
M_I	Dynamics of MHC class I receptor molecules on a single tumor cell.
M_{II}	Dynamics of MHC class II receptor on a single APC.
Parámeter	**Description**
K	Maximal tumor cell burden.
r	Tumor growth rate.
h_T	Standing for the accessibility of the tumor cells to CTL.
a_T	The maximal efficiency of a CTL.
e_T	The dependence on M_I.
$e_{T,\beta}$	The dependence on F_β.
μ_c	Constant death rate.
S	rate of infusion of primed CTL directly to the tumor site.
g_β	Natural basal level production of bioactive $TGF-\beta$ in the CNS.
$a_{\beta,T}$	Release rate per tumor cell.
μ_β	The degradation of $TGF-\beta$.
F_γ	Linear production of $IFN-\gamma$.
$a_{\gamma,C}$	Release rate per single CTL.
μ_γ	Constant rate of degradation of F_γ.
g_{M_I}	Basal rate of M_I receptor expression per tumor cell
$a_{M_{I,\gamma}}$	Maximal effect of $IFN-\gamma$.
μ_{M_I}	Constant rate of degradation of M_I.
$\mu_{M_{II}}$	Constant rate of degradation of M_{II}.

The initial conditions and other values of the parameters of the model used in this analysis were those proposed by the authors in [2] and [3].

3.3.3 Scheme of the mathematical model

An illustration of a schematic depiction of the relationships that are represented by the mathematical model with immunotherapy may be seen in Figure 3.5. The blood-brain barrier (BBB) is sometimes traversed by endogenous CD4+ and CD8+ lymphocytes. These lymphocytes interact with MHC class II on the surface of antigen-presenting cells (APC), which in turn makes it easier for cytotoxic T lymphocytes (CTL) to get activated and recruited. Activated CTL are able to remove MHC class I molecules that are present on the surface of tumor cells by adhering to them. TGF-β is secreted by tumor cells, while CTLs generate IFN-γ. However, TGF-β decreases the permeability of the blood-brain barrier (BBB), as well as the production of MHC II molecules and the activity of T-lymphocytes. At the same time as it activates MHC I and II molecules, IFN-gamma enhances the permeability of the BBB.

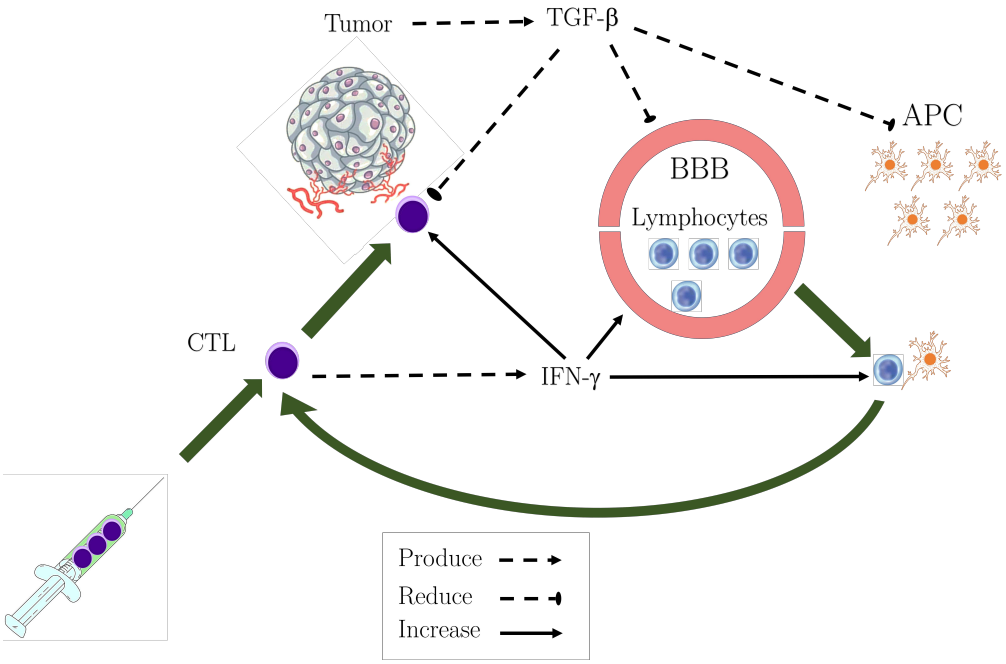

Figure 3.5: Illustration of the interactions of the variables in the mathematical model [1].

3.3.4 Proposed Algorithm

As shown in previous studies [28, 87], the algorithm of the invariant compact set localization method is shown in Table 3.7.

Table 3.7: The algorithm of the invariant compact set localization method.

Given the system of nonlinear equations $\dot{x} = f(x)$
1. Selecting the initial vector x_0.
2. The supreme and minimum limits are determined for $i = 1, 2, 3, 4, 5, 6$.
$x^{(1)}_{imax} := h_{i,sup} = max(h_i\|_{S(hi)})$;
$x^{(1)}_{imin} := h_{i,inf} = min(h_i\|_{S(hi)})$;
3. The supreme and minimum limits are refined for $i = 1, 2, 3, 4, 5, 6$ iteratively.
$x^{(2)}_{imax} := h_{i,sup} = max(h_i\|_{S(hi)\cap\Pi_i})$;
$x^{(2)}_{imin} := h_{i,inf} = min(h_i\|_{S(hi)\cap\Pi_i})$;
4. The domain of attraction
$K^{(n)}_i = \{x^{(n)}_{imin} \le x^{(n)}_i \le x^{(n)}_{imax}\}$; $i = 1, 2, 3, 4, 5, 6$; $n \ge 1$
will tend to the solution of $f(x) = 0$
Where i = order of occurrence of the supremum and infimum equations
and n = the number of iterations

For the purpose of facilitating clear manipulation for the purposes of simulation and analysis of the components involved, the equation system (3.13) that is described below is utilized:

$$
\begin{aligned}
\dot{x}_1 &= a_1 x_1 \left(1 - \frac{x_1}{a_2}\right) - a_3 \left(\frac{x_5}{x_5 + a_4}\right)\left(a_5 + \frac{a_6(1 - a_5)}{x_3 + a_6}\right)\left(\frac{x_2 x_1}{a_7 + x_1}\right), \\
\dot{x}_2 &= \left(\frac{a_8 x_6 x_1}{x_6 x_1 + a_9}\right)\left(a_{10} + \frac{a_{11}(1 - a_{10})}{x_3 + a_{11}}\right) - a_{12} x_2 + S, \\
\dot{x}_3 &= a_{13} + a_{14} x_1 - a_{15} x_3, \\
\dot{x}_4 &= a_{16} x_2 - a_{17} x_4, \\
\dot{x}_5 &= a_{18} + \left(\frac{a_{19} x_4}{x_4 + a_{20}}\right) - a_{21} x_5, \\
\dot{x}_6 &= \left(\frac{a_{22} x_4}{x_4 + a_{23}}\right)\left(\frac{a_{24}(1 - a_{25})}{x_3 + a_{24}} + a_{25}\right) - a_{26} x_6.
\end{aligned}
\tag{3.13}
$$

Six dynamic variables of the equations system (3.13) are considered: x_1, the tumor cell dynamics (T), tumor cell numbers in any moment. x_2, the CTL cells dynamics (C). x_3, the dynamics of TGF$-\beta$ (F_β). x_4 describes the dynamics of IFN_γ (F_γ). x_5, represent the dynamics of MHC class I (M_I),receptor of molecules on a single tumor cell. x_6 represents the dynamics of MHC class II (M_{II}), receptor on a single APC. Furthermore, it takes into account the impact of the dose of S, aCTL cells immunotherapy given to patients whose concentration is quantified in terms of the number of cells per dosage. In equations system (3.13), the following parameters were used a_j, $j = 1, ..., 26$, which depend on the biological parameters given in [2] through the following expressions:

$$
\begin{array}{lll}
a_1 = r; & a_2 = K; & a_3 = a_T; \\
a_4 = e_T; & a_5 = a_{T,\beta}; & a_6 = e_{T,\beta}; \\
a_7 = h_T; & a_8 = a_{C,M_{II}}; & a_9 = e_{C,M_{II}}; \\
a_{10} = a_{C,\beta}; & a_{11} = e_{C,\beta}; & a_{12} = \mu_C; \\
a_{13} = g_\beta; & a_{14} = a_{\beta,T}; & a_{15} = \mu_\beta; \\
a_{16} = a_{\gamma,C}; & a_{17} = \mu_\gamma; & a_{18} = g_{M_I}; \\
a_{19} = a_{M_{I,\gamma}}; & a_{20} = e_{M_{I,\gamma}}; & a_{21} = \mu_{M_I}; \\
a_{22} = a_{M_{II,\gamma}}; & a_{23} = e_{M_{II,\gamma}}; & a_{24} = e_{M_{II,\beta}}; \\
a_{25} = a_{M_{II,\beta}}; & a_{26} = \mu_{M_{II}}. &
\end{array}
$$

3.3.5 Invariant Compact Set Localization Method procedure

First, it is established:

Proposition 5.1. *All compact sets invariant in* $\mathbf{R}^4_{+,0}$ *are located in the bounded set* Π_1 *defined by* $\Pi_1 = \cap_{i=1}^4 K_i^{(1)}$ *and*

$$K_1^{(1)} = \{0 \le x_1 \le a_2\};$$

$$a_{10} \ge 1 : K_2^{(1)} = \left\{0 \le x_2 \le \frac{a_8 a_{10}}{a_{12}}\right\};$$

$$a_{10} < 1 : K_2^{(1)} = \left\{0 \le x_2 \le \frac{a_8}{a_{12}}\right\};$$

$$K_3^{(1)} = \left\{\frac{a_{13}}{a_{15}} \le x_3 \le \frac{a_{13}}{a_{15}} + a_{14}\frac{a_2}{a_{15}}\right\};$$

$$K_4^{(1)} = \left\{0 \le x_4 \le \frac{a_{16} a_8}{a_{17} a_{12}}\right\};$$

$$K_5^{(1)} = \left\{\frac{a_{18}}{a_{21}} \le x_5 \le \frac{a_{18}}{a_{21}} + \frac{a_{19}}{a_{21}}\right\};$$

$$a_{25} \ge 1 : K_6^{(1)} = \left\{0 \le x_6 \le \frac{a_{22} a_{25}}{a_{26}}\right\};$$

$$a_{25} < 1 : K_6^{(1)} = \left\{0 \le x_6 \le \frac{a_{22}}{a_{26}}\right\};$$

Test. The method of Localization of the Compact Invariant Sets is applied to the system of differential equations.

Tumor cells dynamics T. The localizer function is applied to define a domain in which the Tumor cells T is bounded, $h_1 = x_1$. The following set is obtained:

$$S(h_1) = \left\{a_1 x_1 \left(1 - \frac{x_1}{a_2}\right) - a_3 \left(\frac{x_5}{x_5 + a_4}\right)\left(a_5 + \frac{a_6(1 - a_5)}{x_3 + a_6}\right)\left(\frac{x_2 x_1}{a_7 + x_1}\right) = 0\right\};$$

From which the following formula is determined:

$$h_1 \mid_{S(h_1)} = a_1 \left(1 - \frac{x_1}{a_2}\right) - a_3 \left(\frac{x_5}{x_5 + a_4}\right)\left(a_5 + \frac{a_6(1 - a_5)}{x_3 + a_6}\right)\left(\frac{x_2}{a_7 + x_1}\right); \tag{3.14}$$

which represents the constraint of the proposed locator function in the set $S(h_1)$. Next, the principle of extrema is applied to obtain the localization set:

$$K_1^{(1)} = \{0 \le x_1 \le a_2\}. \tag{3.15}$$

CTL dynamics C. To define a domain in which the dynamic of CTL cells C is bounded, the locator function is applied $h_2 = x_2$. The following set is obtained:

$$S(h_2) = \left\{ \left(\frac{a_8 x_6 x_1}{x_6 x_1 + a_9} \right) \left(a_{10} + \frac{a_{11}(1 - a_{10})}{x_3 + a_{11}} \right) - a_{12} x_2 + S = 0 \right\};$$

From which the following formula is determined:

$$h_2 \mid_{S(h_2)} = \left(\frac{a_8 x_6 x_1}{a_{12} x_6 x_1 + a_9} \right) \left(a_{10} + \frac{a_{11}(1 - a_{10})}{x_3 + a_{11}} \right); \tag{3.16}$$

which represents the constraint of the proposed locator function in the set $S(h_2)$. From the above, it can be seen that there are two cases to consider: $a_{10} \ge 1$ and $a_{10} < 1$ respectively.

Applying the principle of extrema to obtain the location set in each case, one has for $a_{10} \ge 1$

$$K_2^{(1)} = \left\{ 0 \le x_2 \le \frac{a_8 a_{10}}{a_{12}} \right\}; \tag{3.17}$$

while for $a_{10} < 1$

$$K_2^{(1)} = \left\{ 0 \le x_2 \le \frac{a_8}{a_{12}} \right\}. \tag{3.18}$$

Cytokine TGF$-\beta$ dynamics F_β. To define a domain in which the dynamic of TGF$-\beta$ cytokine F_β is bounded, the locator function is applied $h_3 = x_3$. The following set is obtained:

$$S(h_3) = \{a_{13} + a_{14} x_1 - a_{15} x_3 = 0\};$$

From which the following formula is determined:

$$h_3 \mid_{S(h_3)} = \left(\frac{a_{13}}{a_{15}} + \frac{a_{14}}{a_{15}} a_2 \right); \tag{3.19}$$

which represents the constraint of the proposed locator function in the set $S(h_3)$. Applying the principle of extrema to obtain the location set:

$$K_3^{(1)} = \left\{ \frac{a_{13}}{a_{15}} \le x_3 \le \frac{a_{13}}{a_{15}} + \frac{a_{14}}{a_{15}} a_2 \right\}. \tag{3.20}$$

IFN$-\gamma$ dynamics F_γ. To define a domain in which the dynamic of IFN$-\gamma$ F_γ is bounded, the locator function is applied $h_4 = x_4$. The following set is obtained:

$$S(h_4) = \{a_{16} x_2 - a_{17} x_4 = 0\};$$

From which the following formula is determined:

$$h_4 \mid_{S(h_4)} = \left(\frac{a_{16} a_8}{a_{17} a_{12}} \right); \tag{3.21}$$

which represents the constraint of the proposed locator function in the set $S(h_4)$. Applying the principle of extrema to obtain the location set:

$$K_4^{(1)} = \left\{ 0 \leq x_4 \leq \frac{a_{16}a_8}{a_{17}a_{12}} \right\}. \tag{3.22}$$

MHC class I dynamics M_I. To define a domain in which the dynamics of MHC class I M_I is bounded, the locator function is applied $h_5 = x_5$. The following set is obtained:

$$S(h_5) = \left\{ a_{18} + \frac{a_{19}x_4}{x_4 + a_{20}} - a_{21}x_5 = 0 \right\};$$

From which the following formula is determined:

$$h_5 \mid_{S(h_5)} = \left(\frac{a_{18}}{a_{21}} + \frac{a_{19}}{a_{21}} \right); \tag{3.23}$$

which represents the constraint of the proposed locator function in the set $S(h_5)$. Applying the principle of extrema to obtain the location set:

$$K_5^{(1)} = \left\{ \frac{a_{18}}{a_{21}} \leq x_5 \leq \frac{a_{18}}{a_{21}} + \frac{a_{19}}{a_{21}} \right\}. \tag{3.24}$$

MHC class II dynamics M_{II}. To define a domain in which the dynamics of MHC class II M_{II} is bounded, the locator function is applied $h_6 = x_6$. The following set is obtained:

$$S(h_6) = \left\{ \left(\frac{a_{22}x_4}{x_4 + a_{23}} \right) \left(\frac{a_{24}(1 - a_{25})}{x_3 + a_{24}} + a_{25} \right) - a_{26}x_6 = 0 \right\};$$

From which the following formula is determined:

$$h_6 \mid_{S(h_6)} = \left(\frac{a_{22}a_{25}}{a_{26}} \right); \tag{3.25}$$

which represents the constraint of the proposed locator function in the set $S(h_6)$. From the above, it can be seen that there are two cases to consider: $a_{25} \geq 1$ and $a_{25} < 1$ respectively.

Applying the principle of extrema to obtain the location set in each case, one has for $a_{25} \geq 1$

$$a_{25} \geq 1 : K_6^{(1)} = \left\{ 0 \leq x_6 \leq \frac{a_{22}a_{25}}{a_{26}} \right\}; \tag{3.26}$$

while for $a_{25} < 1$

$$a_{25} < 1 : K_6^{(1)} = \left\{ 0 \leq x_6 \leq \frac{a_{22}}{a_{26}} \right\}; \tag{3.27}$$

then, the test is completed. ■

3.3.6 Iterations to refine the limits

By using the iterative theorem, it is possible to enhance the limits stated in Proposition 5.1.

Proposition 5.2. *All compact sets invariant in* $\mathbf{R}^4_{+,0}$ *are located in the bounded set* Π_2 *defined by* $\Pi_2 = \cap_{i=1}^4 K_i^{(2)}$ and

$$K_i^{(2)} = \left\{ x_{i\min}^{(2)} \le x_i^{(2)} \le x_{i\max}^{(2)} \right\};\ i = 1,2,3,4, \tag{3.28}$$

with

$$\begin{aligned} x_{i\max}^{(2)} &:= h_{i,\sup} = \max\left(h_i\,|_{S(h_i)\cap\Pi_1}\right); \\ x_{i\min}^{(2)} &:= h_{i,\inf} = \min\left(h_i\,|_{S(h_i)\cap\Pi_1}\right). \end{aligned}$$

Test. Employing the iterative theorem, we have:

Tumor cells dynamics T. To define a domain in which the Tumor cells T is bounded, the equation 3.14 is used to determine the maximum and minimum levels of x_1

$$\begin{aligned} h_{1,\sup} &= \max\left(h_1\,|_{S(h_1)\cap\left\{x_{1\min}^{(1)}\le x_1\right\}\cap\left\{x_2\le x_{2\max}^{(1)}\right\}\cap\left\{x_{3\min}^{(1)}\le x_3\right\}\cap\left\{x_5\le x_{5\max}^{(1)}\right\}}\right) = x_{1\max}^{(2)}; \\ x_{1\max}^{(2)} &:= a_1\left(1-\frac{x_{1\min}^{(1)}}{a_2}\right) - a_3\left(\frac{x_{5\max}^{(1)}}{x_{5\max}^{(1)}+a_4}\right)\left(a_5+\frac{a_6(1-a_5)}{x_{3\min}^{(1)}+a_6}\right)\left(\frac{x_{2\max}^{(1)}}{a_7+x_{1\min}^{(1)}}\right); \\ h_{1,\inf} &= \min\left(h_1\,|_{S(h_1)\cap\left\{x_1\le x_{1\max}^{(1)}\right\}\cap\left\{x_{2\min}^{(1)}\le x_2\right\}\cap\left\{x_3\le x_{3\max}^{(1)}\right\}\cap\left\{x_{5\min}^{(1)}\le x_5\right\}}\right) = x_{1\min}^{(2)}; \\ x_{1\min}^{(2)} &:= a_1\left(1-\frac{x_{1\max}^{(1)}}{a_2}\right) - a_3\left(\frac{x_{5\min}^{(1)}}{x_{5\min}^{(1)}+a_4}\right)\left(a_5+\frac{a_6(1-a_5)}{x_{3\max}^{(1)}+a_6}\right)\left(\frac{x_{2\min}^{(1)}}{a_7+x_{1\max}^{(1)}}\right). \end{aligned}$$

The location set is obtained:

$$K_1^{(2)} = \left\{ x_{1\min}^{(2)} \le x_1^{(2)} \le x_{1\max}^{(2)} \right\}. \tag{3.29}$$

CTL dynamics C: To define a domain in which the CTL cells C is bounded, the equation 3.16 is used, of which there are to cases to consider: $a_{10} \ge 1$ and $a_{10} < 1$ respectively.

When setting the maximum and minimum levels in x_2, it is available for $a_{10} \ge 1$

$$\begin{aligned} h_{2,\sup} &= \max\left(h_2\,|_{S(h_2)\cap\left\{x_1\le x_{1\max}^{(1)}\right\}\cap\left\{x_3\le x_{3\max}^{(1)}\right\}\cap\left\{x_6\le x_{6\max}^{(1)}\right\}}\right) = x_{2\max}^{(2)}; \\ x_{2\max}^{(2)} &:= \left(\frac{a_8 x_{6\max}^{(1)} x_{1\max}^{(1)}}{a_{12}x_{6\max}^{(1)}x_{1\max}^{(1)}+a_9}\right)\left(a_{10}+\frac{a_{11}(1-a_{10})}{x_{3\max}^{(1)}+a_{11}}\right); \\ h_{2,\inf} &= \min\left(h_2\,|_{S(h_2)\cap\left\{x_{1\min}^{(1)}\le x_1\right\}\cap\left\{x_{3\min}^{(1)}\le x_3\right\}\cap\left\{x_{6\min}^{(1)}\le x_6\right\}}\right) = x_{2\min}^{(2)}; \\ x_{2\min}^{(2)} &:= \left(\frac{a_8 x_{6\min}^{(1)} x_{1\min}^{(1)}}{a_{12}x_{6\min}^{(1)}x_{1\min}^{(1)}+a_9}\right)\left(a_{10}+\frac{a_{11}(1-a_{10})}{x_{3\min}^{(1)}+a_{11}}\right). \end{aligned}$$

while for $a_{10} < 1$

$$
\begin{aligned}
h_{2,\sup} &= \max\left(h_2\,|_{S(h_2)\cap\left\{x_1\le x_{1\max}^{(1)}\right\}\cap\left\{x_{3\min}^{(1)}\le x_3\right\}\cap\left\{x_6\le x_{6\max}^{(1)}\right\}}\right) = x_{2\max}^{(2)};\\
x_{2\max}^{(2)} &:= \left(\frac{a_8 x_{6\max}^{(1)} x_{1\max}^{(1)}}{a_{12} x_{6\max}^{(1)} x_{1\max}^{(1)} + a_9}\right)\left(a_{10} + \frac{a_{11}(1-a_{10})}{x_{3\min}^{(1)} + a_{11}}\right);\\
h_{2,\inf} &= \min\left(h_2\,|_{S(h_2)\cap\left\{x_{1\min}^{(1)}\le x_1\right\}\cap\left\{x_3\le x_{3\max}^{(1)}\right\}\cap\left\{x_{6\min}^{(1)}\le x_6\right\}}\right) = x_{2\min}^{(2)};\\
x_{2\min}^{(2)} &:= \left(\frac{a_8 x_{6\min}^{(1)} x_{1\min}^{(1)}}{a_{12} x_{6\min}^{(1)} x_{1\min}^{(1)} + a_9}\right)\left(a_{10} + \frac{a_{11}(1-a_{10})}{x_{3\max}^{(1)} + a_{11}}\right).
\end{aligned}
$$

Depending on the case, the location set is obtained:

$$
K_2^{(2)} = \left\{x_{2\min}^{(2)} \le x_2^{(2)} \le x_{2\max}^{(2)}\right\}. \tag{3.30}
$$

Cytokine TGF$-\beta$ dynamics F_β. To define a domain in which the dynamic of TGF$-\beta$ cytokine F_β is bounded, equation 3.19 is used and establishes the maximum and minimum levels of x_3

$$
\begin{aligned}
h_{3,\sup} &= \max\left(h_3\,|_{S(h_3)\cap\left\{x_1\le x_{1\max}^{(1)}\right\}}\right)\\
&= x_{3\max}^{(2)} := \frac{a_{13}}{a_{15}} + \frac{a_{14}}{a_{15}} x_{1\max}^{(1)};\\
h_{3,\inf} &= \min\left(h_3\,|_{S(h_3)\cap\left\{x_{1\min}^{(1)}\le x_1\right\}}\right)\\
&= x_{3\min}^{(2)} := \frac{a_{13}}{a_{15}} + \frac{a_{14}}{a_{15}} x_{1\min}^{(1)}.
\end{aligned}
$$

The location set is obtained:

$$
K_3^{(2)} = \left\{x_{3\min}^{(2)} \le x_3^{(2)} \le x_{3\max}^{(2)}\right\}. \tag{3.31}
$$

IFN$-\gamma$ dynamics F_γ. To define a domain in which the dynamic of IFN$-\gamma$ F_γ is bounded, equation 3.21 is used and establishes the maximum and minimum levels of x_4

$$
\begin{aligned}
h_{4,\sup} &= \max\left(h_4\,|_{S(h_4)\cap\left\{x_2\le x_{2\max}^{(1)}\right\}}\right)\\
&= x_{4\max}^{(2)} := \frac{a_{16}}{a_{17}} x_{2\max}^{(1)};\\
h_{4,\inf} &= \min\left(h_4\,|_{S(h_4)\cap\left\{x_{2\min}^{(1)}\le x_2\right\}}\right)\\
&= x_{4\min}^{(2)} := \frac{a_{16}}{a_{17}} x_{2\min}^{(1)}.
\end{aligned}
$$

The location set is obtained:

$$K_4^{(2)} = \left\{ x_{4\,\min}^{(2)} \le x_4^{(2)} \le x_{4\,\max}^{(2)} \right\}. \tag{3.32}$$

MHC class I dynamics M_I. To define a domain in which the dynamics of MHC class I M_I is bounded, equation 3.23 is considered and establishes the maximum and minimum levels of x_5

$$\begin{aligned} h_{5,\sup} &= \max\left(h_5 \mid_{S(h_5)\cap\left\{x_4 \le x_{4\,\max}^{(1)}\right\}} \right) \\ &= x_{5\,\max}^{(2)} := \frac{a_{18}}{a_{21}} + \frac{a_{19}}{a_{21}} \left(\frac{x_{4\,\max}^{(1)}}{x_{4\,\max}^{(1)} + a_{20}} \right); \\ h_{5,\inf} &= \min\left(h_5 \mid_{S(h_5)\cap\left\{x_{4\,\min}^{(1)} \le x_4\right\}} \right) \\ &= x_{5\,\min}^{(2)} := \frac{a_{18}}{a_{21}} + \frac{a_{19}}{a_{21}} \left(\frac{x_{4\,\min}^{(1)}}{x_{4\,\min}^{(1)} + a_{20}} \right). \end{aligned}$$

The location set is obtained:

$$K_5^{(2)} = \left\{ x_{5\,\min}^{(2)} \le x_5^{(2)} \le x_{5\,\max}^{(2)} \right\}. \tag{3.33}$$

MHC class II dynamics M_{II}. To define a domain in which the dynamics of MHC class II M_{II} is bounded, equation 3.25 is used, of which there are to cases to consider: $a_{25} \ge 1$ and $a_{25} < 1$ respectively.

When setting the maximum and minimum levels in x_6, it is available for $a_{25} \ge 1$

$$\begin{aligned} h_{6,\sup} &= \max\left(h_6 \mid_{S(h_6)\cap\left\{x_3 \le x_{3\,\max}^{(1)}\right\}\cap\left\{x_4 \le x_{4\,\max}^{(1)}\right\}} \right) = x_{6\,\max}^{(2)}; \\ x_{6\,\max}^{(2)} &:= \left(\frac{a_{22} x_{4\,\max}^{(1)}}{a_{26}(x_{4\,\max}^{(1)} + a_{23})} \right) \left(\frac{a_{24}(1-a_{25})}{x_{3\,\max}^{(1)} + a_{24}} + a_{25} \right); \\ h_{6,\inf} &= \min\left(h_6 \mid_{S(h_6)\cap\left\{x_{3\,\min}^{(1)} \le x_3\right\}\cap\left\{x_{4\,\min}^{(1)} \le x_4\right\}} \right) = x_{6\,\min}^{(2)}; \\ x_{6\,\min}^{(2)} &:= \left(\frac{a_{22} x_{4\,\min}^{(1)}}{a_{26}(x_{4\,\min}^{(1)} + a_{23})} \right) \left(\frac{a_{24}(1-a_{25})}{x_{3\,\min}^{(1)} + a_{24}} + a_{25} \right). \end{aligned}$$

while for $a_{25} < 1$

$$h_{6,\sup} = \max\left(h_6\,|_{S(h_6)\cap\left\{x_{3\min}^{(1)}\le x_3\right\}\cap\left\{x_4\le x_{4\max}^{(1)}\right\}}\right) = x_{6\max}^{(2)};$$
$$x_{6\max}^{(2)} := \left(\frac{a_{22}x_{4\max}^{(1)}}{a_{26}(x_{4\max}^{(1)}+a_{23})}\right)\left(\frac{a_{24}(1-a_{25})}{x_{3\min}^{(1)}+a_{24}}+a_{25}\right);$$
$$h_{6,\inf} = \min\left(h_6\,|_{S(h_6)\cap\left\{x_3\le x_{3\max}^{(1)}\right\}\cap\left\{x_{4\min}^{(1)}\le x_4\right\}}\right) = x_{6\min}^{(2)};$$
$$x_{6\min}^{(2)} := \left(\frac{a_{22}x_{4\min}^{(1)}}{a_{26}(x_{4\min}^{(1)}+a_{23})}\right)\left(\frac{a_{24}(1-a_{25})}{x_{3\max}^{(1)}+a_{24}}+a_{25}\right).$$

Depending on the case, the location set is obtained:

$$K_6^{(2)} = \left\{x_{6\min}^{(2)} \le x_6^{(2)} \le x_{6\max}^{(2)}\right\}. \tag{3.34}$$

3.3.7 Equilibrium points of the system

The equilibrium points of the system(3.13) are obtained by solving $\dot{x}_i = 0$ for $i = 1,\dots,6$.

Tumor dynamics x_1:

$$0 = a_1x_1\left(1-\frac{x_1}{a_2}\right) - a_3\left(\frac{x_5}{x_5+a_4}\right)\left(a_5+\frac{a_6(1-a_5)}{x_3+a_6}\right)\left(\frac{x_2x_1}{a_7+x_1}\right) \tag{3.35}$$

CTL dynamics x_2:

$$0 = \left(\frac{a_8x_6x_1}{x_6x_1+a_9}\right)\left(a_{10}+\frac{a_{11}(1-a_{10})}{x_3+a_{11}}\right) - a_{12}x_2 + S \tag{3.36}$$

Cytokine TGF–β dynamics x_3**:**

$$0 = a_{13}+a_{14}x_1-a_{15}x_3 \implies x_3 = \frac{a_{13}+a_{14}x_1}{a_{15}} \tag{3.37}$$

IFN–γ dynamics x_4**:**

$$0 = a_{16}x_2 - a_{17}x_4 \implies x_4 = \frac{a_{16}}{a_{17}}x_2 \tag{3.38}$$

MHC class I dynamics x_5

$$0 = a_{18}+\frac{a_{19}x_4}{x_4+a_{20}} - a_{21}x_5 \implies x_5 = \frac{a_{18}(x_4+a_{20})+a_{19}x_4}{a_{21}(x_4+a_{20})} \tag{3.39}$$

MHC class II dynamics x_6

$$0 = \left(\frac{a_{22}x_4}{x_4+a_{23}}\right)\left(\frac{a_{24}(1-a_{25})}{x_3+a_{24}}+a_{25}\right) - a_{26}x_6 \implies x_6 = \frac{a_{22}x_4}{a_{26}(x_4+a_{23})}\left(\frac{a_{24}(1-a_{25})}{x_3+a_{24}}+a_{25}\right) \tag{3.40}$$

Equations 3.37–3.40 admit explicit solutions in terms of x_1 and x_2:

- The cytokine concentration (x_3) depends linearly on the tumor population (x_1) (Equation 3.37).
- Inflammatory signals (x_4) are proportional to immune cells (x_2) (Equation 3.38).
- Inhibitors (x_5) and growth factors (x_6) respond nonlinearly to x_4 and x_3 (Equations 3.39, 3.40).

However, the coupled equations for x_1 and x_2 (Equations 3.35, 3.36) form a system that does not admit closed-form analytical solutions. Therefore, the equilibrium points were calculated numerically in MATLAB R2020b, in cases with cycle treatment, continuous treatment ($S = 3\times10^8$) and without treatment ($S = 0$) with clinically relevant parameters and initial conditions proposed in [2] and [3]. Table 3.8 shows the numerical results of the equilibrium states of the tumor-immune system in two clinical scenarios of grade III MG (early vs. advanced diagnosis), under a cyclical immunotherapy protocol with CTLs. Table 3.9 shows the numerical results of continuous CTL therapy administered to the tumor compared to the absence of treatment to validate the natural course of the disease. In the subsequent Results section 4, the equilibrium points will be shown visually with a biological perspective.

Table 3.8: Equilibrium Tumor-Immune dynamics under cyclic CTL therapy

Variable	Initial Condition (Early-diagnosed Grade III MG)	Treatment scheduling $S = (3\times(3\times10^8$ aCTL q5d)+45d of rest)×5
x_1 (Tumor)	1×10^{10}	0
x_2 (CTLs)	2.0×10^6	0
x_3 (F_β)	1.0	9.12×10^4
Variable	Initial Condition (Early-diagnosed Grade III MG)	Treatment scheduling $S = (3\times(3\times10^8$ aCTL q5d)+45d of rest)×5
x_1 (Tumor)	2.5×10^{10}	1.00×10^{11}
x_2 (CTLs)	2.0×10^6	8.64×10^4
x_3 (F_β)	1.0	9.14×10^3

Table 3.9: Equilibrium values under continuous treatment conditions

Variable	Initial Condition (Early-diagnosed Grade III MG)	$S = 0$	$S = 3\times10^8$
x_1 (Tumor)	1×10^{10}	1.00×10^{11}	0
x_2 (CTLs)	2.0×10^6	8.71×10^4	1.71×10^9
x_3 (F_β)	1.0	9.12×10^4	9.13×10^3
Variable	Initial Condition (Advanced MG Grade III)	$S = 0$	$S = 3\times10^8$
x_1 (Tumor)	2.5×10^{10}	1.00×10^{11}	0
x_2 (CTLs)	2.0×10^6	8.24×10^4	1.71×10^9
x_3 (F_β)	1.0	9.12×10^4	9.12×10^3

CHAPTER 4

Results

4.1 Results of Deep Learning technique for multiclass classification

As previously stated, the CNN models were trained via a 5-fold cross-validation method. The following Figures and Tables display the quantitative results derived from the data. This section evaluates the effectiveness of pre-trained TL classifiers used to categorize MRI images from the previously given multiclass dataset. TL classifiers and hyperparameter optimization significantly mitigate overfitting issues, often seen in deep learning algorithms when evaluated with a limited dataset.

Following the preprocessing work, the resulting picture examples are shown in the figure. Zoom and brightness properties were included into each image sample for every tumor type, including glioma and no-tumor, while the location was altered, as seen in the meningioma and pituitary cases. The primary objective of the used preprocessing techniques was to enable the models to discern various image attributes.

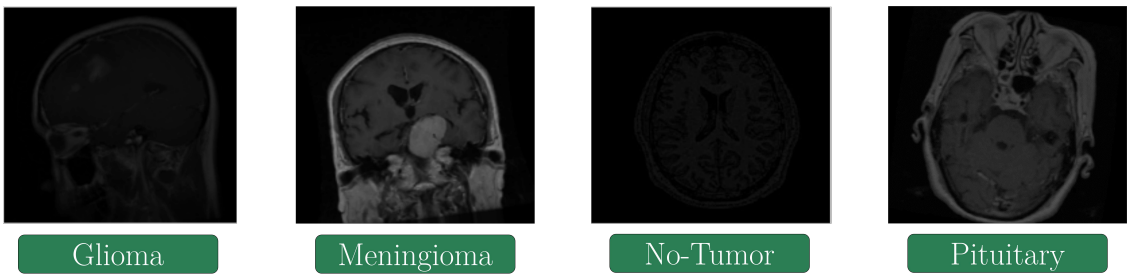

Figure 4.1: Instances of preprocessed images.

Table 4.1 presents the classification outcomes of the transfer learning methods and the suggested model, indicating that each transfer learning classifier yielded satisfactory and competitive results, taking into account the preprocessing used and the dataset composition utilized. The algorithms were assessed using the assessment metrics of Accuracy, Precision, Recall, Specificity, and Area Under the Curve (AUC). The loss ratio for each occurrence was noted, revealing that the InceptionV3 model achieved the lowest losses throughout the training phase. The DL InceptionV3 model had the greatest average accuracy of 97.12%, based on cross-validation conducted with $k = 5$. Conversely, it is crucial to note that the versions of ResNet, namely ResNet50 and InceptionResNetV2, yielded

distinct but very comparable outcomes, securing the second and third positions in the Table with 96.97% and 96.78%, respectively.

Table 4.1: Performance Metrics results.

Model	Accuracy	Precision	Recall	Specificity	AUC	Loss
InceptionV3	0.9712	0.9797	0.9659	0.9998	0.9984	0.0796
ResNet50	0.9697	0.9796	0.9637	0.9997	0.9982	0.0812
InceptionResNetV2	0.9678	0.9767	0.9623	0.9998	0.9980	0.0907
Xception	0.9567	0.9662	0.9509	0.9998	0.9972	0.1157
MobileNetV2	0.9545	0.9661	0.9473	0.9997	0.9967	0.1221
EfficientNetB0	0.9088	0.9312	0.8912	0.9997	0.9898	0.2347
Generic CNN	0.8108	0.8527	0.7677	0.9924	0.9616	0.4661

Table 4.2 provides a detailed account of the outcomes achieved in each K-Fold throughout the cross-validation procedure for the model with the highest average performance, InceptionV3. The standard deviation and confidence limit exhibit little variation throughout the K-Folds, indicating a favorable outcome as it reflects the proximity of the data to the median. This illustrates the robustness of the method to multiple data blocks.

Table 4.2: Performance Metrics results in K-Folds 1-5 of InceptionV3.

K-Fold	Accuracy	Precision	Recall	Specificity	AUC	Loss
1	0.9717	0.9788	0.9666	0.9998	0.9985	0.07778
2	0.9727	0.9818	0.9671	0.9999	0.9987	0.07591
3	0.9714	0.9801	0.9667	0.9998	0.9983	0.08086
4	0.9702	0.9788	0.9646	0.9998	0.9984	0.08082
5	0.9703	0.9791	0.9647	0.9999	0.9985	0.08284
Average	0.97126	0.9797	0.9659	0.9998	0.9984	0.0796
Std. Desv.	0.00093	0.00114	0.00106	0.00004	0.000132	0.00246
Conf. Limit	0.0008	0.001	0.0009	0.00004	0.0001	0.00216

Plots were created using Wandb. Wandb is a tool for monitoring machine learning projects. It facilitates machine learning practitioners in monitoring trials and disseminating their findings to collaborators [88]. The training and validation procedures for the optimal classification model in this work are shown in Figures 4.2 and 4.3. The shown metrics represent the mean training and validation accuracy, as well as the mean training and validation precision. The quantity of K-Folds used in this investigation is shown in the graphs. The mean percentages of Accuracy and Precision are 97.12% and 97.97%, respectively. Conversely, the mean validation Accuracy and Precision are 97.82% and 98.64%, respectively.

Figure 4.4 also shows the percentage of losses in each K-Fold during InceptionV3 model training and validation. This model saw an average of 7.9% loss during training and 6.3% loss during validation.

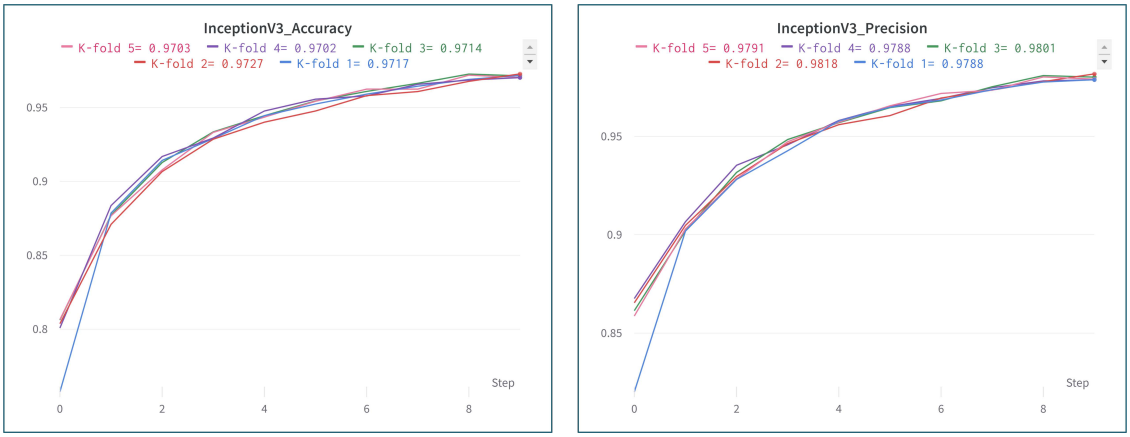

Figure 4.2: Training Accuracy and precision of the InceptionV3 model.

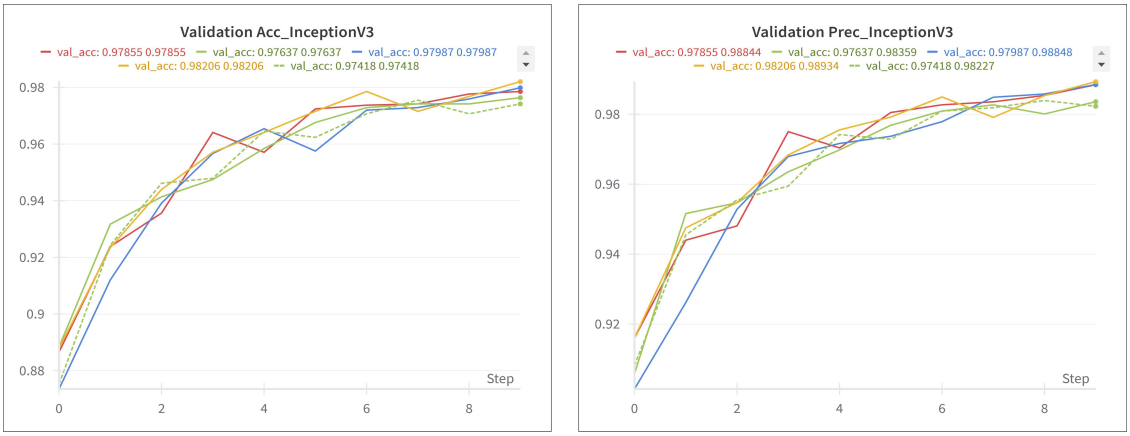

Figure 4.3: Validation Accuracy and precision of the InceptionV3 model.

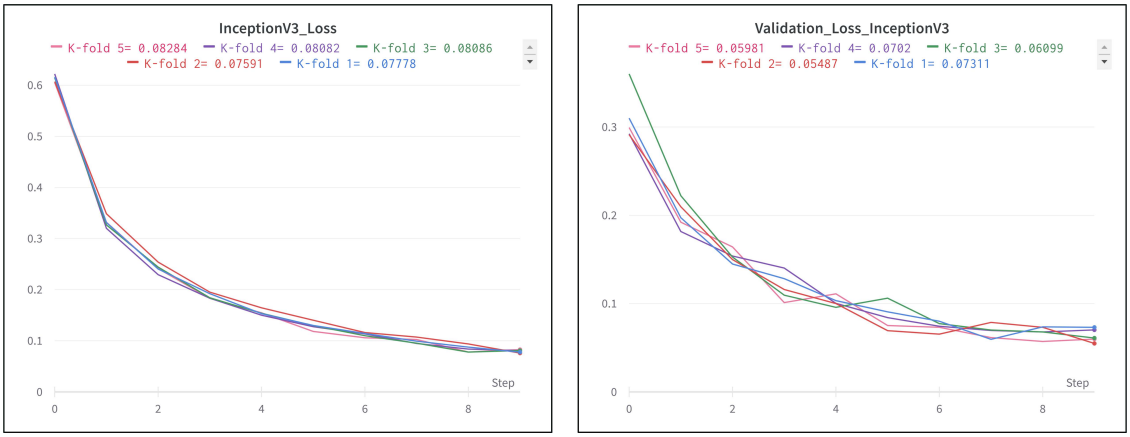

Figure 4.4: Training loss and validation loss of the InceptionV3 model.

Figure 4.5 shows the confusion matrices used to examine the particularities of each K-Fold in the Testing stage. Over-fitting caused by using 30% of the test data acquired during the data augmentation phase has resulted in misclassifications in each K-Fold of the confusion matrices. The confusion matrix of the InceptionV3 model for the first K-Fold in Figure 4.5(a) indicates 13 misclassified tumors categorized as 0 (Glioma), 12 as label 1 (Meningioma), 26 as 2 (No-tumor), and 4 as label 3 (Pituitary).

In the second K-Fold Figure 4.5(b) confusion matrix, there are 5 misclassified tumors from the Glioma label, 34 from the Meningioma label, 19 from the No-tumor label, and 1 from the Pituitary label. In a K-Fold of 3 Figure 4.5(c), 7 Gliomas, 16 Meningiomas, 12 No-tumor labels, and 1 Pituitary label are erroneously identified as tumors. In a K-Fold cross-validation with k equal to 4 in Figure 4.5(d), the misclassified tumors include 1 Glioma, 17 Meningiomas, 21 No-tumor labels, and 7 Pituitary labels. The ultimate K-Fold value is 5 in Figure 4.5(e), with misclassified classes including 5 Gliomas, 21 Meningiomas, 34 No-tumor labels, and 8 Pituitary labels. The InceptionV3 model exhibits more accuracy than its counterparts due to a reduced incidence of misclassified data.

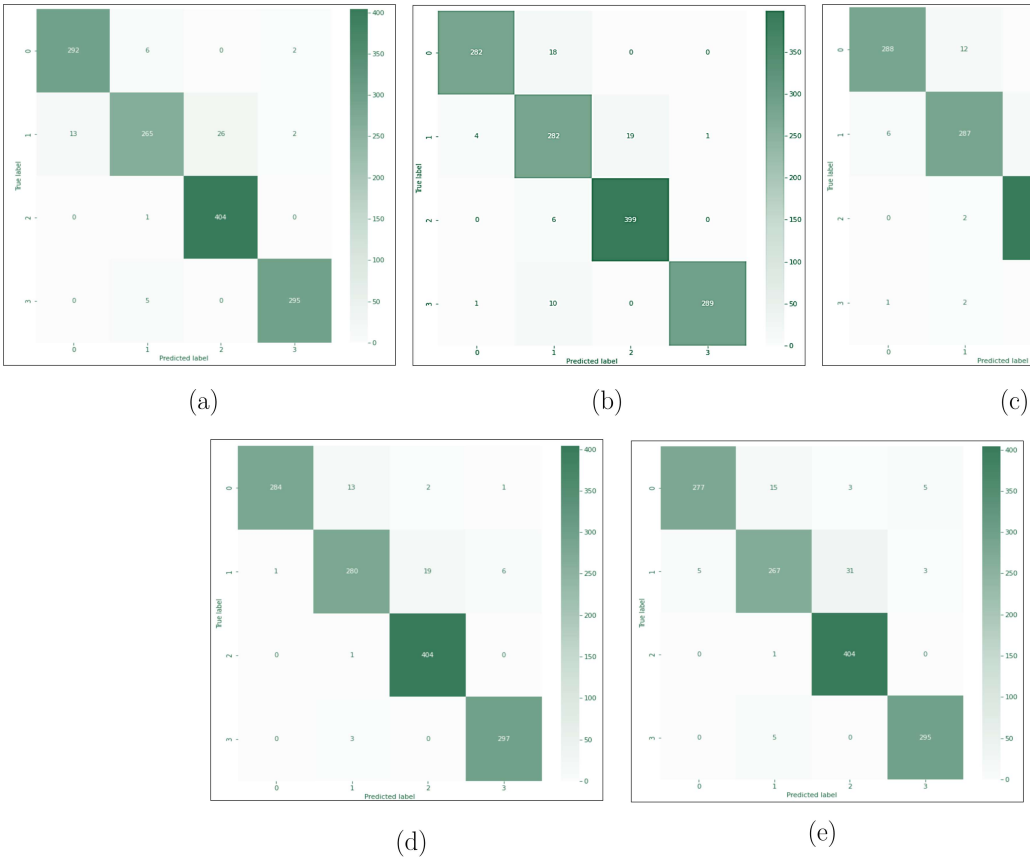

Figure 4.5: Confusion matrix in test stage of InceptionV3 model: (a) Confusion Matrix K-Fold = 1; (b) Confusion Matrix K-Fold = 2; (c) Confusion Matrix K-Fold = 3; (d) Confusion Matrix K-Fold = 4; (e) Confusion Matrix K-Fold = 5.

The following Table shows the performance metrics per K-Fold used in the testing stage. Also the average accuracy, precision, recall and F1 score.

Table 4.3: Performance test results in K-Folds 1-5 of InceptionV3.

K-Fold	Accuracy	Precision	Recall	F1-score
1	0.9600	0.9600	0.9600	0.9600
2	0.9500	0.9600	0.9500	0.9500
3	0.9700	0.9700	0.9700	0.9700
4	0.9600	0.9700	0.9600	0.9600
5	0.9500	0.9500	0.9400	0.9500
Average	0.9580	0.9620	0.9560	0.9580

The Model Size vs Model Accuracy graphic helped to choose the most efficient model in this investigation. This plot is in Figure 4.6. Since size impacts computational cost, this graphic is typically used to evaluate model performance. In [75], authors compared pre-trained and author-proposed models using this graph. The number of parameters or model size is on the x-axis and the accuracy % on the y-axis to create the graph. Graph structure is assessed to identify the best model parameters and accuracy.

InceptionV3 emerges as the most interesting model in this case study. Although ResNet50 ranked second in performance results, it has more parameters than InceptionV3, signifying a greater processing cost. Xception may be the second most effective model for this research because to its accuracy and restricted qualities.

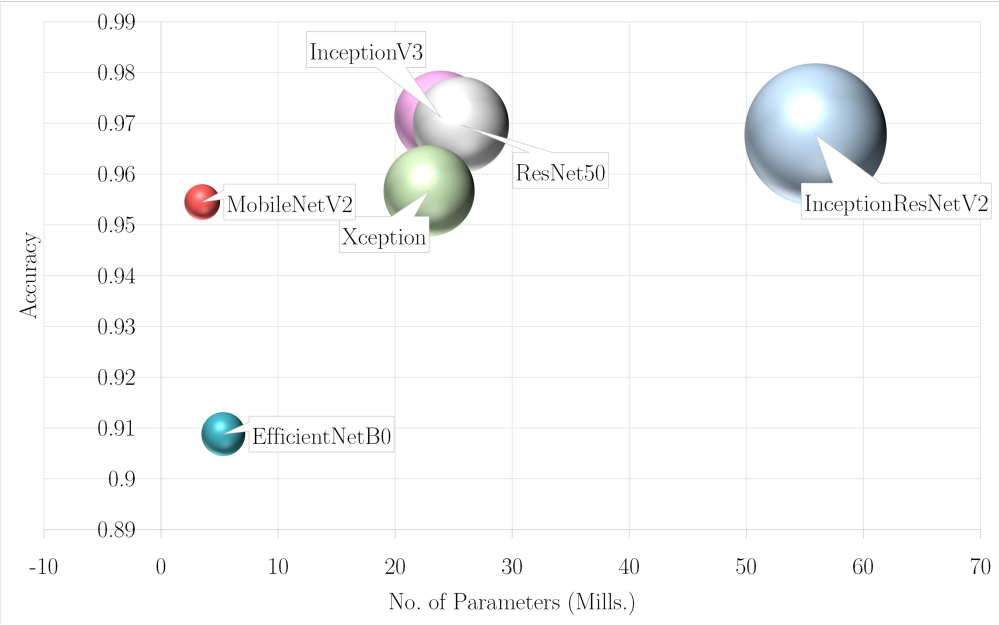

Figure 4.6: Model Size versus Model Accuracy. The amounts are shown in millions for each individual model.

4.1.1 Computational Complexity

This section examines the computational complexity required for this study. Table 4.4 has seven columns, beginning with the model name, followed by the accuracy and parameters of each model. The computational cost is shown as a percentage, starting with CPU and GPU utilization, followed by the percentage of allocated GPU memory, and finishing with the training duration because to its correlation with computational cost.

Table 4.4 indicates that the InceptionV3 model is distinguished from other high-accuracy models due to its reduced use of GPU and increased accuracy. The InceptionV3 model achieved an average GPU memory allocation of 60%. The results indicate that the runtime of this model has the most potential for improvement.

The computational cost graphs for all models examined in this work were created using WandB tool [88]. Figure 4.7 illustrates the proportion of CPU and GPU consumption during each training K-Fold for the InceptionV3 model. In each instance, the maximum usage value was recorded, and the average of these values was calculated, resulting in CPU and GPU utilization percentages of 73.7% and 58.73%, respectively, for InceptionV3, as shown in Table 4.4.

Table 4.4: Computational complexity of the models trained in this study.

Model	Accuracy	Parameters (Mills.)	%CPU	%GPU	%GPU Memory Allocated	Training Time (Minutes)
InceptionV3	0.9712	23.9	73.7	58.73	60	323
ResNet50	0.9697	25.6	71.36	78.53	66.83	223
InceptionResNetV2	0.9678	55.9	89.94	92.29	60.05	294
Xception	0.9567	22.9	75.36	98.4	66.83	274
MobileNetV2	0.9545	3.5	73.45	40.49	32.95	231
EfficientNetB0	0.9088	5.3	73.72	60.51	32.95	239

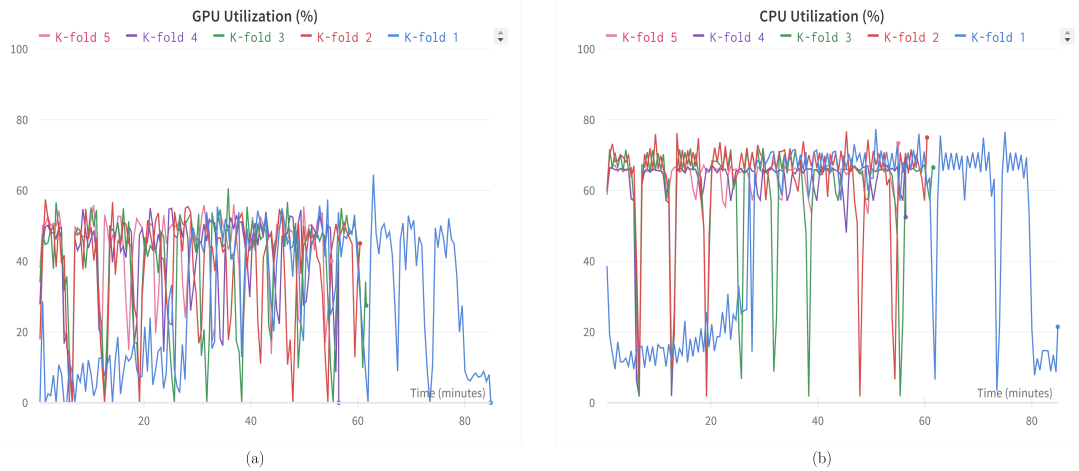

Figure 4.7: Computational resources used in InceptionV3 model: (a) GPU utilization percentage graph for InceptionV3 model; (b) CPU utilization percentage graph for InceptionV3 model.

Figure 4.8 additionally shows and demonstrates that 60% of GPU Memory was allocated while training K-Folds.

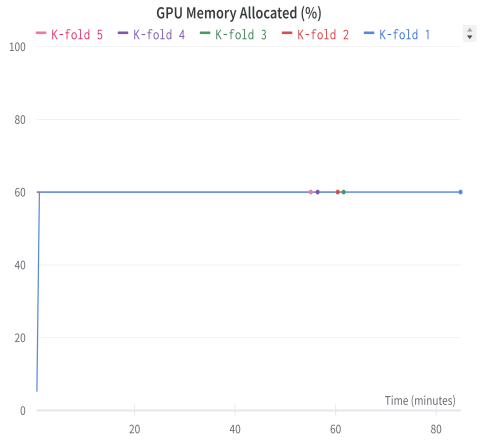

Figure 4.8: GPU Memory Allocated percentage graph for InceptionV3 model.

The Data Augmentation method significantly expanded the dataset, resulting in considerable processing time for all classification models. This duration is contingent upon the model's complexity and architectural design. The duration is quantified in hours and minutes. In the classification of brain tumors, TL's InceptionV3 model was the most time-consuming but the most successful classifier, achieving commendable classification results in a duration of 5 hours and 23 minutes. ResNet50 required a maximum of 3 hours and 43 minutes to identify and categorize MRI images of brain tumors into specific types. The TL model exhibited the fastest execution time and ranked second in the results Table. The MobileNetV2 model, owing to its design, had one of the quickest runtimes, yielding results in 3 hours and 51 minutes, with a reduced computational cost compared to the EfficientNetB0 model, which required 3 hours and 59 minutes. The classification time of the different ResNet transfer learning classifier versions escalates with the growth in the number of framework layers. For example, InceptionResNetV2 necessitated a minimum duration of 4 hours and 54 minutes. The duration of the Xception models was 4 hours and 34 minutes.

Additionally, the training duration of each CNN model was shown in Figure 4.9. Table indicates that, for the dataset used in this study, the accuracy increased somewhat when a shallower ResNet model was implemented. As the depth of the network increases, its computational cost and training duration also escalate, ultimately affecting the network's efficiency; this accounts for the variability in the accuracy of the ResNet variants. Furthermore, we may conclude that the inceptionV3 algorithm is the most effective method for classifying brain cancers in this research.

Figure 4.9: Training time in minutes of every model in this work.

4.2 Results of method for binary classification

Figure 4.10 illustrates all executions using the parameter optimization approach and the hyperparameters delineated in Table 3.5, with training loss designated as the main objective function and test accuracy as the secondary measure. The configuration outlined in Table 3.5 was repeatedly adjusted across the six potential architectures. Figure 4.11 presents results derived from using 50% of the dataset, with the starting learning rate set at 1×10^{-4}. Organizing the CNN models facilitates the visualization of trends, consequently improving the comparison of patterns across various models.

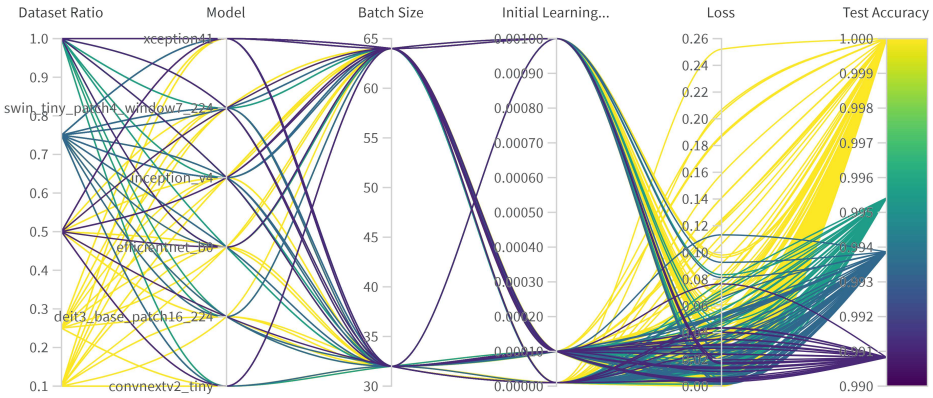

Figure 4.10: Differences in hyperparameters between all iterations are shown in the parallel graph. Minimizing training loss is of the highest priority when creating models, regardless of whether test accuracy is considered to be the benchmark for performance measurement.

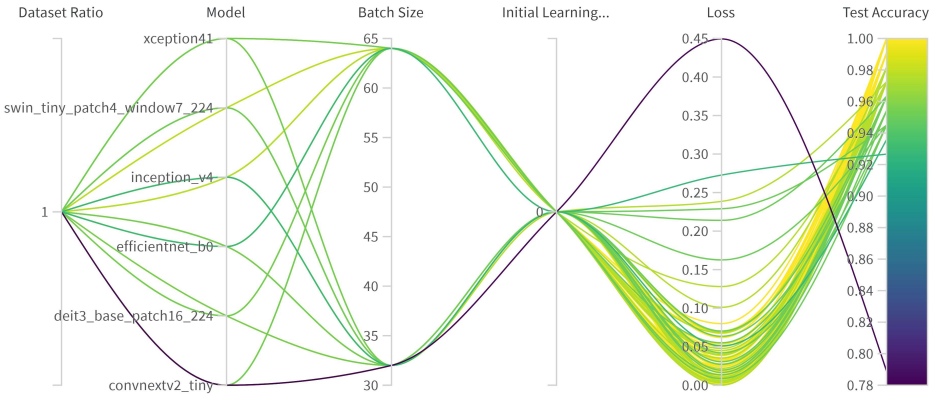

Figure 4.11: Using a dataset size of 50% and an initial learning rate of 1×10^{-4}, a parallel chart is used to illustrate the fluctuations in hyperparameters and filtering. During training, minimizing training loss is crucial, with test accuracy serving as an evaluation measure.

Training accuracy, training loss, and validation accuracy throughout the training stage are displayed in Figure 4.12.

Figure 4.12(a) illustrates the training accuracy of the models over the training steps. The y-axis represents accuracy values ranging from 0 to 1, while the x-axis denotes the training steps (0 to 50). All models show an increasing trend in accuracy. Inception_v4 achieves the highest training accuracy among all models, reaching close to 99% by the 50th training step. The model shows a consistent and steep increase in accuracy, indicating effective learning and optimization during training. EfficientNet_b0 also performs well but lags slightly behind Inception_v4, while other models like ConvNextV2_tiny and Xception41 show slower convergence. In Figure 4.12(b) the loss values decrease over time, indicating that the models are learning effectively. Models like ConvNextV2_tiny and Xception41 exhibit a steeper decline in loss compared to others. ConvNextV2_tiny demonstrates the lowest training loss, dropping to approximately 0 by the 50th training step. The model exhibits a sharp decline in loss early in training, suggesting rapid convergence and efficient optimization. Xception41 also performs well but has a slightly higher final loss while Inception_v4 and EfficientNet_b0 show slower reduction in loss. Finally, in Figure 4.12(c) The validation accuracy increases steadily for most models. DeiT3_base_patch16_224 achieves the highest validation accuracy, reaching close to 100% by the 50th training step. The model shows a steady increase in validation accuracy, indicating strong generalization capabilities. Swin_tiny_patch4_window7_224 also performs well but slightly underperforms compared to deiT3_base_patch16_224. Models like inception_v4 and efficientNet_b0 show slower improvement in validation accuracy. The findings indicate that inception_v4 has superior training accuracy, convNextV2_tiny is the most effective at reducing loss, and deiT3_base_patch16_224 exhibits optimal generalization on validation data.

The scikit-learn package supplies the metrics used to evaluate the performance of the different architectures. These include recall, accuracy, precision, F1 score, and Matthews Correlation Coefficient. The various DNNs' performance is evaluated using 219 test instances.

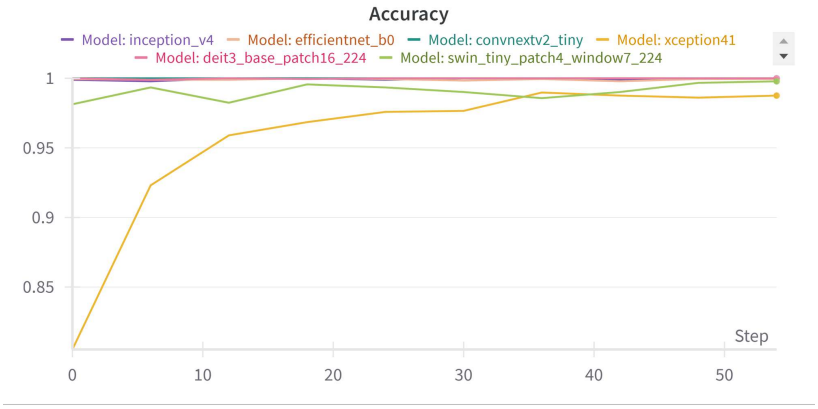

(a)

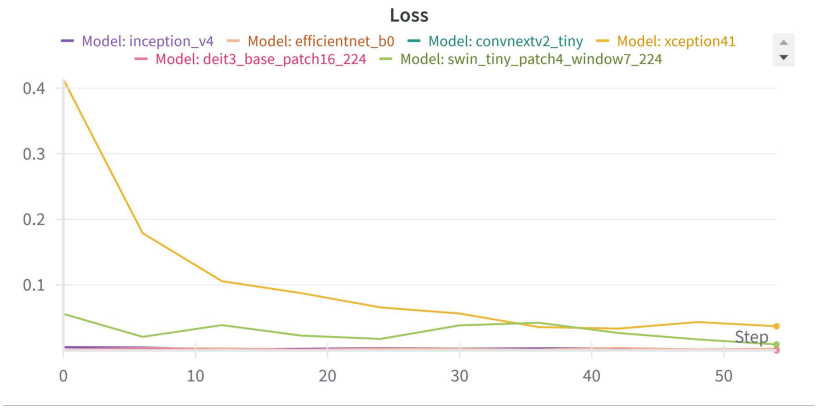

(b)

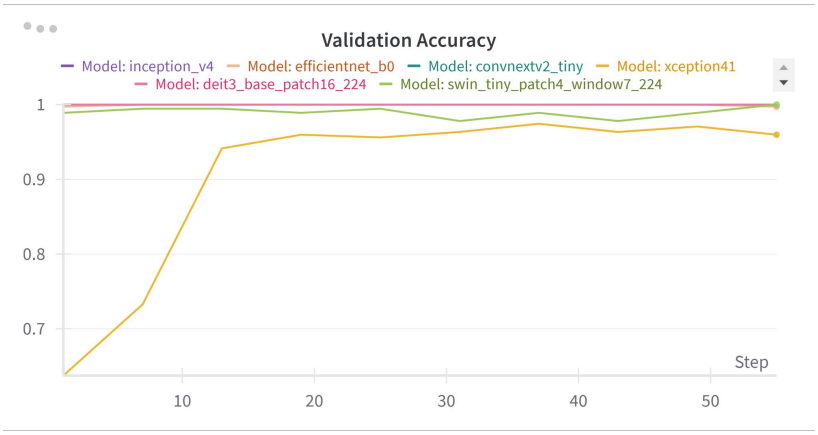

(c)

Figure 4.12: Accuracy, training loss, and validation accuracy during the final training run. (a) Training accuracy, (b) training loss, and (c) validation accuracy.

A correlation between the number of parameters in each model and the Test Accuracy metric, under the conditions of an initial learning rate 1×10^{-4}, a batch size of 64, and a dataset size of 50%, is presented as a bubble plot in Figure 4.13.

Swin_tiny_patch4_window7_224 having a moderate model size 28.1 million parameters, achieves the best test accuracy with 0.9959, demonstrating its efficiency in balancing complexity and performance. Similarly, deiT3_base_patch16_224 has the largest number of parameters 86.1 millions, yet its accuracy is 0.9908. Inception_v4 achieves competitive test accuracy 0.9898 with a moderate parameter count of 42.7 million parameters, making it a strong candidate for tasks requiring a balance between size and performance.

Xception41 maintains an impressive degree of test accuracy of 0.9857 with a second-smallest model size of 22.9 million parameters, proving its effectiveness in parameter utilization.

In scenarios of resource limited availability, EfficientNet_b0 is the most efficient model due to its minimal parameter count of 5.3 million parameters. It exemplifies the trade-off between size and performance, but in this case it obtained one of the lowest test accuracy in this work with 0.9766.

Despite having a similar parameter count to Swin_tiny_patch4_window7_224, 28.6 million parameters, convNextV2_tiny achieves the lowest test accuracy 0.9755. For this study, convnextV2_tiny is presenting potential inefficiencies in its architecture or training process.

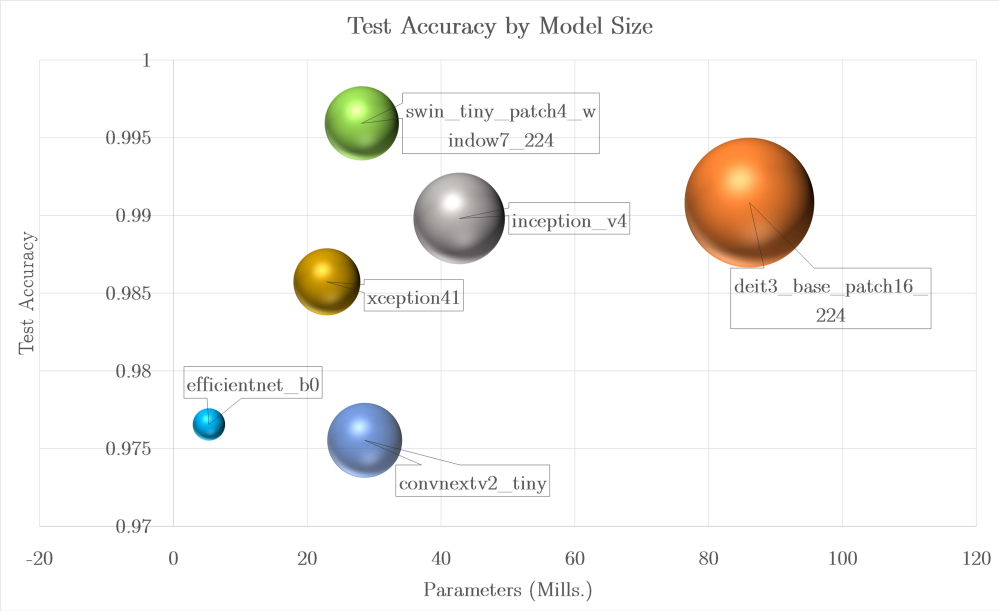

Figure 4.13: Test Accuracy in relation to the number of parameters for each tested architecture.

The presented Table 4.5 shows the performance metrics Test Accuracy, Test Precision, Test Recall, Test F1 Score, and Test MCC for CNN models swin_tiny_patch4_window7_224, deit3_base_patch16_224, inception_v4, xception41, efficientnet_b0, and convnextv2_tiny, evaluated under a set of specific conditions: learning rate 1×10^{-4}, a batch size of 64, and a dataset size of 50% used for training.

Swin_tiny_patch4_window7_224 model attains the greatest scores across all measures, making it the optimal model. The Test Accuracy is 0.9959, Test Precision is 0.9964, Test Recall is 0.9964, Test F1 Score is 0.9963, and Test MCC is 0.9918. This model has exceptional precision and recall,

indicating a robust capacity to accurately detect positive cases while reducing false positives and false negatives. Its elevated F1 score and Matthews correlation coefficient further validate its balanced and reliable performance.

Deit3_base_patch16_224 model ranks as the second-best performer, with somewhat lower scores than the leading model. The model attains a Test Accuracy of 0.9908, Test Precision of 0.9937, Test Recall of 0.9872, Test F1 Score of 0.9904, and Test MCC of 0.9818. This model achieves an ideal equilibrium between precision and recall, making it a strong competitor, despite its parameter count shown in Figure 4.13 signifying a substantial computational cost. Inception_v4 model achieves a third-place ranking, with a Test Accuracy of 0.9898, Test Precision of 0.9919, Test Recall of 0.9879, Test F1 Score of 0.9898, and Test MCC of 0.9797. Although its performance measures are somewhat inferior to the leading two models, it nonetheless exhibits a commendable equilibrium between precision and recall.

Xception41 model exhibits a significant decline in performance relative to the leading three models. The model attains a Test Accuracy of 0.9857, Test Precision of 0.9920, Test Recall of 0.9801, Test F1 Score of 0.9859, and Test MCC of 0.9717. Its diminished recollection signifies a greater difficulty in recognizing actual positives. The efficientnet_b0 model has the lowest accuracy, with Test Accuracy 0.9766, precision 0.9724, Recall 0.9822, F1 Score 0.9771, and MCC 0.9537. Despite its great recall, it may create more false positives. Finally, the convnextv2_tiny model has the lowest recall, with 0.9755 Test Accuracy, 0.9939 Test Precision, 0.9548 Test Recall, 0.9735 Test F1 Score, and 0.9521 Test MCC. Low recall reduces its effectiveness despite its outstanding precision.

Table 4.5: Comparison of models based on Test Accuracy and other metrics. Specific conditions: learning rate 1×10^{-4}, a batch size of 64, and a dataset size of 50% used for training.

Model	Test Accuracy	Test Presicion	Test Recall	Test F1 Score	Test MCC
swin_tiny_patch4_window7_224	0.9959	0.9964	0.9964	0.9963	0.9918
deit3_base_patch16_224	0.9908	0.9937	0.9872	0.9904	0.9818
inception_v4	0.9898	0.9919	0.9879	0.9898	0.9797
xception41	0.9857	0.9920	0.9801	0.9859	0.9717
efficientnet_b0	0.9766	0.9724	0.9822	0.9771	0.9537
convnextv2_tiny	0.9755	0.9939	0.9548	0.9735	0.9521

4.2.1 ML-Model Explorer

As suggested in [80, 89],the ML-Model Explorer tool was implemented in this study. This tool allows users to compare and choose multi-class classifiers by examining their confusion matrices, primarily addressing class imbalances. Results are displayed in Figure 4.14. Based on the analysis, deit3_base_patch16_224 and inception_v4 have the highest rank, both achieving a "Good" performance as indicated by the green color and their bars reaching the maximum value of 1. Efficientnet_b0, swin_tiny_patch4_window7_224, and xception41 are ranked in the "Medium" category (yellow bars). Their performance is slightly lower but still notable. Convnextv2_tiny appears to be the weakest model, as indicated by the "Weak" (red) performance category.

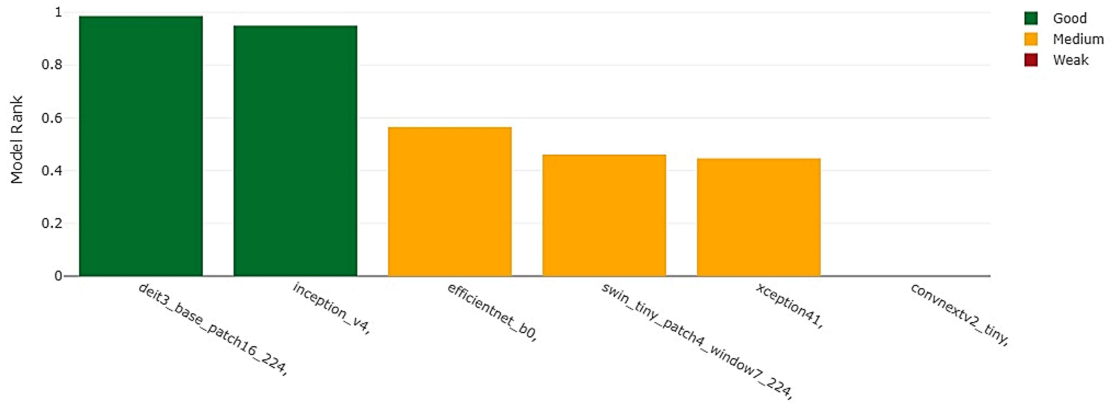

Figure 4.14: Rankings of models produced via the ML-Model Explorer tool.

The scatter plot in Figure 4.15 depicts the performance of the six DL models, evaluated based on their test accuracy and the standard deviation of test recalls. The x-axis represents the standard deviation of test recalls, where lower values signify greater consistency across K-Folds, while the y-axis represents test accuracy, with higher values indicating better classification performance.

The swin_tiny_patch4_window7_224 model achieves the highest test accuracy at 0.9959, making it the best performer in terms of classification. However, it has a standard deviation of 0.0103, indicating slightly less consistent recall performance across K-Folds. The second-best model, deit3_base_patch16_224, achieves an accuracy of 0.9908 with a standard deviation of 0.0181, reflecting a balance between accuracy and consistency.

With test accuracies of 0.9766 and 0.9898, respectively, other models, such as efficientnet_b0 and inception_v4, demonstrated slight levels of accuracy. Their greater standard deviations, which are 0.0353 and 0.0119 respectively, indicate that their recall ability is less consistent, particularly for efficientnet_b0. Similar to the previous example, xception41 has a standard deviation of 0.005, which is considered to be acceptable, but it achieves a test accuracy of 0.9857, which is less than ideal. With a standard deviation of 0.0324, the convnextv2_tiny model exhibits unpredictability in recalls. Furthermore, its accuracy of 0.9755 is the lowest among all models, which makes it less competitive than comparable models.

In summary, the swin_tiny_patch4_window7_224 model is the best performer due to its highest test accuracy of 0.9959. This combination of exceptional accuracy with acceptable variability makes it the most effective model for the given task. In second place, deit3_base_patch16_224 is recognized for its elevated test accuracy and little variability, while in third place, inception_v4 is acknowledged for its high test accuracy and similarly low variability.

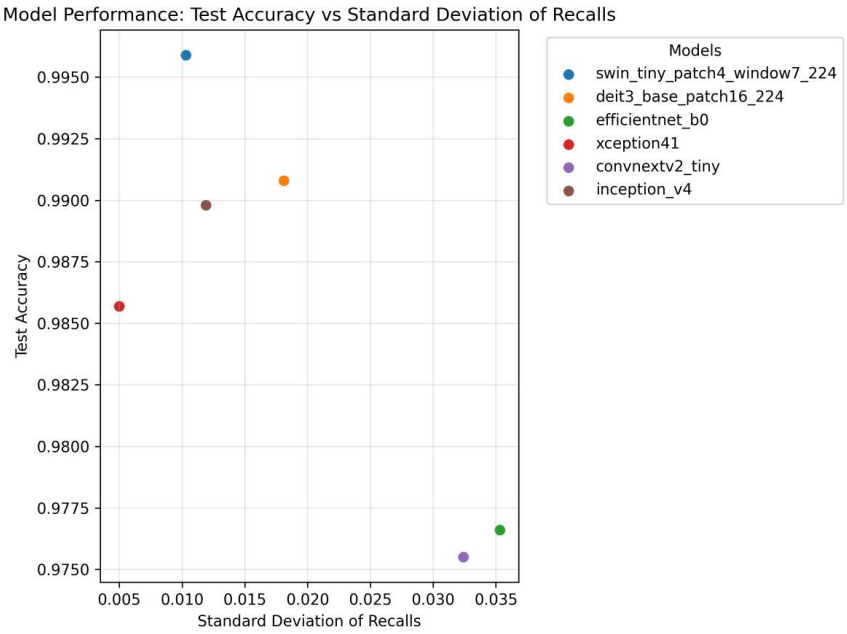

Figure 4.15: Standard deviation of recalls in DL models in relation to test accuracy.

Figure 4.16 presents a boxplot depicting the distribution of three critical metrics: F1-Score, Precision, and Recall. The parameters were a learning rate of 1×10^{-4}, a batch size of 64, and a dataset size of 100% used at this stage.

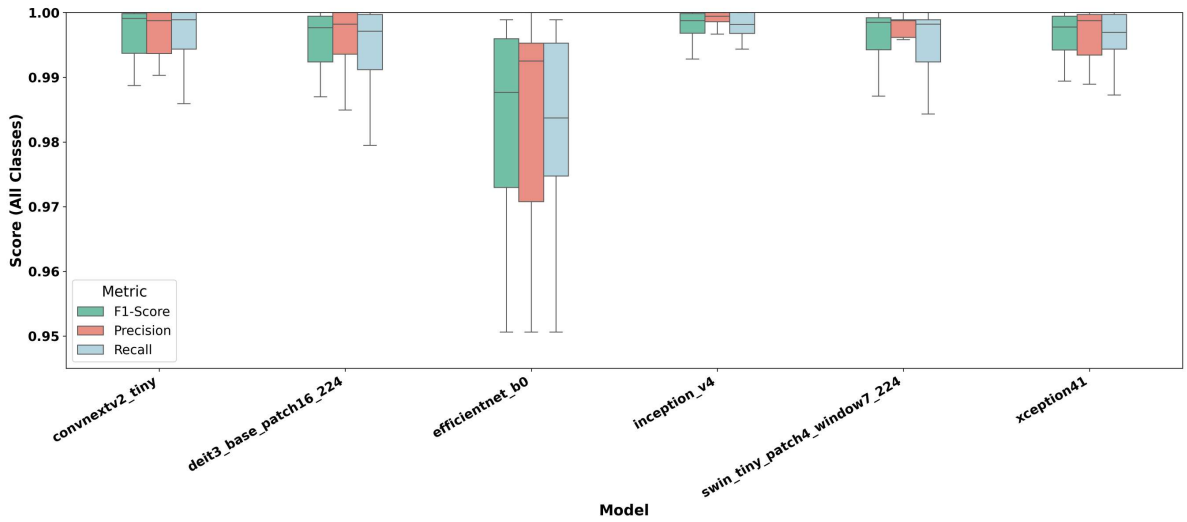

Figure 4.16: The box plot displays the statistical information of the CNN model-specific F1-Score, Precision, and Recall during training stage with learning rate of 1×10^{-4}, a batch size of 64, and a dataset size of 100%.

The x-axis denotes the models: convnextv2_tiny, deit3_base_patch16_224, efficientnet_b0, inception_v4, swin_tiny_patch4_window7_224, and xception41. The y-axis displays scores rang-

ing from 0.95 to 1.00. The measurements are denoted by distinct colors: green for F1-Score, red for Precision, and blue for Recall.

Convnextv2_tiny and deit3_base_patch16_224 provide near-perfect scores approaching 1.00 across all measures, exhibiting low fluctuation. These models exhibit robust and consistent performance. Efficientnet_b0 has more fluctuation and achieves significantly lower scores, ranging from 0.98 to 0.99. Nonetheless, it continues to be competitive regarding F1-Score and Recall. With its very small boxes and whiskers, inception_v4 distinguishes out for having the lowest variability, indicating consistent performance.

Swin_tiny_patch4_window7_224 has modest fluctuation while consistently achieving high scores, equivalent to EfficientNet_b0. Xception41 has exceptional Precision and Recall metrics, nearing 1.00, with little fluctuation; yet, its F1-Score may be somewhat inferior to those of convnextv2_tiny and deit3_base_patch16_224.

The box plot indicates that the optimal models are convnextv2_tiny and deit3_base_patch16_224, owing to their almost flawless scores and consistency. Inception_v4 provides very constant performance, making it a great selection where minimal variability is crucial. Xception41 has outstanding performance in Precision and Recall, yet it may exhibit a minor imbalance in its F1-Score.

4.2.2 DNN training runtime and computational complexity

In Figure 4.17(a) GPU utilization (%) over time (in seconds) is displayed. Each line represents a model's GPU usage. Inception_v4 (purple) shows low and erratic GPU utilization, frequently dropping close to 0% and peaking below 60%. Swin_tiny_patch4_Window7_224 (green) displays fluctuating usage between 20% and 80%, with inconsistent peaks and valleys. Deit3_base_patch16_224 (pink) exhibits the most consistent and high GPU utilization, maintaining values near or above 40-100% for most of the runtime. Efficientnet_b0 (orange) shows very irregular usage, oscillating between 0% and 40%. Xception41 (yellow) demonstrates moderate but steady utilization, averaging around 40-60%. Convnextv2_tiny (blue) also has erratic usage but reaches the highest peaks, frequently hitting 80% GPU utilization.

Figure 4.17(b) evaluates CPU utilization (%) over time (in seconds). All models exhibit consistent and relatively low CPU utilization. Inception_v4 (purple) stays steady around 35-40%. Swin_tiny_patch4_window7_224 (green) consistently operates around 30%. Deit3_base_patch16_224 (pink) maintains a stable utilization of 30%, the highest utilization over time among all models. Efficientnet_b0 (orange) operates at a consistent ~38% CPU usage. Xception41 (yellow) remains consistent around ~35%. Convnextv2_tiny (blue) has slightly lower CPU utilization, around 30%.

Considering resource efficiency, Swin_tiny_patch4_window7_224 is the best model due to its low hardware usage. Xception41 ranks second for its balance of stability and moderate resource demands. Deit3_base_patch16_224 may not be the optimal selection, since it utilizes more GPU and CPU resources in comparison to other models.

Figure 4.18(a) shows GPU Memory Allocated (%) over time. All models exhibit steady memory usage without fluctuation. Deit3_base_patch16_224 (pink) uses around 30% of GPU memory continuously. Convnextv2_tiny (blue) and xception41 (yellow) preserve 35% and 38%, respectively. Swin_tiny_patch4_window7_224 (green) and inception_v4 (purple) allocate about 20% of memory allocated. Memory consumption average is ~20% for efficientnet_b0 (orange). This steady allocation shows effective memory management by all models.

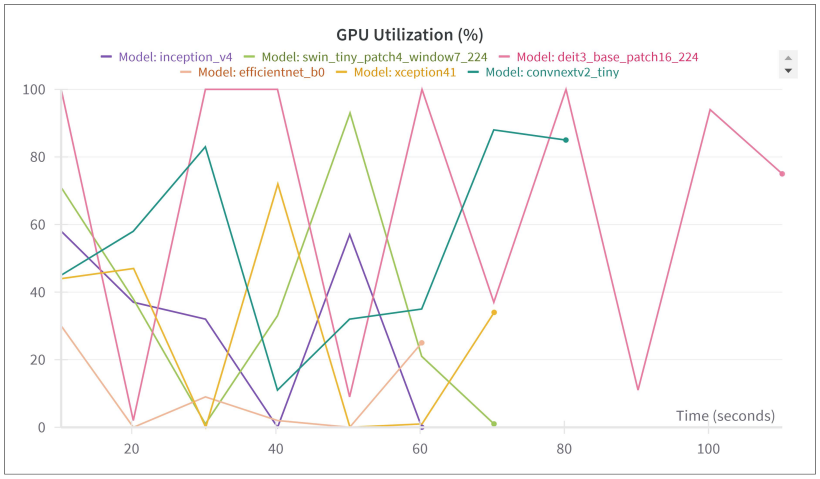

(a)

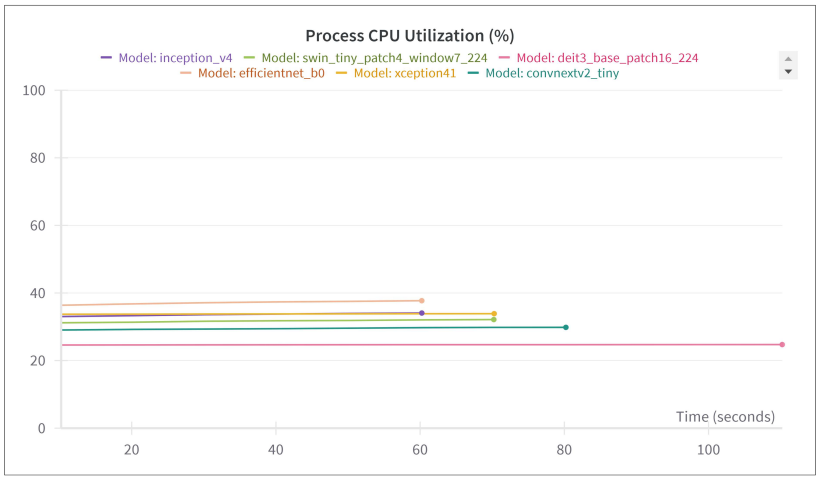

(b)

Figure 4.17: Resources used during the training process. (a) GPU usage throughout training, (b) CPU usage during the training phase.

Figure 4.18(b) shows GPU Power Usage (W) over time. Power consumption is largest and most constant in Deit3_base_patch16_224 (pink), reaching over 300W. Swin_tiny_patch4_window7_224 (green) varies between 150W and 250W, indicating moderate power demands. Convnextv2_tiny (blue) has peak power use at 300W but lowers to ~100W during idle times, indicating inefficiency. Power consumption for efficientnet_b0 (orange) is generally under 150W. Power consumption is seldom above ~100W for Xception41 (yellow). Inception_v4 (purple) uses the least power, running below 100W almost always, however this may reduce computing performance.

Swin_tiny_patch4_window7_224 matches modest GPU memory allocation (~20%) with consistent power utilization (~150W to 250W), ideal for high-performance and energy-efficient situations. Low GPU memory utilization (~20%) and low power needs (~150W) make efficientnet_b0 particularly efficient in resource-constrained settings. For works prioritizing energy efficiency, Xception41 is an efficient option with low GPU memory allocation 38% and low power usage (~100W).

Deit3_base_patch16_224 has the maximum performance potential because to its high GPU

memory utilization and power consumption, but it is unsuitable for resource-efficient applications.

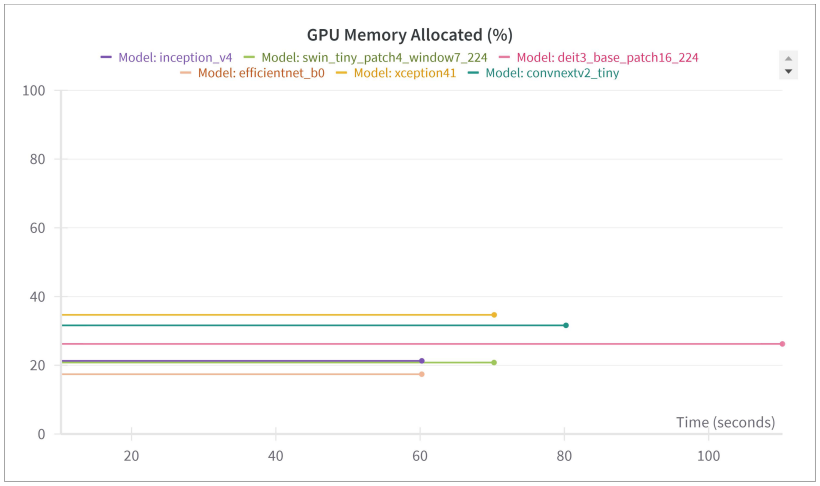

(a)

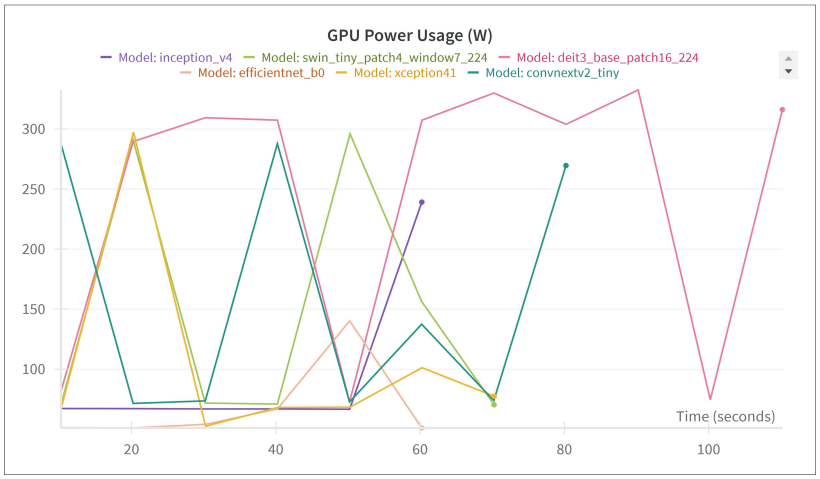

(b)

Figure 4.18: Resources used during the training process. (a) GPU memory allocation observed during the training phase, (b) Power Consumption of GPU throughout the training procedure.

4.2.3 Grad-CAM

Grad-CAM (Gradient-weighted Class Activation Mapping) is a prevalent visualization method in deep learning for interpreting and comprehending the choices of convolutional neural networks (CNNs). It emphasizes the areas in the input picture that most influence the network's predictions by using the gradients that propagate into the final convolutional layers. This approach is especially advantageous in medical imaging, such as brain tumor classification, where pinpointing the most relevant regions for the model's choice elucidates its reasoning process, hence enhancing interpretability and reliability.

The Figure 4.19 illustrates Grad-CAM outcomes applied to DL models trained for the classification of Low-Grade Gliomas (LGG) in this study. Each subfigure depicts the Grad-CAM heatmap

overlaid on a brain MRI image, with warmer hues (red, yellow and blue) signifying regions of greater significance for the model's prediction.

Figure 4.19(a) presents the GradCAM visualization for the inception_v4 model. The heatmap reveals dispersed attention across the MRI, with some concentration on key regions but also significant activation in nonrelevant areas. This suggests inadequate localization of LGG-related features, as the model partially focuses on the tumor while erroneously highlighting extraneous regions.

Figure 4.19(b) illustrates the Grad-CAM results for xception41. The model exhibits a focused emphasis on the approximate location of the tumor, with minimal activation outside the relevant area. This indicates superior feature localization compared to inception_v4, with the activated regions closely corresponding to the actual tumor site.

In Figure 4.19(c), the heatmap indicates a moderate localization of the tumor, although some attention is directed towards peripheral areas. While the interpretability surpasses that of inception_v4, it remains less concentrated than in xception41. The activated regions correspond to the tumor area but with lower precision.

Figure 4.19(d) displays the Grad-CAM visualization for swin_tiny_patch4_window7_224. The heatmap demonstrates a well-localized focus on the LGG region, with minimal noise in irrelevant areas. The activated areas align accurately with the tumor, suggesting that the model effectively identifies tumor-specific features, making it a strong candidate for accurate classification.

In Figure 4.19(e), corresponding to efficientnet_b0, a sharply focused heatmap is observed, with precise attention centered on the core of the tumor. The activated areas exhibit excellent correspondence with the tumor region, representing one of the most effective and interpretable visualizations among the evaluated models.

Finally, 4.19(f) shows the Grad-CAM visualization for deit3_base_patch16_224. Although there is considerable attention directed towards the tumor, there is also extensive activation across irrelevant regions. While the tumor is partially identified, the dispersion of attention reduces the overall clarity and interpretability of the model's decision-making process compared to the other architectures.

Among the evaluated models, EfficientNet_b0 demonstrates the highest performance in terms of tumor localization and interpretability, as evidenced by its sharply focused heatmap and precise attention on the tumor's core region. swin_tiny_patch4_window7_224 also exhibits strong performance, with a well-localized activation on the tumor and minimal noise in extraneous areas, indicating reliable feature identification. Xception41 ranks closely behind, achieving a focused emphasis on the tumor's approximate location with limited dispersion, although its localization is slightly less concentrated compared to EfficientNet_b0 and swin_tiny_patch4_window7_224. Overall, these three architectures show superior capabilities in accurately identifying tumor regions, making them strong candidates for applications requiring high interpretability and diagnostic precision.

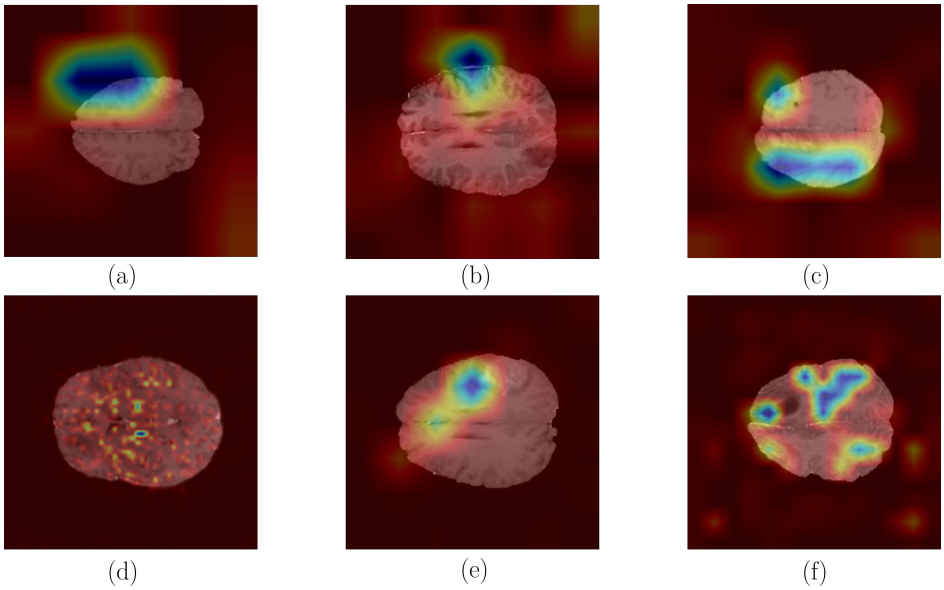

Figure 4.19: Results of the Grad-CAM approach applied to the trained deep learning models for the LGG class: (a) Inception v4, (b) Xception41, (c) Convnextv2 tiny, (d) Swin tiny patch4 window7 224, (e) Efficientnet b0, (f) Deit3 base patch16 224.

4.3 Results of Compact Invariant Sets Localization Method

The subsequent results include temporal simulations of treatment cycles, in addition to simulations assuming continuous treatment, and phase diagrams for both treatment scenarios—cyclic and continuous—demonstrating the equilibrium points achieved by the system in each instance. The findings of the iterative approach demonstrate the compact invariant sets at several identified equilibrium locations. These elements will allow for a detailed analysis of the dynamics of the system and the effectiveness of the treatment over time. The results are divided in two sections, tumors with early detection and advanced tumors. The studies in [2,3] provides a description of the model, cytotoxic T lymphocytes (CTLs) treatments, parameters, simulation timeframes, and other characteristics.

4.3.1 Results of therapy in tumors with early detection

Figure 4.20 illustrates the temporal changes in tumor cell population (T), CTLs, and transforming growth factor-beta (TGF-β) levels during a successful cancer treatment. The x-axis represents time in hours, ranging from 0 to 9000 hours, while the y-axis indicates the quantity of each component. As indicated in the numerical scale, the therapy time is 365 days, equivalent to 8760 hours. The tumor cell population is initially high, with a peak at 10^{10} cells. Over time, the number of tumor cells decreases significantly, reaching near-zero levels by 9000 hours. This reduction indicates the effectiveness of the treatment in eradicating tumor cells. CTLs, which play a crucial role in immune-mediated tumor cell destruction, show an initial increase in population peacking at 4.3×10^8 cells . CTLs remain increased during therapy, indicating tumor-fighting immunity. The CTL population decreases as the tumor cell number decreases. CTLs may have decreased due to decreasing tumor

load-induced antigenic stimulation. When there is a lack of substantial tumor cells to attack, the immune system diminishes the CTL response, resulting in a progressive reduction in their quantity. Over time, TGF-β levels decrease at 9.135×10^3, reaching lower levels by 9000 hours. This reduction may reflect the diminishing tumor burden and the associated decrease in immunosuppressive signals.

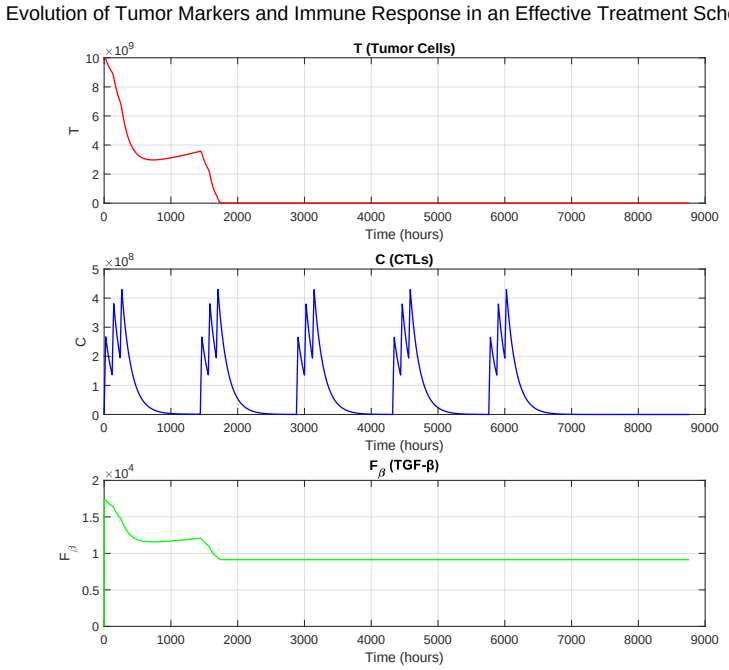

Figure 4.20: Anticipated eradication of early-diagnosed Grade III MG by aCTL immunotherapy. Initial conditions: $T(0) = 10^{10}$, $C(0) = 2 \times 10^6$. Scheduling of CTL immunotherapy: $(3 \times (3 \times 10^8$ aCTL q5d)+45d of rest) $\times 5$. Key parameter values used were mentioned in [2].

Figure 4.21 illustrates the results of an effective treatment of a high dose therapy of CTLs. The population of tumor cells starts at a high initial value, close to $T(0) = 10^{10}$. Nevertheless, it rapidly diminishes during the initial few hundred hours, nearing zero and maintaining that state for the rest of the simulation. This behavior suggests that the therapeutic intervention with the immunotherapy schedule displayed in Figure 4.21 effectively eradicates the tumor cells, preventing regrowth over time. The CTL population exhibits an oscillatory pattern, with periodic peaks followed by sharp declines. These oscillations likely correspond to waves of immune activation and contraction, where CTLs proliferate in response to tumor presence and subsequently decline once the tumor burden is reduced. The periodicity suggests a dynamic immune response cycle that continues despite the tumor being eliminated early in the simulation. In the absence of persistent tumor antigens, CTLs undergo apoptosis (programmed cell death) or transition into a quiescent state, causing their numbers to drop close to zero. This is a natural regulatory mechanism of the immune system to prevent excessive immune activity and autoimmunity.

The concentration of transforming growth factor $TGF-\beta$ begins at a heightened initial value and swiftly stabilizes at a reduced level 9.13×10^3. This stabilization indicates a control mechanism whereby $TGF-\beta$ attains a steady-state concentration. The sustained but diminished presence of $TGF-\beta$, an immunosuppressive cytokine, may signify ongoing immune modulation despite the

eradication of the tumor.

The results demonstrate effective tumor elimination, marked by a fast reduction in tumor cell numbers and sustained oscillatory immune response. The occurrence of periodic CTL peaks indicates a persistent but regulated immunological response, perhaps modulated by the actions of $TGF-\beta$. These results indicate that the immune system stays engaged and alert, inhibiting tumor recurrence while preserving homeostasis in the immune-regulatory network.

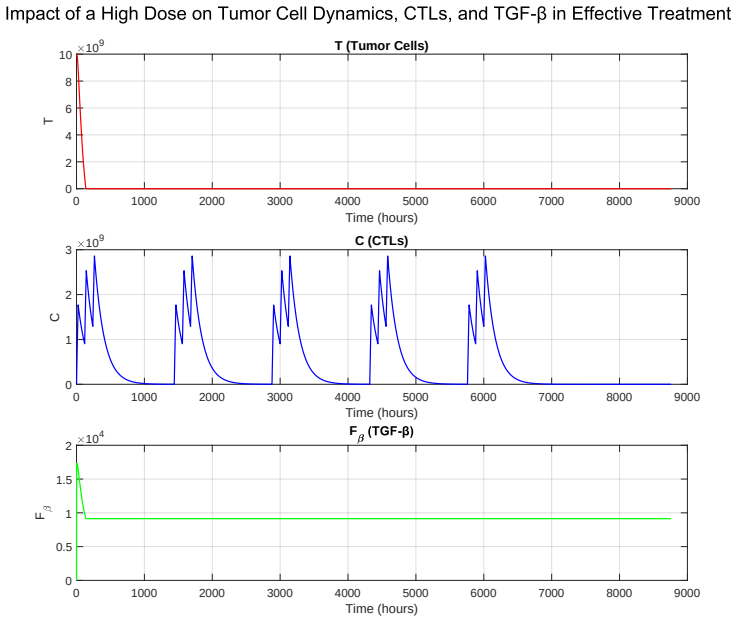

Figure 4.21: Expected elimination of early-stage Grade III MG by a high dosage of aCTL immunotherapy with initial tumor dimensions $T(0) = 10^{10}$, $C(0) = 2 \times 10^6$. CTL immunotherapy schedule: $(3 \times (3 \times 2 \times 10^9$ aCTL q5d)+45d of rest) $\times 5$. Key parameter values used were mentioned in [2].

In Figure 4.22 displays the temporal evolution of the model of early-diagnosed Grade III MG under continuous therapy $S = 3 \times 10^8$. Initial conditions are $T(0) = 10^{10}$, $C(0) = 2 \times 10^6$, $F_\beta(0) = 1$.

The tumor cell population T (red) starts at a high initial value but rapidly decreases to approximately zero. This behavior suggests effective tumor eradication, where the applied treatment successfully reduces tumor growth to an insignificant level.

The population of CTLs C (green) initially increases and then stabilizes at a constant value of 1.71×10^9. This indicates a sustained immune response, in which CTLs remain active at a constant level due to the infusion of a constant dose of therapy, preventing tumor recurrence.

The concentration of F_β (blue) shows a sharp initial decrease before stabilizing at a value of 9.135×10^3. This suggests that the system reaches a balance in the regulatory dynamics of TGF-β, maintaining an environment that neither excessively suppresses nor overstimulates the immune response.

These results highlight the stability achieved under continuous therapy, where the tumor is eradicated, immune cells persist at a controlled level, and immune-regulatory factors reach equilibrium.

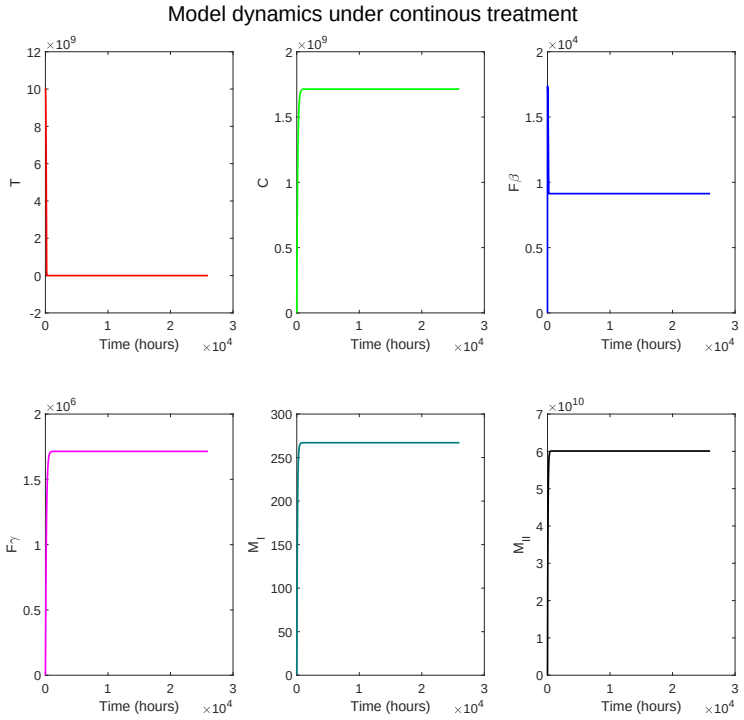

Figure 4.22: Tumor dynamics under continuous therapy, with initial conditions $T(0) = 10^{10}, C(0) = 2 \times 10^6, F_\beta(0) = 1$ and convergence to equilibrium in $T \approx 0, C \approx 1.71 \times 10^9, F_\beta \approx 9135$

Figures 4.23(a) and 4.23(b) illustrate two three-dimensional phase-space trajectories that depict the dynamics of a tumor-immune interaction model. They depict previous instances shown in Figures 4.20 and 4.22, corresponding to cycle therapy and continuous therapy, respectively.

Figure 4.23(a) depicts a trajectory (black line), it initiates from the initial condition (green diamond) and progresses toward a stable equilibrium point (red circle) where $T \approx 0$, $C \approx 20$, and $F_\beta \approx 9.14 \times 10^3$. This dynamic illustrates a scenario in which the tumor has been eradicated and the numbers of endogenous CTLs have normalized, indicating that the immune system is balanced and further therapy is unnecessary. The observed pattern aligns with a tendency towards a stable asymptotic dynamic, representing a tumor-free steady-state solution. The contour around the trajectory is a polytope of eleven iterations of the iterative localization method, which, from a mathematical perspective, ensures that the solution remains inside a positively invariant region of the phase space. This polytope represents a diminutive variant of the system's ultimate attractor, which constrains the viable trajectories of the model in the presence of therapy.

Figure 4.23(b), on the contrary, illustrates a distinctly different dynamic, where continuous treatment results in sustained proliferation of CTLs. In this scenario, the trajectory begins from the same initial conditions (green rhombus) and concludes at an equilibrium state where $T \approx 0$, $C \approx 1.71 \times 10^9$, and $F_\beta \approx 9.14 \times 10^3$. The tumor is prevented from recurring over time due to the significant and continuous immunological pressure exerted by the regular administration of CTLs. In this instance, CTLs do not return to baseline levels as shown in the left. Instead, they remain elevated, indicating that the immune system is perpetually functioning. This dynamic indicates the existence of system attractors, with the configuration of the external stimulus (the treatment) dictating which

attractor is activated. Both trajectories technically mean convergence toward fixed points, while from a medical standpoint they denote two modes of monitoring: autonomous functional immunity due to periodic treatment doses (left) and therapeutically enhanced immunity with continuous, uninterrupted therapy (right). Both cases illustrate the importance of treatment design for the future of the system, particularly with regard to tumor eradication.

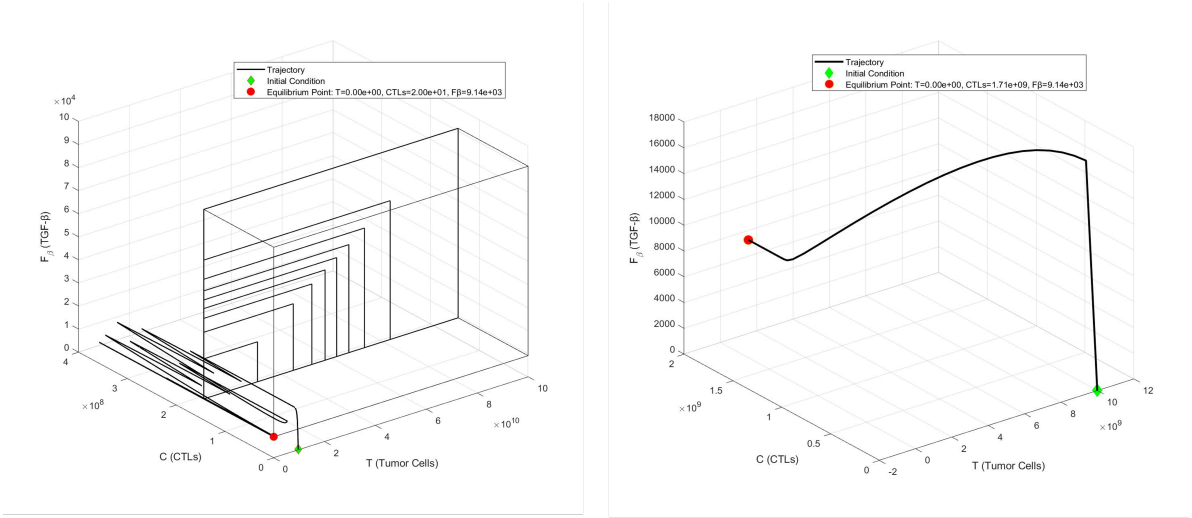

(a) (b)

Figure 4.23: Phase space trajectories of the tumor and immune system under different CTL treatment plans and defined by initial conditions $T(0) = 10^{10}$, $C(0) = 2 \times 10^6$, $F_\beta = 1$. Scheduling of CTL immunotherapy: $(3 \times (3 \times 10^8$ aCTL q5d)+45d of rest) $\times 5$. a) Trajectory under pulsed immunotherapy schedule, showing tumor eradication and convergence to a tumor-free equilibrium. The final state is enclosed by an 11-iteration polytope approximating the global attractor. b) Trajectory under continuous CTL administration, highlighting an alternative equilibrium with persistent CTLs and tumor suppression.

4.3.2 Results of therapy in advanced tumors

This section displays simulations of advanced malignant neoplasm that do not receive the appropriate amount of therapy. The dosage is administered in cycles and other case is displayed without therapy. The simulations were performed over a time span of three years (approximately 26,280 hours).

Figure 4.24 illustrates the temporal changes in T and CTLs during an unsuccessful cancer treatment over a period of 40 months, scaled in hours. The x-axis represents time in hours, while the y-axis indicates the quantity of each component, scaled appropriately for clarity. The tumor cell population starts at 2.5×10^{10} cells and shows a steady increase over time, reaching up 3×10^{10} cells at the end of the treatment stage. This continued growth during the rest of the 40-month period indicates that treatment is not effective in controlling or reducing the tumor burden. The lack of reduction in the tumor cell population suggests that the tumor continues to proliferate without significant hindrance.

The population of CTLs, which are crucial for immune mediated tumor cell killing, remains relatively low and stable throughout the treatment period. The count of CTLs fluctuates slightly,

but does not show a significant increase, reaching a maximum of about 2.5×10^8 and 4×10^8 cells. The absence of significant CTL activity indicates an insufficient immunological response to the tumor. The failure of CTLs to proliferate and efficiently target tumor cells is a critical component in therapy ineffectiveness.

Levels of $TGF-\beta$, a cytokine that can suppress the immune response and promote tumor progression, remain elevated throughout much of the treatment period. The presence of $TGF-\beta$ at significant levels of 9.12×10^4 cells suggests an immunosuppressive tumor microenvironment. This may partially explain the decreased activity of CTLs, since $TGF-\beta$ suppresses immune cell function and promotes immunological evasion by the tumor.

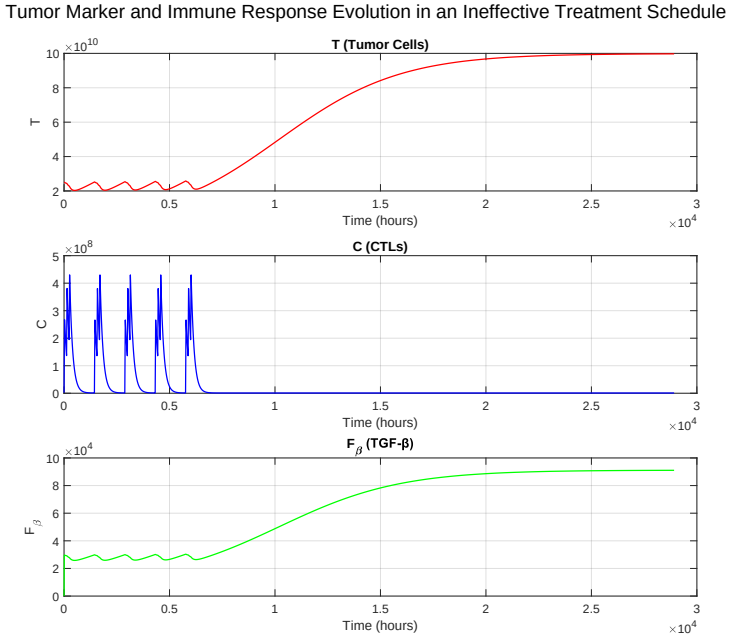

Figure 4.24: Ineffective treatment of advanced-stage grade III MG with aCTL immunotherapy due to elevated initial tumor dimensions $T(0) = 2.5 \times 10^{10}$, $C(0) = 2 \times 10^6$, $F\beta = 1$. CTL immunotherapy schedule: $(3 \times (3 \times 10^8$ aCTL q5d)+45d of rest) $\times 5$. Key parameter values used were mentioned in [2].

As indicated in Figure 4.25 in the absence of therapy ($S = 0$) the temporal evolution of the key variables T (tumor cells), C (CTL), and F_β (TGF-β) has a markedly different dynamic, yet maintains a steady state comparable to a scenario of ineffective therapy, resulting in tumor growth rather than elimination.

The tumor cell population T (red) exhibits uncontrolled growth, increasing from its initial value and stabilizing at approximately 10^{11}. This indicates that, without treatment, tumor cells proliferate rapidly and reach a high equilibrium level.

The CTL population C (green) initially starts at 2×10^6 but quickly declines to a lower equilibrium value of 8.71×10^4, which will eventually become a smaller value. This suggests a weakened immune response, likely due to tumor-induced immunosuppression, leading to an insufficient attack on cancer cells.

The concentration of F_β (blue) increases over time and stabilizes at 9.12×10^4. This reflects a strong immunosuppressive environment, where high levels of TGF-β hinder the effectiveness of the immune system, allowing tumor cells to thrive.

These results highlight the detrimental effects of untreated tumor growth, where immune suppression dominates, CTLs fail to control the tumor, and cancer progression becomes inevitable.

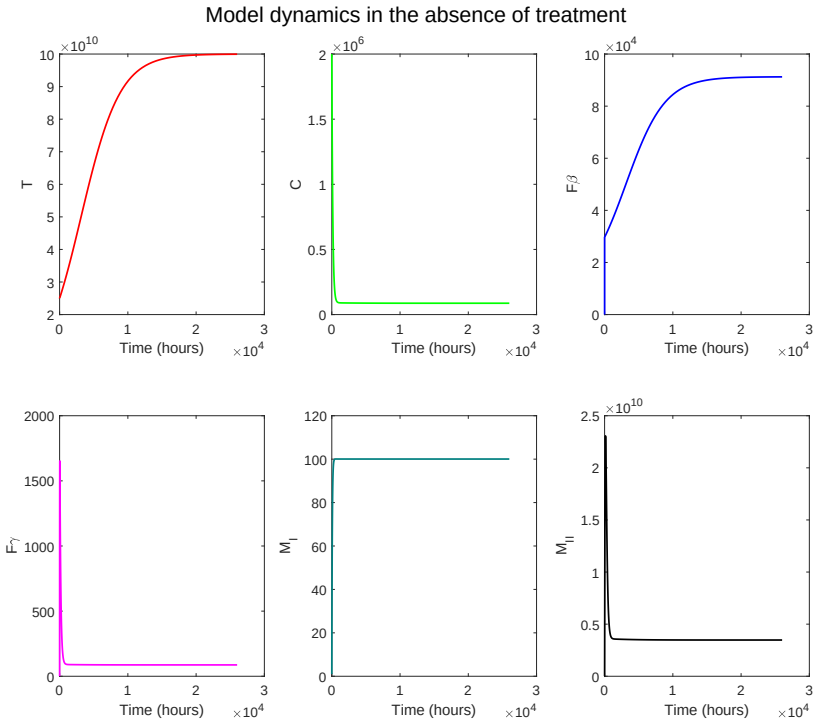

Figure 4.25: Tumor dynamics without therapy, with initial conditions of an advanced tumor $T(0) = 2.5\times10^{10}, C(0) = 2\times10^6, F_\beta(0) = 1$ and equilibrium point at: $T = 10^{11}, C = 8.71\times10^4, F_\beta = 9.12\times10^4$.

Figure 4.26 depicts evolution of an advanced-stage grade III MG within a three-dimensional phase space, characterized by the variables: T, CTLs, and the immunosuppressive factor $F\beta$, under two distinct situations. Initial conditions of the advanced tumor are $T(0) = 10^{10}$, $C(0) = 2 \times 10^6$, $F_\beta = 1$ and $T(0) = 2.5 \times 10^{10}$, $C(0) = 2 \times 10^6$, $F_\beta = 1$. CTL immunotherapy dosage is: $(3 \times (3 \times 10^8$ aCTL q5d)+45d of rest) $\times 5$.

Figure 4.26(a) illustrates the progression of the system following cyclic immunotherapy treatment. Despite the administration of treatment, the tumor continues to proliferate, resulting in a state of equilibrium (indicated in red) characterized by a substantial tumor burden ($T \approx 9.95\times10^{10}$), diminished levels of CTLs ($C \approx 8.64 \times 10^4$), and elevated expression of the factor F_β ($\approx 9.08 \times 10^4$). This dynamic indicates that the therapy was ineffective in managing the disease. Figure 4.26(b) illustrates the progression of the system in the absence of therapy, analogous to the autonomous growth of cancer. Similarly, the system progresses towards an equilibrium position nearly identical to that depicted in Figure 4.26(a). Furthermore, a polytope is incorporated that delineates the feasible solutions of the system and aids in visualizing how the dynamics are restricted inside a phase space area indicative of tumor development and the absence of efficient immune modulation.

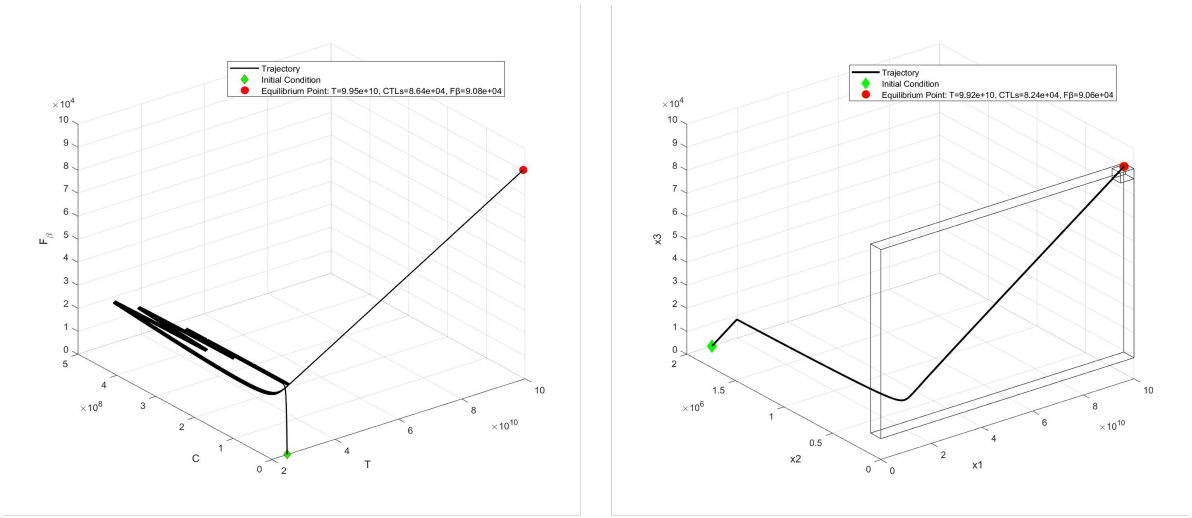

(a) (b)

Figure 4.26: Evolution of the immune-tumor system under ineffective immunotherapy ($3 \times (3 \times 10^8$ aCTL q5d)+45d of rest) ×5, initial conditions $T(0) = 2.5 \times 10^{10}$, $C(0) = 2 \times 10^6$, $F_\beta = 1$ and without treatment. a) System trajectory under an ineffective cyclical immunotherapy treatment. b) Tumor proliferation in the absence of immunotherapy treatment.

Finally, in Figure 4.27, analysis of advanced tumor evolution over time in phase space, both with and without therapeutic intervention is depicted. The image displays two distinct trajectories originating from a same initial condition, shown as a green diamond with coordinates $T = 2.5 \times 10^{10}$, $C = 2.0 \times 10^6$, $F_\beta = 1$ indicating an advanced malignancy grade III.

The black trajectory illustrates the temporal evolution of the system under treatment ($S = 3 \times 10^8$). The system attains an equilibrium state in which the tumor is eradicated ($T \approx 0$), characterized by elevated concentrations of CTLs ($C = 1.71 \times 10^9$, and moderate levels of TGF-β $F_\beta = 9.14 \times 10^3$). A red point indicates this equilibrium. It is a stable attractor that represents immune-mediated tumor control in a mathematical point of view.

The blue trajectory illustrates the system's typical changes in the absence of treatment ($S = 0$). The pathway culminates in a pathological equilibrium state, shown as a pink sphere. This condition has a significant tumor burden ($T = 9.99 \times 10^{10}$), diminished immune response ($C = 8.24 \times 10^4$), and elevated TGF-β levels ($F_\beta = 9.12 \times 10^4$). This trajectory illustrates the diminishing stability of immune-tumor interactions in the absence of intervention.

This figure illustrates the significance of immunotherapeutic stimulation. The bifurcation in equilibrium findings indicates that the system is responsive to the parameter S, which governs external stimulation. The phase diagram illustrates how immune modulation alters the configuration of attractors and modifies the trajectories of systems.

This contrast is crucial for understanding the distinction between therapeutic success and failure. The figure illustrates the system's threshold-like behavior by contrasting trajectories with and without intervention. It also demonstrates how little alteration in immune activation can result in very divergent long-term outcomes. By comparing and contrasting these factors, the areas of parameter space that respond best to interventions can be located. This makes it easier to create effective immunotherapeutic plans.

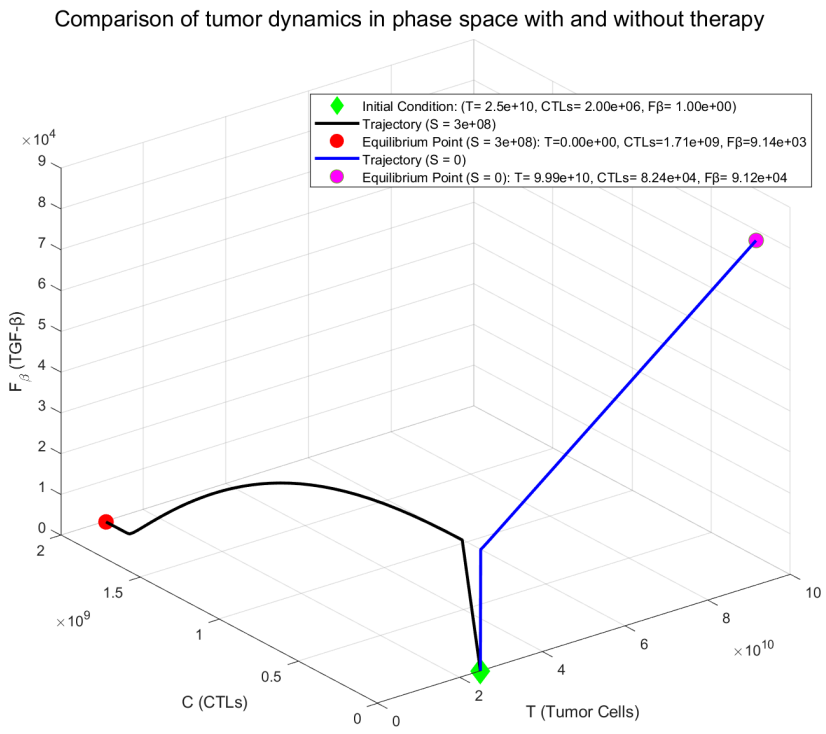

Figure 4.27: Tumor dynamics in phase space with and without treatment. Initial conditions: $T(0) = 2.5 \times 10^{10}$, $C(0) = 2 \times 10^6$, $F_\beta(0) = 1$. Equilibrium points: With therapy ($S = 3 \times 10^8$): $T \approx 0$, $C \approx 1.71 \times 10^9$, $F_\beta \approx 9140$. Without therapy ($S = 0$): $T \approx 9.99 \times 10^{10}$, $C \approx 8.24 \times 10^4$, $F_\beta \approx 91200$.

CHAPTER 5

Conclusions

5.1 Key contributions

This doctoral thesis makes significant contributions to the intersection of artificial intelligence and mathematical modeling for the diagnosis and therapeutic evaluation of gliomas. The principal achievements are as follows:

First, in the domain of deep learning, two classification stages were successfully implemented. In the multiclass classification stage, six state-of-the-art CNNs, InceptionV3, ResNet50, Xception, InceptionResNetV2, EfficientNetB0, and MobileNetV2, were trained and evaluated on MRI images to classify glioma, meningioma, pituitary tumors, and healthy brain tissue. Among these, the InceptionV3 model achieved the highest performance, reaching an accuracy of 97.12%. This demonstrates the feasibility of utilizing deep learning models for accurate, automated brain tumor classification, reducing diagnostic subjectivity and aiding radiological workflows. In the second stage, focused on binary classification between LGG and HGG, six additional architectures, Inception_v4, Xception41, ConvNextV2_Tiny, Swin_Tiny_Patch4_Window7_224, EfficientNetB0, and DeiT3_Base_Patch16_224 were trained on the BRATS 2019 dataset. The best performing models achieved test accuracies above 99%, confirming the robustness of the approach for clinically relevant tumor grading. This two-stage classification pipeline represents a practical contribution to medical imaging analysis, showcasing the utility of deep learning tools for both general tumor detection and precise glioma grading. Moreover, GradCAM interpretability techniques were applied to assess model decision-making, further validating the potential of these models to assist clinicians by highlighting tumor regions automatically.

Second, in the domain of mathematical modeling, a novel six-dimensional system of ordinary differential equations was formulated to simulate the dynamic interaction between tumor cells, CTLs, and immune mediators under immunotherapy. The iterative compact invariant set localization method was employed to rigorously study the global dynamics of the system. This mathematical model not only provides qualitative and quantitative insights into tumor–immune system interactions but also serves as a predictive tool to assess the efficacy of different immunotherapeutic strategies. Thus, it exemplifies the role of "mathematical medicine" in enhancing therapeutic planning, optimizing treatment protocols, and supporting clinical decision-making through simulation-based evidence.

Collectively, this work demonstrates the integration of advanced artificial intelligence techniques and nonlinear dynamic modeling as a promising paradigm for precision neuro-oncology, contributing

both to early diagnosis and to the personalized design of treatment strategies.

5.2 Limitations of the study

Although the training datasets employed are extensive, they may not fully encapsulate the biological and clinical diversity of glioma presentations across global populations, potentially affecting model generalizability. The classification models, despite their high performance, may be susceptible to biases arising from class imbalance or underrepresentation of specific glioma subtypes. In the mathematical modeling component, the adopted assumptions regarding immune–tumor interactions and treatment regimens, while biologically plausible, necessitate further empirical validation against longitudinal clinical datasets. Additionally, the interpretability of the deep learning models, as inferred through Grad-CAM analysis, remains partially constrained, highlighting the need for more transparent AI methodologies to facilitate clinical integration.

5.3 Future work

Future research could enhance glioma classification methods by including other medical imaging modalities, such as functional MRI or positron emission tomography (PET), to improve diagnostic precision. Augmenting the dataset to include a broader array of cases, including uncommon tumor forms and different phases of gliomas, may provide a more resilient model for practical applications. Furthermore, investigating hybrid deep learning architectures that integrate various networks, such as using the advantages of InceptionV4 and DeiT3 for enhanced generalization, may further augment classification outcomes. One potential approach is to investigate the interpretability of the models, enabling clinicians to understand the reasoning behind the classifications, which is crucial for practical implementation. The integration of real-time data augmentation and transfer learning from analogous domains might enhance performance with limited datasets, making these models more versatile and effective in clinical settings. These developments may render AI-driven categorization systems indispensable for the early and precise diagnosis of gliomas, thereby enhancing patient outcomes.

In mathematical modeling may concentrate on enhancing and verifying the glioma model under CTL-based immunotherapy via more intricate simulations and empirical data. A potential study avenue might include incorporating other biological elements, such as the interactions among various immune cell types or the effects of combination therapy, to enhance the understanding of glioma's response to diverse therapeutic strategies. Furthermore, it would be intriguing to investigate other numerical approaches that enhance the precision in localizing invariant compact sets, enabling a more comprehensive examination of nonlinear dynamics. Incorporating changes in glioma features, such as tumor heterogeneity, may provide new insights for customizing immune treatments according to patient-specific traits.

References

[1] Zvia Agur, Karin Halevi-Tobias, Yuri Kogan, and Ofer Shlagman. Employing dynamical computational models for personalizing cancer immunotherapy. *Expert opinion on biological therapy*, 16(11):1373–1385, 2016.

[2] Natalie Kronik, Yuri Kogan, Vladimir Vainstein, and Zvia Agur. Improving alloreactive ctl immunotherapy for malignant gliomas using a simulation model of their interactive dynamics. *Cancer Immunology, Immunotherapy*, 57:425–439, 2008.

[3] Yuri Kogan, Urszula Foryś, Ofir Shukron, Natalie Kronik, and Zvia Agur. Cellular immunotherapy for high grade gliomas: mathematical analysis deriving efficacious infusion rates based on patient requirements. *SIAM Journal on Applied Mathematics*, 70(6):1953–1976, 2010.

[4] Atika Akter, Nazeela Nosheen, Sabbir Ahmed, Mariom Hossain, Mohammad Abu Yousuf, Mohammad Ali Abdullah Almoyad, Khondokar Fida Hasan, and Mohammad Ali Moni. Robust clinical applicable cnn and u-net based algorithm for mri classification and segmentation for brain tumor. *Expert Systems with Applications*, page 122347, 2023.

[5] Pallabi Sharma, Deepak Ranjan Nayak, Bunil Kumar Balabantaray, M Tanveer, and Rajashree Nayak. A survey on cancer detection via convolutional neural networks: Current challenges and future directions. *Neural Networks*, 2023.

[6] Nahid Ferdous Aurna, Mohammad Abu Yousuf, Kazi Abu Taher, AKM Azad, and Mohammad Ali Moni. A classification of mri brain tumor based on two stage feature level ensemble of deep cnn models. *Computers in biology and medicine*, 146:105539, 2022.

[7] B Sarala, G Sumathy, AV Kalpana, and J Jasmine Hephzipah. Glioma brain tumor detection using dual convolutional neural networks and histogram density segmentation algorithm. *Biomedical Signal Processing and Control*, 85:104859, 2023.

[8] MK Balwant. A review on convolutional neural networks for brain tumor segmentation: Methods, datasets, libraries, and future directions. *IRBM*, 43(6):521–537, 2022.

[9] Md Monirul Islam, Prema Barua, Moshiur Rahman, Tanvir Ahammed, Laboni Akter, and Jia Uddin. Transfer learning architectures with fine-tuning for brain tumor classification using magnetic resonance imaging. *Healthcare Analytics*, 4:100270, 2023.

[10] Zahid Rasheed, Yong-Kui Ma, Inam Ullah, Tamara Al Shloul, Ahsan Bin Tufail, Yazeed Yasin Ghadi, Muhammad Zubair Khan, and Heba G Mohamed. Automated classification of brain tumors from magnetic resonance imaging using deep learning. *Brain Sciences*, 13(4):602, 2023.

[11] Arkapravo Chattopadhyay and Mausumi Maitra. Mri-based brain tumour image detection using cnn based deep learning method. *Neuroscience informatics*, 2(4):100060, 2022.

[12] Radhika Malhotra, Barjinder Singh Saini, and Savita Gupta. Survival classification of gliomas through a novel enhancement-based strategy for class overlap of radiomics features. *Expert Systems with Applications*, page 122320, 2023.

[13] Tapas Kumar Dutta, Deepak Ranjan Nayak, and Yu-Dong Zhang. Arm-net: Attention-guided residual multiscale cnn for multiclass brain tumor classification using mr images. *Biomedical Signal Processing and Control*, 87:105421, 2024.

[14] Takowa Rahman and Md Saiful Islam. Mri brain tumor detection and classification using parallel deep convolutional neural networks. *Measurement: Sensors*, 26:100694, 2023.

[15] Monika Sachdeva, Alok Kumar Singh Kushwaha, et al. Irnetv: A deep learning framework for automated brain tumor diagnosis. *Biomedical Signal Processing and Control*, 87:105459, 2024.

[16] Naeem Ullah, Javed Ali Khan, Mohammad Sohail Khan, Wahab Khan, Izaz Hassan, Marwa Obayya, Noha Negm, and Ahmed S Salama. An effective approach to detect and identify brain tumors using transfer learning. *Applied Sciences*, 12(11):5645, 2022.

[17] Zahid Rasheed, Yong-Kui Ma, Inam Ullah, Yazeed Yasin Ghadi, Muhammad Zubair Khan, Muhammad Abbas Khan, Akmalbek Abdusalomov, Fayez Alqahtani, and Ahmed M Shehata. Brain tumor classification from mri using image enhancement and convolutional neural network techniques. *Brain Sciences*, 13(9):1320, 2023.

[18] Paul A Valle, Luis N Coria, and Karla D Carballo. Chemoimmunotherapy for the treatment of prostate cancer: Insights from mathematical modelling. *Applied Mathematical Modelling*, 90:682–702, 2021.

[19] Paul A Valle, Luis N Coria, and Corina Plata. Personalized immunotherapy treatment strategies for a dynamical system of chronic myelogenous leukemia. *Cancers*, 13(9):2030, 2021.

[20] Soroosh Arshadi and Ahmad Reza Pishevar. Magnetic drug delivery effects on tumor growth. *Informatics in Medicine Unlocked*, 27:100789, 2021.

[21] Subhas Khajanchi. The impact of immunotherapy on a glioma immune interaction model. *Chaos, Solitons & Fractals*, 152:111346, 2021.

[22] Irene Golán, Laura Rodriguez de la Fuente, and Jose A Costoya. Nk cell-based glioblastoma immunotherapy. *Cancers*, 10(12):522, 2018.

[23] Masoumeh Najafi, Amin Jahanbakhshi, Sebastiano Finocchi Ghersi, Lucia Giaccherini, Andrea Botti, Francesco Cavallieri, Jessica Rossi, Federico Iori, Cinzia Iotti, Patrizia Ciammella, et al. Clinical effects of immuno-oncology therapy on glioblastoma patients: A systematic review. *Brain Sciences*, 13(2):159, 2023.

[24] Jorge L López-Agredo, Diego A Rueda-Gómez, and Élder J Villamizar-Roa. Numerical analysis of a mathematical model describing the evolution of hypoxic glioma cells. *Computers & Mathematics with Applications*, 131:138–157, 2023.

[25] Konstantin E Starkov and Diana Gamboa. Localization of compact invariant sets and global stability in analysis of one tumor growth model. *Mathematical Methods in the Applied Sciences*, 37(18):2854–2863, 2014.

[26] Konstantin E Starkov. On dynamic tumor eradication conditions under combined chemical/anti-angiogenic therapies. *Physics Letters A*, 382(6):387–393, 2018.

[27] Alexander P Krishchenko and Konstantin E Starkov. 5d model of pancreatic cancer: Key features of ultimate dynamics. *Communications in Nonlinear Science and Numerical Simulation*, 103:105997, 2021.

[28] Konstantin E Starkov and Anatoly N Kanatnikov. Cancer cell eradication in a 6d metastatic tumor model with time delay. *Communications in Nonlinear Science and Numerical Simulation*, 120:107164, 2023.

[29] A Priya and V Vasudevan. Brain tumor classification and detection via hybrid alexnet-gru based on deep learning. *Biomedical Signal Processing and Control*, 89:105716, 2024.

[30] Wanyi Sun, Cheng Song, Chao Tang, Chenghao Pan, Peng Xue, Jinhu Fan, and Youlin Qiao. Performance of deep learning algorithms to distinguish high-grade glioma from low-grade glioma: A systematic review and meta-analysis. *Iscience*, 2023.

[31] Evgin Goceri. Vision transformer based classification of gliomas from histopathological images. *Expert Systems with Applications*, 241:122672, 2024.

[32] Szidónia Lefkovits, László Lefkovits, and László Szilágyi. Hgg and lgg brain tumor segmentation in multi-modal mri using pretrained convolutional neural networks of amazon sagemaker. *Applied Sciences*, 12(7):3620, 2022.

[33] Shingo Kihira, Xueyan Mei, Keon Mahmoudi, Zelong Liu, Siddhant Dogra, Puneet Belani, Nadejda Tsankova, Adilia Hormigo, Zahi A Fayad, Amish Doshi, et al. U-net based segmentation and characterization of gliomas. *Cancers*, 14(18):4457, 2022.

[34] Ghazanfar Latif, Ghassen Ben Brahim, DNF Awang Iskandar, Abul Bashar, and Jaafar Alghazo. Glioma tumors' classification using deep-neural-network-based features with svm classifier. *Diagnostics*, 12(4):1018, 2022.

[35] Kaitlyn Alleman, Erik Knecht, Jonathan Huang, Lu Zhang, Sandi Lam, and Michael DeCuypere. Multimodal deep learning-based prognostication in glioma patients: A systematic review. *Cancers*, 15(2):545, 2023.

[36] Said Seif Salim, Eunice Mureithi, Nyimvua Shaban, and Joseph Malinzi. Mathematical modelling of the dynamics of prostate cancer with a curative vaccine. *Scientific African*, 11:e00715, 2021.

[37] Md Atiqur Rahman, Mustavi Ibne Masum, Khan Md Hasib, MF Mridha, Sultan Alfarhood, Mejdl Safran, and Dunren Che. Gliomacnn: An effective lightweight cnn model in assessment of classifying brain tumor from magnetic resonance images using explainable ai. *CMES-Computer Modeling in Engineering & Sciences*, 140(3), 2024.

[38] Prince Priya Malla, Sudhakar Sahu, and Ahmed I Alutaibi. Classification of tumor in brain mr images using deep convolutional neural network and global average pooling. *Processes*, 11(3):679, 2023.

[39] Vladimir Despotovic, Sang-Yoon Kim, Ann-Christin Hau, Aliaksandra Kakoichankava, Gilbert Georg Klamminger, Felix Bruno Kleine Borgmann, Katrin BM Frauenknecht, Michel Mittelbronn, and Petr V Nazarov. Glioma subtype classification from histopathological images using in-domain and out-of-domain transfer learning: An experimental study. *Heliyon*, 10(5), 2024.

[40] Maad M Mijwil. Smart architectures: computerized classification of brain tumors from mri images utilizing deep learning approaches. *Multimedia Tools and Applications*, pages 1–32, 2024.

[41] Lingling Fang and Yumeng Jiang. Dual-path parallel hierarchical diagnostic model of glioma based on pathomorphological feature. *Biomedical Signal Processing and Control*, 87:105559, 2024.

[42] PS Tejashwini, J Thriveni, and KR Venugopal. Ebt deep net: Ensemble brain tumor deep net for multi-classification of brain tumor in mr images. *Biomedical Signal Processing and Control*, 95:106312, 2024.

[43] Daniel Reyes and Javier Sánchez. Performance of convolutional neural networks for the classification of brain tumors using magnetic resonance imaging. *Heliyon*, 10(3), 2024.

[44] Pallavi Priyadarshini, Priyadarshi Kanungo, and Tejaswini Kar. Multigrade brain tumor classification in mri images using fine tuned efficientnet. *e-Prime-Advances in Electrical Engineering, Electronics and Energy*, 8:100498, 2024.

[45] Deependra Rastogi, Prashant Johri, Varun Tiwari, and Ahmed A Elngar. Multi-class classification of brain tumour magnetic resonance images using multi-branch network with inception block and five-fold cross validation deep learning framework. *Biomedical Signal Processing and Control*, 88:105602, 2024.

[46] Ercan Gürsoy and Yasin Kaya. Brain-gcn-net: Graph-convolutional neural network for brain tumor identification. *Computers in Biology and Medicine*, 180:108971, 2024.

[47] P Sreedevi, Ajmeera Kiran, T Santhi Sri, E Poornima, Sanjeeva Polepaka, and Y Supriya Reddy. Da-resbigru-brain tumor classification using dual attention residual bi directional gated recurrent unit using mri images. *Biomedical Signal Processing and Control*, 88:105596, 2024.

[48] Gayathri Devi Krishnamoorthy and Kishore Balasubramanian. Multivariate technique for the prediction and classification of brain tumor using deep shallow network. *Applied Soft Computing*, 164:111962, 2024.

[49] A Priya and V Vasudevan. Brain tumor classification and detection via hybrid alexnet-gru based on deep learning. *Biomedical Signal Processing and Control*, 89:105716, 2024.

[50] Muhammed Celik and Ozkan Inik. Development of hybrid models based on deep learning and optimized machine learning algorithms for brain tumor multi-classification. *Expert Systems with Applications*, 238:122159, 2024.

[51] K Nishanth Rao, Osamah Ibrahim Khalaf, V Krishnasree, Aruru Sai Kumar, Deema Mohammed Alsekait, S Siva Priyanka, Ahmed Saleh Alattas, and Diaa Salama AbdElminaam. An efficient brain tumor detection and classification using pre-trained convolutional neural network models. *Heliyon*, 10(17), 2024.

[52] Ernesto Urenda-Cázares, Armando Gallegos, and Jorge Eduardo Macías-Díaz. A mathematical model that combines chemotherapy and oncolytic virotherapy as an alternative treatment against a glioma. *Journal of Mathematical Chemistry*, 58:544–554, 2020.

[53] Tedi Ramaj and Xingfu Zou. On the treatment of melanoma: A mathematical model of oncolytic virotherapy. *Mathematical Biosciences*, 365:109073, 2023.

[54] Léo Adenis, Stéphane Plaszczynski, Basile Grammaticos, Johan Pallud, and Mathilde Badoual. The effect of radiotherapy on diffuse low-grade gliomas evolution: confronting theory with clinical data. *Journal of Personalized Medicine*, 11(8):818, 2021.

[55] Rebecca Anne Bekker, Sungjune Kim, Shari Pilon-Thomas, and Heiko Enderling. Mathematical modeling of radiotherapy and its impact on tumor interactions with the immune system. *Neoplasia*, 28:100796, 2022.

[56] Luis E Ayala-Hernández, Armando Gallegos, Philippe Schucht, Michael Murek, Luis Pérez-Romasanta, Juan Belmonte-Beitia, and Víctor M Pérez-García. Optimal combinations of chemotherapy and radiotherapy in low-grade gliomas: a mathematical approach. *Journal of personalized medicine*, 11(10):1036, 2021.

[57] Kang-Ling Liao, Adam J Wieler, and Pedro M Lopez Gascon. Mathematical modeling and analysis of cancer treatment with radiation and anti-pd-l1. *Mathematical Biosciences*, page 109218, 2024.

[58] Hsiu-Chuan Wei. Mathematical modeling of tumor growth and treatment: Triple negative breast cancer. *Mathematics and Computers in Simulation*, 204:645–659, 2023.

[59] Runpeng Li, Prativa Sahoo, Dongrui Wang, Qixuan Wang, Christine E Brown, Russell C Rockne, and Heyrim Cho. Modeling interaction of glioma cells and car t-cells considering multiple car t-cells bindings. *ImmunoInformatics*, 9:100022, 2023.

[60] Daniela Silva Santurio, Emanuelle A Paixão, Luciana RC Barros, Regina C Almeida, and Artur C Fassoni. Mechanisms of resistance to car-t cell immunotherapy: Insights from a mathematical model. *Applied Mathematical Modelling*, 125:1–15, 2024.

[61] Pariya Khalili and Ramin Vatankhah. Studying the importance of regulatory t cells in chemoimmunotherapy mathematical modeling and proposing new approaches for developing a mathematical dynamic of cancer. *Journal of Theoretical Biology*, 563:111437, 2023.

[62] Ophir Nave. A mathematical model for treatment using chemo-immunotherapy. *Heliyon*, 8(4), 2022.

[63] Kangbo Bao, Guizhen Liang, Tianhai Tian, and Xinan Zhang. Mathematical modeling of combined therapies for treating tumor drug resistance. *Mathematical Biosciences*, 371:109170, 2024.

[64] Megan Dixon, Tuan Anh Phan, JC Dallon, and Jianjun Paul Tian. Mathematical model for il-2-based cancer immunotherapy. *Mathematical Biosciences*, 372:109187, 2024.

[65] Mrinmoy Sardar, Subhas Khajanchi, Santosh Biswas, and Sumana Ghosh. A mathematical model for tumor-immune competitive system with multiple time delays. *Chaos, Solitons & Fractals*, 179:114397, 2024.

[66] Kaushik Dehingia, Yamen Alharbi, and Vikas Pandey. A mathematical tumor growth model for exploring saturated response of m2 macrophages. *Healthcare Analytics*, 5:100306, 2024.

[67] Alexander P Krishchenko and Konstantin E Starkov. Localization analysis of compact invariant sets of multi-dimensional nonlinear systems and symmetrical prolongations. *Communications in Nonlinear Science and Numerical Simulation*, 15(5):1159–1165, 2010.

[68] Konstantin E Starkov and Laura Jimenez Beristain. Dynamic analysis of the melanoma model: from cancer persistence to its eradication. *International Journal of Bifurcation and Chaos*, 27(10):1750151, 2017.

[69] Marco Antonio Gómez-Guzmán, Laura Jiménez-Beristaín, Enrique Efren García-Guerrero, Oscar Roberto López-Bonilla, Ulises Jesús Tamayo-Perez, José Jaime Esqueda-Elizondo, Kenia Palomino-Vizcaino, and Everardo Inzunza-González. Classifying brain tumors on magnetic resonance imaging by using convolutional neural networks. *Electronics*, 12(4):955, 2023.

[70] Msoud Nickparvar. Brain tumor mri dataset, 2021. (accessed on 10 December 2024) https://www.kaggle.com/dsv/2645886.

[71] Karen Simonyan and Andrew Zisserman. Very deep convolutional networks for large-scale image recognition. *arXiv preprint arXiv:1409.1556*, 2014.

[72] Kashif Shaheed, Aihua Mao, Imran Qureshi, Munish Kumar, Sumaira Hussain, Inam Ullah, and Xingming Zhang. Ds-cnn: A pre-trained xception model based on depth-wise separable convolutional neural network for finger vein recognition. *Expert Systems with Applications*, 191:116288, 2022.

[73] François Chollet. Xception: Deep learning with depthwise separable convolutions. In *Proceedings of the IEEE conference on computer vision and pattern recognition*, pages 1251–1258, 2017.

[74] Xiaoling Xia, Cui Xu, and Bing Nan. Inception-v3 for flower classification. In *2017 2nd international conference on image, vision and computing (ICIVC)*, pages 783–787. IEEE, 2017.

[75] Mingxing Tan and Quoc Le. Efficientnet: Rethinking model scaling for convolutional neural networks. In *International conference on machine learning*, pages 6105–6114. PMLR, 2019.

[76] Mark Sandler, Andrew Howard, Menglong Zhu, Andrey Zhmoginov, and Liang-Chieh Chen. Mobilenetv2: Inverted residuals and linear bottlenecks. In *Proceedings of the IEEE conference on computer vision and pattern recognition*, pages 4510–4520, 2018.

[77] Jun Cheng. Brain tumor dataset, 2017. (accessed on 28 March 2025) https://figshare.com/articles/dataset/brain_tumor_dataset/1512427.

[78] Sartaj Bhuvaji, Ankita Kadam, Prajakta Bhumkar, Sameer Dedge, and Swati Kanchan. Brain tumor classification (mri), 2020. (accessed on 28 March 2025) https://www.kaggle.com/dsv/1183165.

[79] Ahmed Hamada. Br35h: Brain tumor detection 2020, 2020. (accessed on 28 March 2025) https://www.kaggle.com/datasets/ahmedhamada0/brain-tumor-detection?select=no.

[80] Edgar Rene Ramos-Acosta, Enrique Efrén García-Guerrero, Oscar Roberto López-Bonilla, Ulises Jesús Tamayo-Pérez, Oscar Adrián Aguirre-Castro, Lidia Yolanda Ramírez-Rios, and Everardo Inzunza-Gonzalez. A novel system for the classification of zinc-plated components by benchmarking deep neural networks. *Expert Systems with Applications*, 255:124866, 2024.

[81] Christian Szegedy, Sergey Ioffe, Vincent Vanhoucke, and Alexander Alemi. Inception-v4, inception-resnet and the impact of residual connections on learning. In *Proceedings of the AAAI conference on artificial intelligence*, 2017.

[82] Hugo Touvron, Matthieu Cord, Matthijs Douze, Francisco Massa, Alexandre Sablayrolles, and Hervé Jégou. Training data-efficient image transformers & distillation through attention. In *International conference on machine learning*, pages 10347–10357. PMLR, 2021.

[83] Ze Liu, Yutong Lin, Yue Cao, Han Hu, Yixuan Wei, Zheng Zhang, Stephen Lin, and Baining Guo. Swin transformer: Hierarchical vision transformer using shifted windows. In *Proceedings of the IEEE/CVF international conference on computer vision*, pages 10012–10022, 2021.

[84] Sanghyun Woo, Shoubhik Debnath, Ronghang Hu, Xinlei Chen, Zhuang Liu, In So Kweon, and Saining Xie. Convnext v2: Co-designing and scaling convnets with masked autoencoders. In *Proceedings of the IEEE/CVF Conference on Computer Vision and Pattern Recognition*, pages 16133–16142, 2023.

[85] Spyridon (Spyros) Bakas. Brats miccai brain tumor dataset, 2020, https://dx.doi.org/10.21227/hdtd-5j88.

[86] Davide Chicco and Giuseppe Jurman. The advantages of the matthews correlation coefficient (mcc) over f1 score and accuracy in binary classification evaluation. *BMC genomics*, 21:1–13, 2020.

[87] Alexander P Krishchenko and Konstantin E Starkov. 5d model of pancreatic cancer: Key features of ultimate dynamics. *Communications in Nonlinear Science and Numerical Simulation*, 103:105997, 2021.

[88] L Biewald. Software for experiment tracking with weights and biases. *Weights & Biases*, 2020.

[89] Andreas Theissler, Simon Vollert, Patrick Benz, Laurentius A Meerhoff, and Marc Fernandes. Ml-modelexplorer: An explorative model-agnostic approach to evaluate and compare multiclass classifiers. In *Machine Learning and Knowledge Extraction: 4th IFIP TC 5, TC 12, WG 8.4, WG 8.9, WG 12.9 International Cross-Domain Conference, CD-MAKE 2020, Dublin, Ireland, August 25–28, 2020, Proceedings 4*, pages 281–300. Springer, 2020.

APPENDIX A

Scientific production, dissemination, and outreach

A.1 Products derived from the thesis work

Journal Publications (JCR)

1. Marco Antonio Gómez-Guzmán, Laura Jiménez-Beristáin, Enrique Efren García-Guerrero, Oscar Roberto López-Bonilla, Ulises Jesús Tamayo-Perez, José Jaime Esqueda-Elizondo, Kenia Palomino-Vizcaino, Everardo Inzunza-González. (2023). Classifying brain tumors on magnetic resonance imaging by using convolutional neural networks. Electronics, 12(4), 955.

   DOI: https://doi.org/10.3390/electronics12040955

2. Marco Antonio Gómez-Guzmán, Everardo Inzunza-González, Kenia Palomino-Vizcaino, José Jaime Esqueda-Elizondo, Enrique Efren García-Guerrero, Oscar Roberto López-Bonilla, Ulises Jesús Tamayo-Perez, Laura Jiménez-Beristáin. (2024). Analysis of immunotherapeutic control of the TH1/TH2 imbalance in a 4D melanoma model applying the invariant compact set localization method. Alexandria Engineering Journal, 107, 838-850.

   DOI: https://doi.org/10.1016/j.aej.2024.09.023

3. Marco Antonio Gómez-Guzmán, Laura Jiménez-Beristáin, Enrique Efren García-Guerrero, Oscar Adrian Aguirre-Castro, Edgar René Ramos-Acosta, José Jaime Esqueda-Elizondo, Gilberto Manuel Galindo-Aldana, Cynthia Torres-Gonzalez, Everardo Inzunza-Gonzalez. (2025). A novel system for Glioma classification in magnetic resonance imaging by benchmarking deep learning architectures. Expert systems with applications. Status: Submitted.

4. Marco Antonio Gómez-Guzmán, Laura Jiménez-Beristáin, Enrique Efren García-Guerrero, Oscar Adrian Aguirre-Castro, José Jaime Esqueda-Elizondo, Edgar René Ramos-Acosta, Gilberto Manuel Galindo-Aldana, Cynthia Torres-Gonzalez, Everardo Inzunza-Gonzalez. (2025). Enhanced Multi-Class Brain Tumor Classification in MRI Using Pre-trained CNNs and Transformer Architectures. Technologies. Status: Submitted.

5. Marco Antonio Gómez-Guzmán, Everardo Inzunza-Gonzalez, Enrique Efren García-Guerrero, José Jaime Esqueda-Elizondo, Laura Jiménez-Beristain. (2025). Dynamic analysis of glioma model with immunotherapy using invariant compact set localization method. Status: Submitted.

Universal access to knowledge

1. Marco Antonio Gómez-Guzmán, Laura Jiménez-Beristáin, Enrique Efren García-Guerrero, Oscar Roberto López-Bonilla, Ulises Jesús Tamayo-Perez, José Jaime Esqueda-Elizondo, Kenia Palomino-Vizcaino, Everardo Inzunza-González. (2021). Evaluación de la dinámica global en modelo de cáncer cerebral usando técnicas de aprendizaje automático y método iterativo de Localización. 8vo Simposio de Investigación FIAD 2021. Ensenada, Baja California.

2. Marco Antonio Gómez-Guzmán, Everardo Inzunza-González. (2022). Clasificación de tumores cerebrales en imágenes de resonancia magnética usando redes neuronales convolucionales. 7mo Foro Nacional de Bioingeniería. FCITEC Tijuana, Baja California.

3. Marco Antonio Gómez-Guzmán, Everardo Inzunza-González. (2022). A complex System for Brain Tumor Classification Using Convolutional Neural Networks on MRI Images. 3rd Meeting for the Dissemination and Research in the Study of Complex Systems and their Applications (EDIESCA 2022). Ensenada, Baja California, México.

4. Marco Antonio Gómez-Guzmán, Laura Jiménez-Beristáin, Enrique Efren García-Guerrero, Oscar Roberto López-Bonilla, Ulises Jesús Tamayo-Perez, José Jaime Esqueda-Elizondo, Kenia Palomino-Vizcaino, Everardo Inzunza-González. (2023). Brain Tumor Classification Using Convulutional Neural Networks on MRI Images. 3rd International Virtual Conference on Neuroscience, Brain Disorders and Therapeutics. London, England.

5. Marco Antonio Gómez-Guzmán, Laura Jiménez-Beristáin, José Jaime Esqueda-Elizondo. (2024). Medicina Matemática. 3er. Seminario de Economía Social Solidaria. TECNM Ciudad Madero, Tamaulipas.

6. Marco Antonio Gómez-Guzmán, Everardo Inzunza-González, Laura Jiménez-Beristáin. (2024). Aplicaciones de la inteligencia artificial en la clasificación de tumores cerebrales (Taller). Congreso Multidisciplinario Internacional 2024, Inteligencia Artificial "Retos y Expectativas". TECNM Campus Pánuco, Veracruz.

7. Marco Antonio Gómez-Guzmán, Everardo Inzunza-González, Laura Jiménez-Beristáin. (2024). Aplicaciones de la inteligencia artificial en la clasificación de tumores cerebrales (Conferencia). Congreso Multidisciplinario Internacional 2024, Inteligencia Artificial "Retos y Expectativas". TECNM Campus Pánuco, Veracruz.

8. Marco Antonio Gómez-Guzmán, Everardo Inzunza-González, Laura Jiménez-Beristáin. (2024). Inteligencia Artificial como metodología de prevención de tumores en trabajadores mexicanos. Conferencia Procesos de Trabajo de la Licenciatura en Psicología del Trabajo. Facultad de Psicología UAQ, Santiago de Querétaro, Querétaro.

9. Marco Antonio Gómez-Guzmán, Everardo Inzunza-González, Laura Jiménez-Beristáin. (2024). Inteligencia Artificial, internet de las cosas, robótica y su impacto en las transformaciones de los Procesos de Trabajo en México. Conferencia Procesos de Trabajo de la Licenciatura en Psicología del Trabajo. Facultad de Psicología UAQ, Santiago de Querétaro, Querétaro.